

Final Report - 2nd Phase

DFG Research Group FOR575

**High Frequency Parasitic Effects in
Inverter-fed Electric Drives**

*Höherfrequente Parasitäreffekte in
umrichtergespeisten elektrischen Antrieben*

Prof. Dr.-Ing. habil. Dr. h.c. Andreas Binder (Sprecher)
PD Dr. rer.nat. Erion Gjonaj
Prof. Dr.-Ing. Volker Hinrichsen
Prof. Dr.-Ing. Peter Mutschler
Prof. Dr.-Ing. Thomas Weiland

Darmstadt, July 2012

Responsible for the report:

Prof. Dr.-Ing. habil. Dr.h.c. Andreas Binder, geb. 16.7.1957
Technische Universität Darmstadt
Institut für Elektrische Energiewandlung
Fachbereich 18 - Elektrotechnik und Informationstechnik
Landgraf-Georg-Straße 4, D-64283 Darmstadt
Telefon: 06151/16-2167, Fax: 06151/16-6033
E-Mail: abinder@ew.tu-darmstadt.de

1. Summary

This report summarizes the results of the research work in the second phase of the DFG Forschergruppe FOR575.

2. Introduction

The DFG FOR575 second-phase project continued the first-phase of the project with 5 new subprojects (Table 2.1). During the second phase of the project, the group members presented their results in 24 internal meetings. The power point presentations, the meeting protocols and all DFG reports are available at the dedicated DFG FOR575 homepage:

http://www.ew.tu-darmstadt.de/forschung_3/projekt573/projekt573_1.de.jsp

The results of the research are presented in two PhD Thesis (Mr. Purcarea and Ms. Kedarisetti) and 18 scientific papers (Section 4). The scientific results have been recognized with 3 international IEEE awards (Section 5).

TP1-Binder	<p><i>Bearing impedance and bearing damage due to bearing currents in inverter-fed electrical machines</i> Dipl.-Ing. Oliver Magdun Dipl.-Ing. Yves Gemeinder, starting: 1st December 2009 Tutor: Prof. A. Binder</p> <p><i>Start date:</i> 7th April 2009 <i>End date:</i> 6th April 2012</p>
TP2-Gjonaj	<p><i>Extended transmission line models for inverter-fed electrical drives using multi-rate time integration</i> Dipl.-Ing. Hai Van Jorks Tutor: PD Dr.rer.nat. E.Gjonaj</p> <p><i>Start date:</i> 1st November 2009 <i>End date:</i> 30st October 2012</p>
TP3-Hinrichsen	<p><i>Microvaristors in the insulation of inverter-fed drives</i> Dipl.-Ing. Sébastien Blatt Tutor: Prof. V. Hinrichsen</p> <p><i>Start date:</i> 1st March 2009 <i>End date:</i> 28th February 2012</p>
TP4-Mutschler	<p><i>Motor-friendly and high efficient inverter for electrical drives</i> Dipl.-Ing. Calin Purcarea M-Tech. Jayalakshmi Kedarisetti, starting: 1st November 2009 Tutor: Prof. Mutschler</p> <p><i>Start date:</i> 1st January 2009 <i>End date:</i> 31th October 2011</p>
TP5-Weiland	<p><i>Multi-scale modeling for windings with heterogeneous material distribution considering capacitive effects</i> M.Sc. Zarife Cay, Dipl.-Ing. Frank Denz , started: 1st July 2010 Tutor: Prof. Weiland</p> <p><i>Start date:</i> 1st January 2009 <i>End date:</i> 31th December 2011</p>

Table 2.1 The 5th projects of the 2nd phase of the DFG Research Group FOR575

3. Overview on the research topics

In the 1st subproject **TP1**, systematic experimental investigations were performed to give more insight into the development of bearing damages caused by EDM currents and rotor-to-ground currents. The influence of different operating parameters: bearing load, bearing temperature and speed on the magnitude of EDM currents and rotor-to-ground currents is analysed. In parallel with the practical work, the project dealt with the calculation of the main indicators of the bearing life prediction, the apparent bearing current density and the discharge energy. They were compared with the bearing race degradation degree and the best operating bearing conditions have been established. The bearing impedance has been calculated and measured for several lubricants, at frequencies between 1 kHz ... 30 MHz.

In the 2nd subproject **TP2** the high frequency eddy currents induced in the stator and rotor blocks due to fast inverter switching are investigated. This is performed by first extracting a transmission line model of the machine and then incorporating this model into transient network simulations including the switching network. The transmission line model parameters are extracted from either 2D or 3D eddy current simulations. In particular, the 2D FE analysis is an efficient tool which is commonly employed in machine simulations. However, eddy currents induced in laminations cannot be accounted for in 2D geometry. They are usually modeled by means of homogenized, equivalent material models for the iron core. The investigation of the validity of these models in the interesting high frequency range is an important goal of the subproject. In order to fully include eddy current effects in the laminations, we have developed a specialized 3D simulation tool. Furthermore, a numerical procedure for extracting transmission line parameters from large FE discretization matrices is implemented. Full 3D eddy current simulations are performed for a number of test cases as well as for the entire cross-section of an existing 240 kW motor.

The 3rd subproject **TP3** deals with the application of microvaristors in inverter fed drives. Previous investigations (DFG FOR 575, 1st phase, Final Project 2009) have shown that the microvaristors reduce the overvoltages produced by the traveling wave effects of the cable between inverter and motor. Before performing investigations with microvaristors in the insulation of the inverter fed drive a model of a machine (without microvaristors in the insulation) consisting passive elements was created. After optimization of the model the simulated voltage distribution are nearly the same as the measured voltage distribution. Then, the simulation model was extended with nonlinear elements to consider the nonlinear effects of the microvaristors. The measured E–J characteristic of a microvaristor filled varnish was used to simulate the effects of microvaristors in the motor insulation. Simulations with different switching points were performed by shifting the measured E–J characteristics. These simulations showed decreasing of the overvoltages due to traveling wave effects, but increasing of the dielectric losses.

Two quasi-resonant DC-link (QRDCL) inverter topologies are analyzed, in the 4th subproject **TP4**, for a motor-friendly application. For the control of an inverter, a modified space vector pulse width modulation is implemented, which requires only two resonant cycles per switching period

and helps in better utilization of DC-link voltage. The first topology is tested experimentally with a 34 m long cable connected between inverter and induction machine for reduced voltage overshoot at motor side cable end and common mode (CM) voltage. This QRDCL inverter is then compared with the conventional hard switched voltage source inverter together with filter under identical load conditions. Even though results are satisfying, a freewheeling interval of this topology produces high losses. So a new motor friendly QRDCL inverter with lossless variable zero voltage duration is proposed. In this topology, during a zero voltage interval, energy is stored in a capacitor rather than an inductor. No current is freewheeling through inverter switches, and it clearly helps in reducing the losses under a low modulation index region. Simulation results are presented to verify the validity of the proposed inverter and its motor friendly characteristics.

The 5th subproject **TP5** deals with the characterization of the nonlinear machine components as well as with the transition from field simulations to equivalent network models. The nonlinearity of microvaristor filled insulator shieldings is analyzed in terms of their field depended permittivity and electrical conductivity. Emphasis is given to the development of an appropriate model for the ferroelectric-like behavior of these materials. Another goal of the project is the derivation of nonlinear capacitances and conductances from numerical field simulations. The widely used approach used for this purpose is based on the linear superposition principle. This, however, does not apply in the highly nonlinear case of microvaristor insulation. We develop a method for extracting nonlinear equivalent network models from transient electro-quasistatics simulations. These models are, then, integrated in the full transient simulation of electric drives in order to quantify the propagation of higher frequency parasitic currents in inverter-fed induction machines.

4. List of publications

1. O. Magdun, Y. Gemeinder, A. Binder, "Investigation of Influence of Bearing Load and Bearing Temperature on EDM Bearing Currents", Proceedings of ECCE'10, pp. 2733-2738, Atlanta, USA, 12-16 September, 2010.
2. O. Magdun, Y. Gemeinder, A. Binder, "Prevention of Harmful EDM Currents in Inverter-Fed AC Machines by Use of Electrostatic Shields in the Stator Winding Overhang", Proceedings of IECON'10, pp.956-961, Glendale, USA, 6-10 November, 2010.
3. O. Magdun, Y. Gemeinder, A. Binder, "Representation of iron core and dielectric losses for calculation of common mode stator ground currents in inverter-fed AC machines", Proceedings of OPTIM'10, pp. 371-376, Brasov, Romania, 20-22 May, 2010.
4. O. Magdun, Y. Gemeinder, A. Binder, K. Reis, „Calculation of bearing and common-mode voltages for the prediction of bearing failures caused by EDM currents“, Proceedings of SDEMPED'11, pp. 462-467, Bologna, Italy, 5-8 September, 2011.
5. O. Magdun, A. Binder, "An iron core impedance model for calculating high frequency common mode currents and induced shaft voltages in inverter-fed AC machines", Proceedings of SPEEDAM'12, pp. 135-140, Sorrento, Italy, 20-22 June, 2012.
6. O. Magdun, A. Binder, "The High-Frequency Induction Machine Parameters and Their Influence on the Common Mode Stator Ground Current", (accepted at ICEM'12, Marseille, France, 2012).

7. J. Kedarisetti, C. Purcarea and P. Mutschler, “Design of a Quasi resonant DC-link soft switching inverter,” in Proc. International Symposium on Power Electronics Electrical Drives Automation and Motion (SPEEDAM), 2010, pp. 454-459.
8. J. Kedarisetti and P. Mutschler, “A motor friendly quasi-resonant DC-link inverter with lossless variable zero voltage duration,” IEEE Trans. Power Electron., accepted for publication.
9. J. Kedarisetti and P. Mutschler, “Efficiency comparison between motor friendly hard and soft switching inverters,” in Proc. 14th European Conference on Power Electronics and Applications (EPE), 2011, pp. 1-10.
10. J. Kedarisetti and P. Mutschler, “Control of a quasi-resonant DC-link soft switching inverter,” in Proc. IEEE International Symposium on Industrial Electronics ISIE, 2011, pp.171-176.
11. J. Kedarisetti and P. Mutschler, “FPGA based control of quasi-resonant DC-link inverter and induction motor drive,” in Proc. IEEE International Symposium on Industrial Electronics ISIE, 2011, pp.171-176.
12. H. Jorks, E. Gjonaj, T. Weiland, “Simulation of an induction motor including eddy-current effects in core laminations”, IET 8th International Conference on Computation in Electromagnetics (CEM 2011), Wroclaw, Poland, 11-14 April 2011, pp. 54-55
13. H. Jorks, E. Gjonaj, T. Weiland, "Three-dimensional simulations of an induction motor including eddy current effects in core laminations," accepted for publication in IET Science, Measurement & Technology, May 2012
14. H. Jorks, E. Gjonaj, T. Weiland, "Eddy current analysis in core laminations of PWM controlled induction machine," submitted to Scientific Computing in Electrical Engineering (SCEE 2012), September 11-14, 2012, Zürich, Switzerland
15. H. Jorks, E. Gjonaj, T. Weiland, "Eddy current analysis of a PWM controlled induction machine," submitted to IGTE Symposium, November 6 -19, 2012, Graz, Austria
16. A. Blatt, V. Hinrichsen, “Effects of Microvaristors in the Insulation of Inverter Fed Drives”, ISH 2011, 17th International Symposium on High Voltage Engineering August 22nd – 26th 2011, Hannover, Germany
17. F. Denz, E. Gjonaj and T. Weiland, Nonlinear Characterization and Simulation of Zinc-Oxide Surge Arresters, Bastiaan Michielsen and Jean-René Poirier (Eds.), Scientific Computing in Electrical Engineering (SCEE 2010), The European Consortium for Mathematics in Industry, Vol. 16, Springer-Verlag, Berlin/Heidelberg, 2012, ISBN: 978-3-642-22452-2, pp 213-221
18. F. Denz, E. Gjonaj, T. Weiland, M. Tuczec, V. Hinrichsen, Electric and Thermal Reaction of Zinc Oxide to Current Impulses, 30th International Conference on Lightning Protection (ICLP 2010), Cagliari, Italy, September 2010, paper 6B-1331, pp. 1-5

5. IEEE Paper Awards

5.1. The paper “Investigation of EMI Reduction Techniques Using Time Domain Simulation of Drives”, written by C. Purcarea and P. Mutschler, and presented at the 35th Annual Conference of the IEEE Industrial Electronics Society, IECON’09, 3-5 November 2009, has received the “Committee Prize Paper Award” from the Electrical Machines Technical Committee of the IEEE Industrial Electronics Society. The award was presented at the 36th Annual Conference of the IEEE Industrial Electronics Society, IECON’10, 6-10 November 2010.



Committee Prize Paper Award

The Electrical Machines Technical Committee of the
IEEE Industrial Electronics Society
recognizes

Calin Purcarea, Peter Mutschler

with this Paper Award, First Prize, for the technical competence displayed in
the paper entitled:

**Investigation of EMI reduction techniques using time domain
simulation of drives**

presented at the 35th IECON, 3-5 November 2009, Porto, Portugal

EM Tech. Committee Chair Aldo Boglietti:

IES President Leopoldo Garcia Franquelo:

5.2. The paper “Calculation of bearing and common-mode voltages for the prediction of bearing failures caused by EDM currents” written by O. Magdun, Y. Gemeinder, A. Binder and K. Reis, and presented at the 8th IEEE Symposium on Diagnostics/Prognostics of the IEEE Power Electronics Society, SDEMPED’11, 5-8 September 2011, has received the “SDEMPED Paper Award” from the Technical Thrust on Diagnostics/Prognostics of the IEEE Power Electronics Society.



SDEMPED Paper Award



The Technical Thrust on Diagnostics/Prognostics
of the IEEE Power Electronics Society recognizes

Oliver Magdun, Yves Gemeinder, Andreas Binder, and Kersten Reis

with the Prize Paper Award for
the outstanding technical competence displayed in their paper entitled:

**Calculation of Bearing and Common-Mode Voltages
for the Prediction of Bearing Failures
Caused by EDM Currents,**

presented at the 8th IEEE Symposium on Diagnostics for Electrical Machines,
Power Electronics & Drives

September 5-8, 2011, Bologna - ITALY

Alberto Bellini:

Alberto Bellini, Award Chair

Carla Tassoni:

Carla Tassoni, Award Chair

Gérard André Capolino, Committee Chairman

5.3. The paper “Prevention of Harmful EDM Currents in Inverter-Fed AC Machines by Use of Electrostatic Shields in the Stator Winding Overhang”, written by O. Magdun, Y. Gemeinder, and A. Binder, and presented at the 36th Annual Conference of the IEEE Industrial Electronics Society, IECON’10, 6-10 November 2010, received the “Committee Prize Paper”, second prize, from the Electrical Machines Technical Committee of the IEEE Industrial Electronics Society.



Committee Prize Paper Certificate

*The Electrical Machines Technical Committee of the
IEEE Industrial Electronics Society
recognizes*

Oliver Magdun, Yves Gemeinder, and Andreas Binder

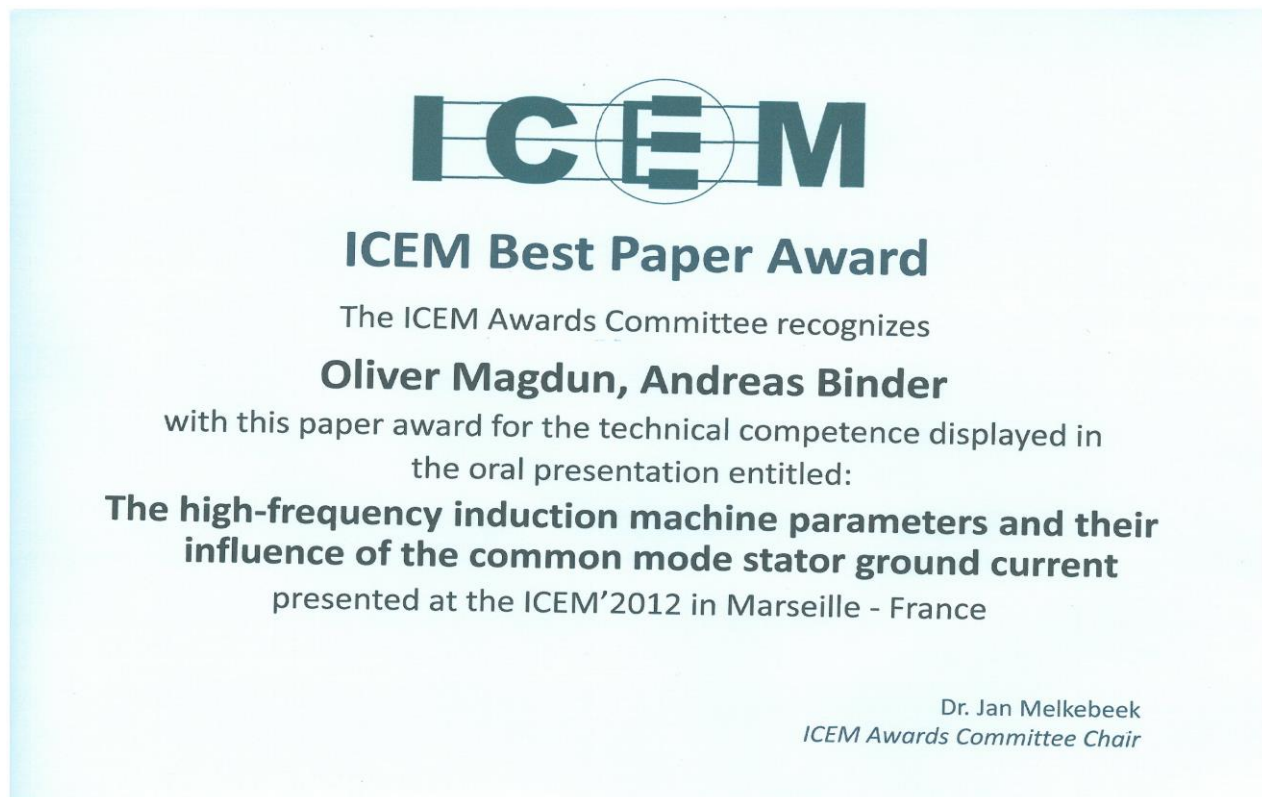
*with Second Prize for the technical competence displayed in
the paper entitled:*

**Prevention of Harmful EDM Currents in Inverter-Fed AC Machines by
Use of Electrostatic Shields in the Stator Winding Overhang**
presented at the 36th IECON. 7-10 November 2010, Glendale, AZ

EM Tech. Committee Chair Leila Parsa:

IES President Leopoldo Garcia Franquelo:

5.4. The paper “The high-frequency induction machine parameters and their influence of the common mode stator ground current”, written by O. Magdun and A. Binder, presented at the XXth International Conference on Electrical Machines ICEM’12, 2-5 September 2012, received the “ICEM Best Paper Award”, from the ICEM Awards Committee.



6.1. Subproject 1: Bearing impedance and bearing damage due to bearing currents in inverter-fed electrical machines

Dipl.-Ing. Oliver Magdun
 Dipl.-Ing. Yves Gemeinder
 Prof. Dr.-Ing. habil. Dr. h.c. Andreas Binder
 Institut für Elektrische Energiewandlung, TU Darmstadt
 E-Mail: omagdun@ew.tu-darmstadt.de, ygemeinder@ew.tu-darmstadt.de

1.1. Summary

During this project, a large number of ball bearings, ca. 400 bearings for inverter-fed 4-pole squirrel cage induction motors of 1.5 kW and 11 kW rated powers, have been used to investigate the bearing degradation due to bearing currents in different conditions of the bearing operation: load, temperature and speed. After long time tests (500 hour and 1000 hour), each bearing race of the tested bearings was analyzed with a light microscope to determine the state of the bearing. Based on these experimental tests, the convenient bearing operating conditions have been established.

The main indicators of the electrical bearing life, the apparent bearing current density and the discharge energy, were calculated and analyzed in comparison with the bearing degradation. For apparent bearing current densities less than 0.3 A/mm^2 no bearing damages were found, whereas for larger values than 0.8 A/mm^2 pitting was found on the bearing race. It has been found that a current density of $0.3 \text{ A/mm}^2 \dots 0.8 \text{ A/mm}^2$ may indicate a failure, but only if a large

number of discharges occur inside the bearings and the average discharge energy is of at least 2 nJ per one discharge. In the performed tests, no fluting was found due to EDM currents.

In parallel to the bearing degradation tests, the bearing impedance has been measured at frequencies between 1 kHz ... 30 MHz. The parameters of the steady state electrical bearing model have been determined. The steady state bearing impedance model cannot be directly used to calculate the EDM currents. For that, the electrical discharges inside the bearing have to be modeled by a switch that adds an additional bearing arc resistance in parallel to the steady state bearing impedance model. For the tested bearings, the bearing arc resistance was determined, in order of 10 Ω ... 20 Ω .

1.2. Work schedule and methods:

months	Duration in months		Content
	7	(A)	Construction and manufacturing of 4 bearing test rigs
1	1	(A1)	Construction of the bearing test rigs at frame size 90 mm and 160 mm
2-3	2	(A2)	Mechanical and electrical set up of the first test rig, starting of the test runs: Test rig 1 – frame size 160 mm (especially prepared motors are available from previous work)
4-7	4	(A3)	- Construction of the 3 further test rigs - Starting of the long-term test runs - In parallel buying of the test specimen, training for measurement
	26	(B)	Long term tests: 64 „1000h“-Tests with roller ball bearings as four parallel measurement series, 16 sequential test runs
8-33	26	(B1)	Work in parallel to Section C: for 2.5 years: - Mounting of the bearings in test rigs - Operation and the monitoring of the tests - Measurement of bearing currents, speed, temperature, vibration, bearing force - Dismounting and microscope measurement of the bearings
8-33	26	(B2)	Measurement of the bearing impedance at the beginning and end of the 1000h-Test at the selected set of operation parameters (no bearing current)
8-12	5	(C)	Analytical modelling of roller ball bearings: Based on literature, set up of models, comparison to measurement of $Z_b(f)$
13-20	8	(D)	Numerical modelling of roller ball bearings: Calculation of the HF current flow with skin effect and different contact points at different frequencies. The results may be used for correcting the analytical models.
21-26	6	(E)	Test of known facts to the generation of fluting: Systematic evaluation of the test results – what are the failure mechanisms? What are the dominating influencing parameters?
27-33	7	(F)	Combination of the HF bearing equivalent circuit with the existing HF models of the stator winding and the motor frame: Simulation of the bearing currents
34-36	3		Final report

1.3. Short description of the research work:

- **Construction and manufacturing of 4 bearing test rigs:** Construction of the bearing test rigs is presented in Section 2.2. Squirrel-cage induction machines of the same power, 4-pole 1.5 kW and 11 kW, have been selected for the 4th bearing test rigs.

- **Long term tests: 64 „1000h“-Tests with roller ball bearings as four parallel measurement series, 16 sequential test runs:** For detection of bearing failures caused by EDM currents and rotor-to-ground currents, 500 and 1000 hours tests have been performed for the 1.5 kW and 11 kW induction machines at different bearing temperatures, speeds and loads (Section 2.3 and 2.7):

a) 112 EDM current tests (Table 2.3-1a, Section 2.3) were performed with the 90 mm test rigs (1.5 kW induction machines), and 110 EDM current tests (Table 2.3-1b, Section 2.3) were performed with the 160 mm test rigs (11 kW induction machines);

b) 54 rotor-to-earth current tests were performed with the 90 mm test rigs (Table. 2.7-1, Section 2.7) and 39 rotor-to-earth current tests were performed with the 160 mm test rigs (Table. 2.7-2, Section 2.7).

- **Analytical modelling of roller bearings:** The analytical steady state bearing circuit model is made by series and parallel connections of the inner and outer bearing resistances and capacitances of each ball (Section 2.6). For calculation of the EDM currents, a bearing arc resistance has to be added by a switch that simulates the electric discharges, in parallel to the equivalent bearing capacitance. By measuring the peak-to-peak EDM current and the threshold bearing voltage, the bearing arc resistance has been determined in Section 2.5.3.

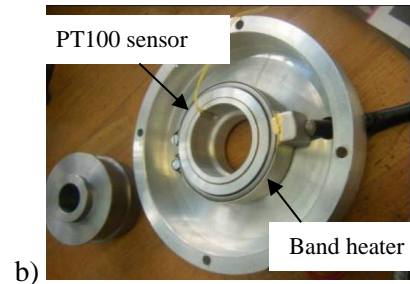
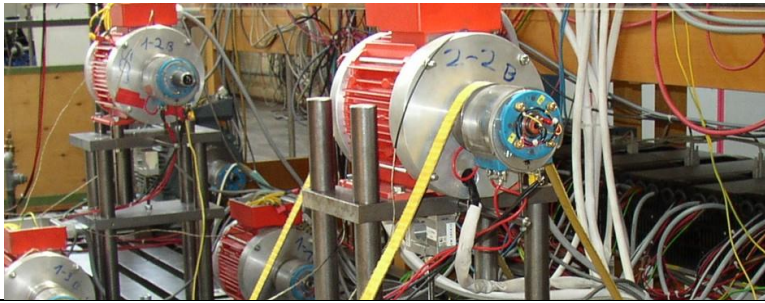
- **Measurement of bearing impedances:** The bearing impedances have been measured with an *LCR*-meter at different frequencies, different bearing operating conditions and two different lubricants (Section 2.5).

- **Numerical modelling of roller ball bearings:** the analytical and numerical calculation of the bearing capacitances has been presented in the DFG FOR 575, Annual Report 2009. A harmonic bearing model has been tested to check the influence of the skin effect on the ball bearing resistance and inductance. In the MHz frequency range, the obtained results showed a negligible inductance and a very small resistance, in order of m Ω .

- **Test of known facts to the generation of fluting:** A systematic evaluation of the test results was conducted for the EDM and rotor-to-ground current tests. The results of the EDM current test are presented for 112 tests with the 1.5 kW induction machines (Table 2.3-1a, Section 2.3) and 110 tests with the 11 kW induction machines (Table 2.3-1b, Section 2.3). The indicators for predicting the bearing failures due to EDM currents were calculated (Section 2.4). The rotor-to-ground current tests are presented for 29 tests with the 1.5 kW induction machines (Table 2.7-1, Section 2.7) and 28 tests with the 11 kW induction machines (Table 2.7-2, Section 2.7).

- **Combination of the HF bearing equivalent circuit with the existing HF models of the stator winding and the motor frame:** a new high frequency time-domain model of the induction machine has been proposed for calculating the common mode and bearing voltage (Section 2.4.1). By considering the bearing operating conditions (temperature, speed and load) the threshold bearing voltage is calculated in Section 2.4.2. An equivalent circuit model, including the rotor-to-stator frame capacitances and the shaft resistance and inductance has been combined with the bearing capacitances and the bearing arc resistances in order to calculate the EDM currents and the discharge energy (Section 2.4.3).

2.1. Introduction



During the last years, the bearing failures in inverter-fed electrical machines due to bearing currents have been researched at the Institute for Electrical Energy Conversion, TU Darmstadt. In the lab, as well as in industrial applications, it was noted that at the same bearing current flow, in some cases, a stable grey bearing trace condition was reached, whereas in other cases, fluting and severe pitting was observed with increased noise and vibration in the machines. The reason for that remained hidden, so a more thoroughly performed experiment was performed in this research to give more insight into the development of the bearing damages caused by bearing currents in different bearing operating conditions.

2.2. An experimental test bench for adjustment and measurement of bearing operating parameters

A. Adjustment and measurement of bearing loads

Two test benches of 3 x 1.5 kW induction machines and two test benches of 3 x 11 kW induction machines were built in similar mechanical structures to simulate different operating conditions of the machine bearings. Fig. 2.2-1a shows the two test benches with three 4-pole, 50 Hz squirrel cage induction machines of 1.5 kW rated power each of them, having the same ball bearings - type 6205 C3 in the both sides: (DE) drive-end and (NDE) non-drive-end. The NDE is built in a way that the NDE bearing seat can move to compensate the construction tolerances and the temperature expansion. Taking different springs at the NDE, the axial force acting on the machine bearings is modified. In order to obtain different radial forces, at the DE and NDE bearings, two belt-pulley systems are used to connect the three machines at each side.

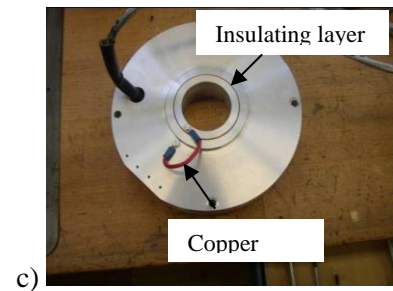


Figure 2.2-1 a) Bearing loading system built with three identical 1.5 kW squirrel-cage induction machines
 b) Modified motor shield with a band heater for the temperature control and the PT100 sensor mounted on the shield for measurements of temperatures at the bearing outer surface, and c) Insulating layer and copper loop for measurements of EDM currents

Two machines are placed on a fix base support and the third machine is placed on a frame with a changeable position, up or down. Modifying the frame position, the radial forces acting on the bearings can be adjusted. The total loading force is measured and counted with an acquisition system which is arranged in the middle of the variable support frame. Based on the measured forces, the radial forces, acting on each motor bearing, are calculated with a mechanical model of the test bench [3]. The bearing loading system and the measurement system are built to avoid the electrical connections between the tested machines or ground.

B. Adjustment and measurement of bearing temperatures

At no-load running conditions, the bearing temperature cannot normally increase at any wanted value. To control the bearing temperature, the original end-shields of the induction motors of 1.5 kW are replaced with new shields which are manufactured such as the bearings can be heated up externally by cylindrical band heaters (Fig. 2.2-1b). A PT100 temperature sensor is placed on the inner bore shield surface to measure the temperature of the outer bearing race and another sensor is placed on the outer shaft surface, under the bearing seat, to measure the temperature of the inner bearing race. By contact rings, the acquisition measurement system is connected to the PT100 sensors. A bore is done into the rotor shaft to take out the connecting wires from the shaft sensors. The system allows accurate measurements of temperatures up to a shaft speed of 3000 rpm.

C. Measurement of EDM currents

An insulating layer is inserted into the end-shields of the DE and NDE bearings to create an electrical separation of the bearings from the stator frame (Fig. 2.2-1c). A copper loop bridges the insulation, and gives the current path where the EDM bearing currents are indirectly measured. The methodology for measurements of the EDM currents is largely described in [4].

2.3. Tests for evaluation of bearing failures caused by EDM currents

The EDM bearing current damage assessment has been performed for:

- a) a 90 mm test bench:
 - 3 x 1.5 kW induction machines
 - 6 bearings for each cycle of tests
 - 16 different settings and 6 bearings per setting results in 96 tests
 - a single test at the beginning (the sum of tests increases from 96 to 112)
 - 6 bearings tested every month
 - 10 month test time – 60 bearings each year

b) a 160 mm test bench:

- 3 x 11 kW induction machines
- 6 bearings for each cycle of tests
- 16 different settings and 6 bearings per setting results in 96 tests
- a single test at the beginning (the sum of tests increases from 96 to 110)
- 6 bearings tested every month
- 10 month test time – 60 bearings each year

Table 2.3-1 shows the overview of the performed tests for the 1.5 kW machine (a), and 11 kW machine bearings (b). The bearings were monitored by daily measurements of the EDM currents. The average peak-to-peak EDM current value and the discharge activity were permanently counted during the tests [4], [5]. After 500 hours, the machine bearings were disassembled from the shaft and the bearing races were sectioned in order to identify the grey race, the pitting or the fluting. The bearing race was analyzed with a light microscope and a digital camera with an optical resolution of 0.003 mm per pixel. The lubricant was collected and stored for further possible chemical investigations.

According to the assessment tests of Table 2.3-1, the behavior of the bearing degradation for the 1.5 kW and 11 kW induction machine bearings is presented in Tables 2.3-2, 2.3-3, 2.3-4 and 2.3-5 for different steady-state bearing operation conditions: “low (L)” and “high (H)” radial (F_r) and axial (F_a) bearing loads: $F_r/F_a = 63 \text{ N}/50 \text{ N}$ and $F_r/F_a = 240 \text{ N}/50 \text{ N}$, “L” and “H” speeds: 450 rpm and 1500 rpm and “L” and “H” bearing temperatures: $\sim 60^\circ\text{C}$ and 100°C . Reducing of the crater size is shown there by a red arrow. The degree of degradation of the bearings type 6205 C3 of the inverter-fed 1.5 kW machines is presented together with the main indicators for predicting the bearing failures: the “apparent” EDM current density J_b and the discharge energy W_t in Table 2.3-6. The methods for their calculation are presented in Section 2.4.4. The width of the gray race w_r , the number of craters with a diameter bigger than $0.3 \mu\text{m}$ and the biggest crater diameter d_c are also given in Table 2.3-6, and the corresponding photos of the bearing race are given in Fig. 2.3-1. Based on the bearing race inspection, the bearing degradation was appreciated with (+)(+): high, (+), (-), and (-)(-): low. Cases with uncertain degradations are denoted with 0. In setting 1c, Fig. 2.3-1, the highest degree of degradation from all the tested bearings was identified. It has occurred for an apparent bearing current density of $0.8 \text{ A}/\text{mm}^2$. For apparent bearing current densities less than $0.3 \text{ A}/\text{mm}^2$, the bearing race was clean. Between $0.3 \text{ A}/\text{mm}^2$ and $0.8 \text{ A}/\text{mm}^2$, the prediction of the bearing failures was uncertain. Pitting on the bearing race and big craters have been found for two of the settings (1d and 2c, Fig. 2.3-1), whereas for one setting (1a, Fig. 2.3-1), the bearing race was clean. A current density between $0.3 \text{ A}/\text{mm}^2$ and $0.8 \text{ A}/\text{mm}^2$ may indicate a bearing failure for, when a large number of discharges occur inside the bearings and the average discharge energy becomes larger than 2 nJ per one discharge. For the setting 1c, Fig. 2.3-1, the worst case of the 500 hours test was found: 36 discharges per 10 ms and a large discharge energy of 20 nJ for a single discharge.

Table 2.3-1a EDM current tests performed for the 1.5 kW induction machines at different operating parameters.

	Setting 1	Setting 2	Setting 3	Setting 4	Setting 5	Setting 6	Setting 7	Setting 8
Speed	1500 rpm (H)							
Axial Bearing Load	50 N (L)	150 N (H)						
Radial Bearing Load	63 N (L)	63 N (L)	63 N (L)	63 N (L)	270 N (H)	270 N (H)	270 N (H)	270 N (H)
Bearing Temperature	58 °C (L)	57 °C (L)	100 °C (H)	100 °C (H)	55 °C (L)	54 °C (L)	100 °C (H)	100 °C (H)
Number of Bearings Measured	8	8	8	6	8	8	8	6

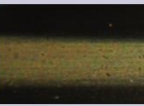
	Setting 9	Setting 10	Setting 11	Setting 12	Setting 13	Setting 14	Setting 15	Setting 16
Speed	450 rpm (L)							
Axial Bearing Load	50 N (L)	150 N (H)						
Radial Bearing Load	63 N (L)	63 N (L)	63 N (L)	63 N (L)	270 N (H)	270 N (H)	270 N (H)	270 N (H)
Bearing Temperature	50 °C (L)	53 °C (L)	100 °C (H)	100 °C (H)	51 °C (L)	52 °C (L)	100 °C (H)	100 °C (H)
Number of Bearings Measured	6	6	6	6	8	8	8	6

Table 2.3-1b EDM current tests performed for the 11 kW induction machines at different operating parameters.

	Setting 1	Setting 2	Setting 3	Setting 4	Setting 5	Setting 6	Setting 7	Setting 8
Speed	1500 rpm (H)	1500 rpm (H)	1500 rpm (H)	1500 rpm (H)				
Axial Bearing Load	240 N (L)	720 N (H)	240 N (L)	720 N (H)	240 N (L)	720 N (H)	240 N (L)	720 N (H)
Radial Bearing Load	325 N (L)	325 N (L)	325 N (L)	325 N (L)	995 N (H)	995 N (H)	995 N (H)	995 N (H)
Bearing Temperature	62 °C (L)	59 °C (L)	100 °C (H)	100 °C (H)	e.g. 60 °C (L)	e.g. 60 °C (L)	100 °C (H)	100 °C (H)
Number of Bearings Measured	8	8	8	8	6	6	6	6

	Setting 9	Setting 10	Setting 11	Setting 12	Setting 13	Setting 14	Setting 15	Setting 16
Speed	450 rpm (L)	450 rpm (L)	450 rpm (L)					
Axial Bearing Load	240 N (L)	720 N (H)	240 N (L)	720 N (H)	240 N (L)	720 N (H)	240 N (L)	720 N (H)
Radial Bearing Load	325 N (L)	325 N (L)	325 N (L)	325 N (L)	995 N (H)	995 N (H)	995 N (H)	995 N (H)
Bearing Temperature	62 °C (L)	59 °C (L)	100 °C (H)	100 °C (H)	61 °C (L)	e.g. 60 °C (L)	100 °C (H)	100 °C (H)
Number of Bearings Measured	8	8	8	6	6	6	6	6

Table 2.3-2 View of the outer DE bearing race with measured crater sizes, measured grey trace and the calculated average current density after a test duration of 500 h at the 1.5 kW induction test bench

Radial Load Axial Load	63 N 50 N	63 N 150 N	240 N 50 N	240 N 150 N
Width Grey Race: Biggest Crater Size: Ø Current Density: Speed: 1500 rpm Bearing Temperature: ca. 62 °C	1,64 mm 0,21 mm 0,84 A/mm² 	1,35 mm 0,06 mm 0,28 A/mm² 	1,16 mm 0,06 mm 0,41 A/mm² 	1,78 mm 0,15 mm 0,3 A/mm² 
Setting:	1	2	5	6
Width Grey Race: Biggest Crater Size: Ø Current Density: Speed: 1500 rpm Bearing Temperature: 100 °C	1,74 mm 0,17 mm 0,59 A/mm² 	1,2 mm 0,06 mm 0,39 A/mm² 	1 mm 0 mm 0,33 A/mm² 	1,54 mm 0,04 mm 0,33 A/mm² 
Setting	3	4	7	8

Radial Load Axial Load	63 N 50 N	63 N 150 N	240 N 50 N	240 N 150 N
Width Grey Race: Biggest Crater Size: Ø Current Density: Speed: 450 rpm Bearing Temperature: e.g. 59 °C	0 mm 0 mm 0,44 A/mm² 	1,25 mm 0 mm 0,4 A/mm² 	1,1 mm 0 mm 0,51 A/mm² 	1,06 mm 0,13 mm 0,21 A/mm² 
Setting:	9	10	13	14
Width Grey Race: Biggest Crater Size: Ø Current Density: Speed: 450 rpm Bearing Temperature: 100°C	1,26 mm 0 mm 0,5 A/mm² 	0,86 mm 0,04 mm 0,24 A/mm² 	0 mm 0 mm 0,24 A/mm² 	0,98 mm 0 mm 0,2 A/mm² 
Setting	11	12	15	16

Table 2.3-3 View of the DE inner bearing race with measured crater sizes, measured grey trace and the calculated average current density after a test duration of 500 h at the 1.5 kW induction test bench

Radial Load Axial Load	63 N 50 N	63 N 150 N	240 N 50 N	240 N 150 N
Width Grey Race: Biggest Crater Size: Ø Current Density: Speed: 1500 rpm Bearing Temperature: ca. 62 °C	1,64 mm 0,17 mm 0,84 A/mm² 	2 mm 0,13 mm 0,28 A/mm² 	1,52 mm 0,26 mm 0,41 A/mm² 	2,09 mm 0,26 mm 0,3 A/mm² 
Setting:	1	2	5	6
Width Grey Race: Biggest Crater Size: Ø Current Density: Speed: 1500 rpm Bearing Temperature: 100°C	1,4 mm 0,12 mm 0,59 A/mm² 	1,61 mm 0,05 mm 0,39 A/mm² 	1,38 mm 0,14 mm 0,33 A/mm² 	2,69 mm 0,06 mm 0,33 A/mm² 
Setting	3	4	7	8

Radial Load Axial Load	63 N 50 N	63 N 150 N	240 N 50 N	240 N 150 N
Width Grey Race: Biggest Crater Size: Ø Current Density: Speed: 450 rpm Bearing Temperature: e.g. 59 °C	0 mm 0 mm 0,44 A/mm² 	2,14 mm 0 mm 0,4 A/mm² 	1,15 mm 0,09 mm 0,51 A/mm² 	2,12 mm 0,16 mm 0,21 A/mm² 
Setting:	9	10	13	14
Width Grey Race: Biggest Crater Size: Ø Current Density: Speed: 450 rpm Bearing Temperature: 100°C	0 mm 0 mm 0,5 A/mm² 	1,32 mm 0,06 mm 0,24 A/mm² 	0 mm 0 mm 0,24 A/mm² 	1,23 mm 0 mm 0,2 A/mm² 
Setting	11	12	15	16

Table 2.3-4 View of the outer DE bearing race with measured crater sizes, measured grey trace and the calculated average current density after a test duration of 500 h at the 11 kW induction test bench

Radial Load Axial Load	325 N 240 N	325 N 720 N	995 N 240 N	995 N 720 N
Width Grey Race: Biggest Crater Size: Ø Current Density: Speed: 1500 rpm Bearing Temperature: ca. 62 °C	1.27 mm 0.54 mm 0.22 A/mm ² 	2 mm 0.09 mm 0.052 A/mm ² 	1.73 mm 0 mm 0.11 A/mm ² 	2.13 mm 0.11 mm 0.04 A/mm ² 
Setting:	1	2	5	6
Width Grey Race: Biggest Crater Size: Ø Current Density: Speed: 1500 rpm Bearing Temperature: 100 °C	1.95 mm 0.09 mm 0.13 A/mm ² 	2.39 mm 0 mm 0.047 A/mm ² 	2 mm 0 mm 0.09 A/mm ² 	1.93 mm 0 mm 0.04 A/mm ² 
Setting	3	4	7	8

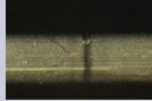
Radial Load Axial Load	325 N 240 N	325 N 720 N	995 N 240 N	995 N 720 N
Width Grey Race: Biggest Crater Size: Ø Current Density: Speed: 450 rpm Bearing Temperature: e.g. 59 °C	1.03 mm 0.19 mm 0.14 A/mm ² 	1.6 mm 0 mm 0.05 A/mm ² 	1.46 mm 0 mm 0.05 A/mm ² 	1.14 mm 0.1 mm 0.03 A/mm ² 
Setting:	9	10	13	14
Width Grey Race: Biggest Crater Size: Ø Current Density: Speed: 450 rpm Bearing Temperature: 100°C	1.62 mm 0.09 mm 0.11 A/mm ² 	1.28 mm 0 mm 0.07 A/mm ² 	1.3 mm 0 mm 0.04 A/mm ² 	2.06 mm 0 mm 0.03 A/mm ² 
Setting	11	12	15	16

Table 2.3-5 View of the DE inner bearing race with measured crater sizes, measured grey trace and the calculated average current density after a test duration of 500 h at the 1.5 kW induction test bench

Radial Load Axial Load	325 N 240 N	325 N 720 N	995 N 240 N	995 N 720 N
Width Grey Race: Biggest Crater Size: Ø Current Density: Speed: 1500 rpm Bearing Temperature: ca. 62 °C	1.05 mm 0.95 mm 0.22 A/mm ² 	2.83 mm 0.11 mm 0.08 A/mm ² 	2.81 mm 0 mm 0.05 A/mm ² 	3.49 mm 0.17 mm 0.04 A/mm ² 
Setting:	1	2	5	6
Width Grey Race: Biggest Crater Size: Ø Current Density: Speed: 1500 rpm Bearing Temperature: 100 °C	1.78 mm 0.09 mm 0.13 A/mm ² 	3.53 mm 0.04 mm 0.03 A/mm ² 	2.9 mm 0 mm 0.05 A/mm ² 	2.31 mm 0 mm 0.04 A/mm ² 
Setting	3	4	7	8

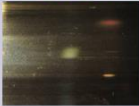
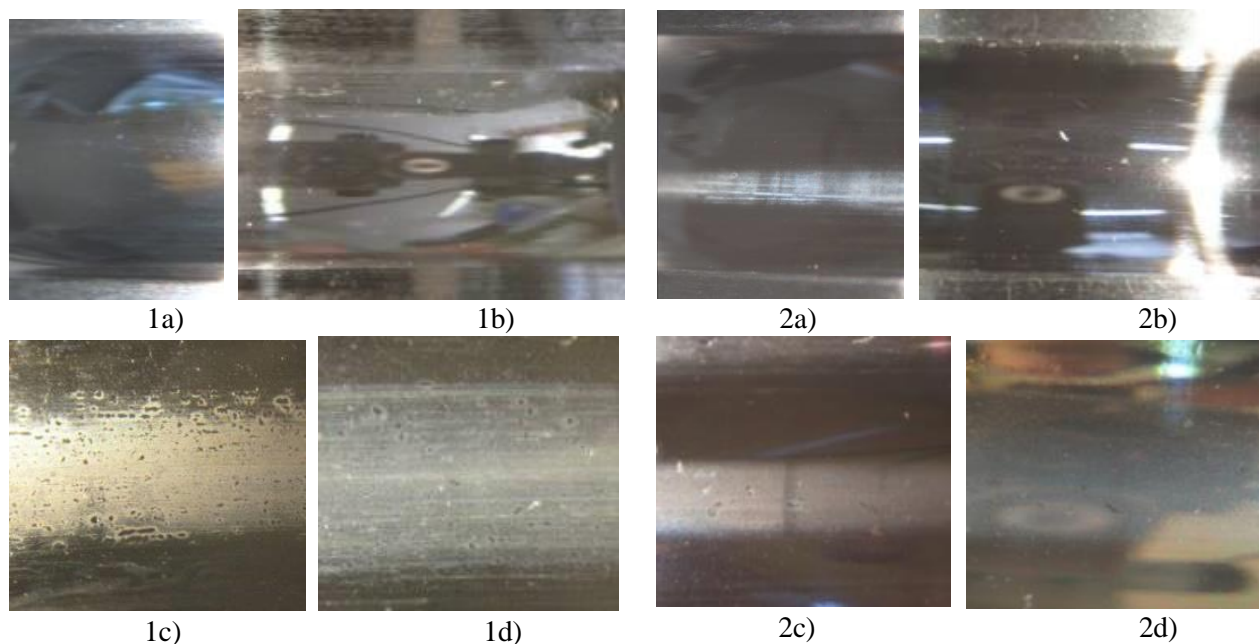
Radial Load Axial Load	325 N 240 N	325 N 720 N	995 N 240 N	995 N 720 N
Width Grey Race: Biggest Crater Size: Ø Current Density: Speed: 450 rpm Bearing Temperature: e.g. 59 °C	1.04 mm 0.1 mm 0.14 A/mm ² 	1.63 mm 0.04 mm 0.05 A/mm ² 	0.82 mm 0 mm 0.05 A/mm ² 	1.12 mm 0 mm 0.03 A/mm ² 
Setting:	9	10	13	14
Width Grey Race: Biggest Crater Size: Ø Current Density: Speed: 450 rpm Bearing Temperature: 100°C	1.03 mm 0.06 mm 0.11 A/mm ² 	2.81 mm 0 mm 0.07 A/mm ² 	1.76 mm 0 mm 0.04 A/mm ² 	3.3 mm 0 mm 0.04 A/mm ² 
Setting	11	12	15	16

Table 2.3-6 Indicators for bearing failures and the degree of damage of the bearing race of the bearings type 6205 C3 of the 1.5 kW machine.

Setting	-	1a	1b	1c	1d	2a	2b	2c	2d
F_r	N	63	63	63	63	240	240	240	240
F_a	N	50	50	50	50	50	50	50	50
n	rpm	450		1500		450		1500	
ϑ_b	°C	62	100	65	100	51	100	55	100
J_b	A/mm ²	0.44	0.29	0.84	0.59	0.51	0.24	0.41	0.32
DA (500 h)	-	$4.5 \cdot 10^6$	$1460 \cdot 10^6$	$6555 \cdot 10^6$	$5227 \cdot 10^6$	$2104 \cdot 10^6$	$1020 \cdot 10^6$	$1504 \cdot 10^6$	$2169 \cdot 10^6$
W_t (500 h)	J	0.06	2.49	32.7	15.69	5.27	0.77	15.96	8.73
w_r	mm	-	-	1.64	1.4	1.15	-	1.52	1.38
d_c	mm	-	-	0.17	0.12	0.09	-	0.26	0.14
Number of craters	-	0	0	239	107	30	0	58	6
Degree of degra- dation	-	(-) (-)	(-) (-)	(+) (+)	(+)	0	(-) (-)	(+)	0

**Figure 2.3-1** Inner race of the bearings type 6205 C3, after 500 hour tests, when different steady-state loads, temperatures and speeds were applied (settings: 1a, 1b, 1c, 1d, 2a, 2b, 2c and 2d of Table 2.3-6).

It has been observed that the bearing temperature increase reduces the degree of degradation of the bearing race. In the worst case of the bearing operation (Fig. 2.3-1, setting 1c), by increasing the bearing temperature from 60°C to 100°C, the number of craters and their diameters were reduced (Fig. 2.3-1, setting 1d). With the bearing temperature increasing, the lubricant thickness decreases. Thus, the arcing effect will occur at lower bearing voltages and smaller EDM currents:

$h_{\min} \sim v_{\text{TH}} \sim i_b$ (Section 2.4-2).

A significant degradation of the bearing race was found at lower speeds, temperatures, at bearing loading with $F_r/F_a \approx 1$ (Fig. 2.3-1, setting 1c). A convenient change of the bearing temperature and of the axial and radial bearing loads F_r and F_a may prevent the early bearing damage. For $F_r/F_a \gg 1$ and 100°C bearing temperature, the number of craters has strongly decreased (Fig. 2.3-1, setting 2d). Therefore, the ratio of the radial and axial bearing load F_r/F_a influences the state of the bearing race and the electrical bearing life. This is caused by the *Hertz*'ian contact surface that depends on the ratio F_r/F_a (Fig. 2.3-2). If $F_r \gg F_a$, then the *Hertz*'ian contact surface between the roller ball elements and the inner bearing race is an ellipse (Fig. 2.3-2a & b). Else, if $F_r/F_a \approx 1$, then the *Hertz*'ian apparent contact and the high pressure contact surfaces (blue dark) deviates to smaller triangle surfaces (Fig. 2.3-2c). The apparent bearing current density increases.

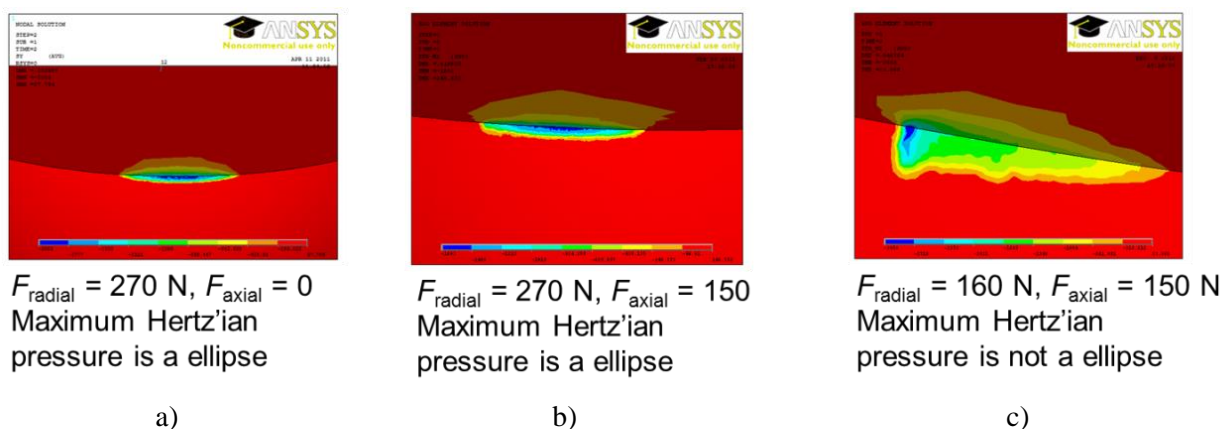


Figure 2.3-2 Calculation of the *Hertz*'ian area between a ball and bearing raceway, with the 3D ANSYS software, for different axial and radial bearing loads at zero speed. No lubricant was considered between the ball and bearing raceway.

During 500 hour tests no ripple was observed at the races of the tested bearings. In one case (setting 2c), the change of the race colour might be the start of the ripple forming. There, the biggest crater with a diameter of 0.26 mm was measured.

2.4. Calculation of bearing threshold voltage, EDM currents and discharge energy for predicting the bearing failures

Once the induced voltages on the motor bearings exceed the breakdown voltage of the lubricant, they discharge through the bearings, causing the EDM currents [1], [6], [7]. The product of the instantaneous EDM current and the arc voltage results, by integration over the discharge time, in the energy transmitted to the bearing race and roller elements where it heats, melts and vaporizes the material. Depending on the energy levels, craters with diameters of several 10 μm may be formed. If the craters are smaller than a few μm , they can be flattened by rollers; the bearing surface develops a grey race and the bearing operates stable. If the craters are larger, the pitting is generated and may cause the start of the fluting damage [2], [6]. A distinguish between the grey race, fluting or pitting is possible if the apparent bearing current density and the energy level generated by the arc discharge is known [6].

2.4.1. Calculation of bearing voltage

The bearing voltage v_b is the image of the stator common mode voltage v_{com} that is mirrored over the bearings via the machine capacitances [8]-[11]:

$$v_b = \frac{C_{WR}}{C_{WR} + C_{RS} + C_{bDE} + C_{bNDE}} \cdot v_{com} = BVR \cdot v_{com} \quad (1)$$

where C_{WR} is the stator winding-to-rotor capacitance, C_{RS} is the rotor-to-stator frame capacitance and C_{bDE} and C_{bNDE} are the drive-end (DE) and non-drive-end (NDE) bearing capacitances. The methods for their measurements and calculation were presented in [11].

The common mode voltage of (1) is given in [12] as:

$$v_{com} = \frac{\int i_{u,g} dt + \int i_{v,g} dt + \int i_{w,g} dt}{3 \cdot C_{WS}} \quad (2)$$

where C_{WS} is the stator winding-to-stator frame capacitance per phase, which provides the return path of the common mode (CM) stator ground current. The CM stator ground current is formed by the superposition of the current pulses $i_{u,g}$, $i_{v,g}$ and $i_{w,g}$, which are generated in the inverter-fed AC machine, when the line-to-ground voltages $v_{u,g}$, $v_{v,g}$ and $v_{w,g}$ are switched between the two levels $\pm \frac{1}{2} V_{DC}$ of the inverter DC link voltage (Fig. 2.4-1). Each current pulse of the CM current, $i_{u,g}$, $i_{v,g}$

or $i_{w,g}$, can be calculated with a time-domain high-frequency equivalent circuit per phase of Fig. 2.4-2 as it has been described in [12]. In Fig. 2.4-2, the stator winding-to-stator frame capacitance $C_{WS} = C_{g1} + C_{g2}$ describes the behaviour of the motor at lower frequencies, in order of 10 kHz - 100 kHz, whereas the capacitance $C_{g1} = k_{cap} C_{WS}$ describes the behaviour of the motor at higher frequencies, in range of 1 MHz ... 10 MHz [12], [13]. The factor k_{cap} depends on the stator winding and the machine design. For the 1.5 kW induction machine, the capacitances $C_{g1} = 0.28$ nF and $C_{g2} = 1.07$ nF are determined in [13].

The capacitance $C_{WS} = C_{g1} + C_{g2}$ is connected to the ground via the laminated iron core, which is represented by the resistances and inductances R_{gk} , L_{gk} , $k = 1 \dots n$ of a ladder circuit with $n = 6$ branches (Table 2.4-2). In order to simulate the skin and proximity effects, at high frequency, the resistances and inductances of the stator winding are represented by the ladder circuits: R_{sk} , L_{sk} , $k = 1 \dots n$ of Table 2.4-3. They can be measured or calculated with the combined analytical and finite element methods of [12].

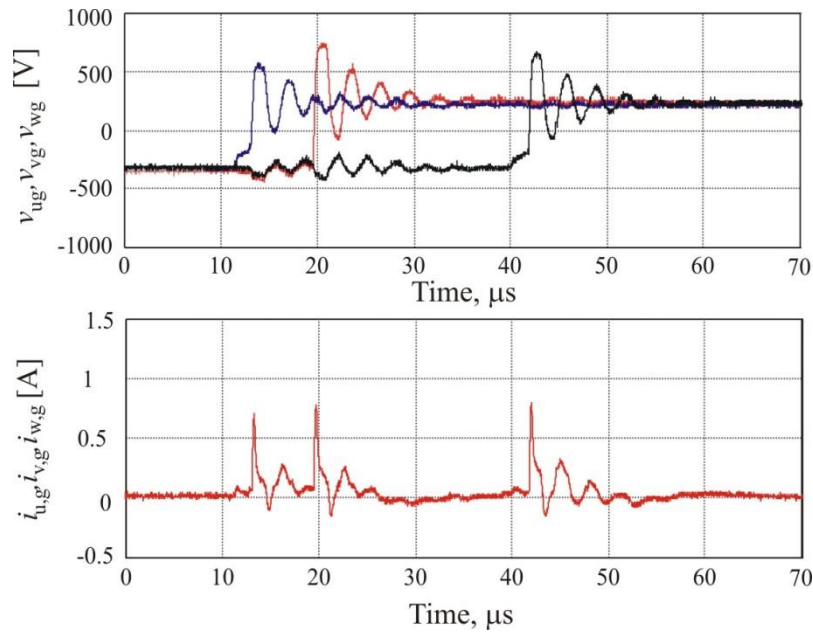


Figure 2.4-1 Measurements on the 1.5 kW induction machine used in the 500 hour test: (a) - Line-to-ground voltages at operation with 100 m unshielded motor cable, DC link voltage 560 V, 5 kHz switching frequency, (b) - CM stator ground current in the protective earth conductor.

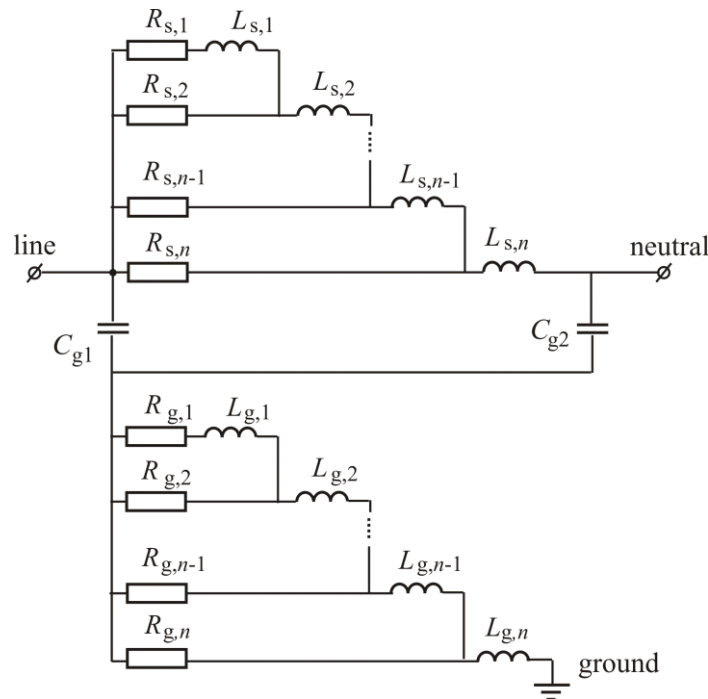


Figure 2.4-2. A time-domain high-frequency (HF) model per phase of the induction machines for calculation of CM stator ground currents and CM voltages [12].

Table 2.4-1 High-frequency capacitances [11] of the 1.5 kW induction machines of Fig. 2.2-1

n 1/min	C_{WR} pF	C_{RS} pF	$C_{bDE} + C_{bNDE}$ pF	BVR %
300	27.36	607.7	260	3.06
1500			170	3.4

Table 2.4-2 High-frequency representation of the laminated iron core [13] of the 1.5 kW induction machines of Fig. 2.2-1.

k	1	2	3	4	5	6
$R_{g,k}/\text{m}\Omega$	8.53	21.43	53.78	134.25	326.5	950.1
$L_{g,k}/\mu\text{H}$	1.37	0.55	0.22	0.10	0.05	0.01

Table 2.4-3 High-frequency representation of the stator winding [12] of the 1.5 kW induction machines of Fig. 2.2-1.

k	1	2	3	4	5	6
$R_{s,k}/\Omega$	31.25	10.64	43.0	120.01	561.47	9688.5
$L_{s,k}/\text{mH}$	4.98	0.52	0.69	2.01	8.06	2.42

2.4.2. Calculation of bearing threshold voltage

The threshold voltage v_{TH} is the magnitude of the capacitive voltage v_b across the bearing before the breakdown of the lubricant film. For the bearings type 6205 C3 of the 1.5 kW induction machine, lubricated with a standard mineral oil based on lithium soap (base oil viscosity of $80 \text{ mm}^2/\text{s}$ at 40°C), the breakdown of the lubricated film was determined for an electric field larger than $E = 30 \text{ kV/mm}$. For $E = v_{\text{TH}}/h_{\text{min}}$, the threshold voltage is estimated with respect to the minimum film thickness h_{min} :

$$v_{\text{TH}} = E \cdot h_{\text{min}} \quad (3)$$

The film thickness is almost constant along the contact surface h_c , but it is smaller at the outlet h_{min} (Fig. 2.4-3). It increases with the speed and decreases with the lubricant temperature. In optimal conditions of the bearing lubrication, i.e. for a minimum film thickness greater than the surface roughness, a not-too-high temperature, a not-too-low bearing load and a not-too-low or a high speed, the minimum film thickness h_{min} [m] and the central film thickness h_c [m] are calculated with the *Hamrock* and *Dowson's* equations [14]:

$$\begin{aligned} \frac{h_{\text{min}}}{R_{\text{eq}}} &= 3.63 \cdot U_{\text{ro}}^{0.68} \cdot G_o^{0.49} \cdot W_o^{-0.073} \cdot (1 - e^{-0.68 \cdot k}) \\ \frac{h_c}{R_{\text{eq}}} &= 2.69 \cdot U_{\text{ro}}^{0.67} \cdot G_o^{0.53} \cdot W_o^{-0.067} \cdot (1 - 0.61 \cdot e^{-0.73 \cdot k}) \\ U_{\text{ro}} &= \frac{v_o \cdot U_r}{E_{\text{eq}} \cdot R_{\text{eq}}}, \quad W_o = \frac{W}{E_{\text{eq}} \cdot R_{\text{eq}}^2}, \quad G_o = \alpha \cdot E_{\text{eq}} \end{aligned} \quad (4)$$

where v_o [Ns/m^2] is the absolute viscosity at the ambient temperature, α [m^2/N] is the viscosity-pressure coefficient, U_r [m/s] is the rolling speed, W [N] is the maximum bearing load at the contact of one rolling element, E_{eq} [N/m^2] is the equivalent modulus of elasticity, R_{eq} [m] is the equivalent contact radius of curvature in the plane of rotation and $k = b/a$ is the ellipticity parameter (Fig. 2.4-3a). The maximum static load, which is carried by one rolling element, is roughly estimated as $W \approx 5 \cdot F/N_b$, where N_b is the number of ball bearings and $F = X \cdot F_r + Y \cdot F_a$ is the equivalent load [N] at the bearing place. F_r and F_a are the radial and axial bearing loads [N], and X and Y are the radial and axial load factors, available from the bearing manufacturers.

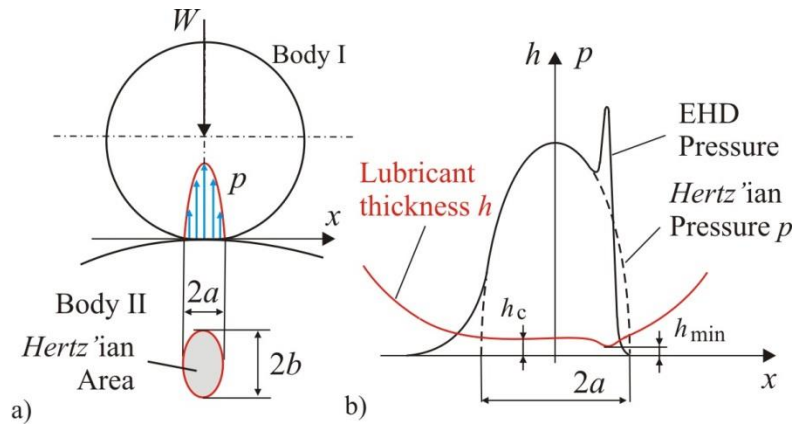


Figure 2.4-3 a) - Hertzian area $A_{Hz} = \pi ab$ and pressure p between a ball and the bearing outer raceway, b) - Lubricant thickness distribution and pressure in the Hertz's theory and the elastohydrodynamic (EHD) theory [14].

As the viscosity of the lubricant increases significantly with the pressure, the bearing load is strongly involved in the forming of the elastohydrodynamic lubricant film. In optimal conditions, the bearing load W has only a small influence on the lubricant thickness h_{min} . In some particular conditions of the bearing operation, as example for small loads and high temperatures, the starvation effect may already occur at a speed of 1000 rpm [15]. There, the calculation of the lubricant thickness with (4) is not valid and the experimental measurements of the lubricant thickness are necessary [15]. By keeping the optimal conditions of the bearing lubrication, the minimum and central lubricant thickness may be calculated with (4). Fig. 2.4-4 shows the calculated values of h_c and h_{min} for the bearings type 6205 C3 and the estimated threshold voltage for an electric field strength of $E = 30 \text{ kV/mm}$. At 60°C , and a speed of 450 rpm, the breakdown of the oil film occurs at a thickness of $0.12 \text{ }\mu\text{m}$, which corresponds to a bearing threshold voltage of 3.7 V (Fig. 2.4-5). So, one single pulse of the line-to-ground voltage between $\pm \frac{1}{2}V_{DC}$ may be used to calculate the bearing voltage.

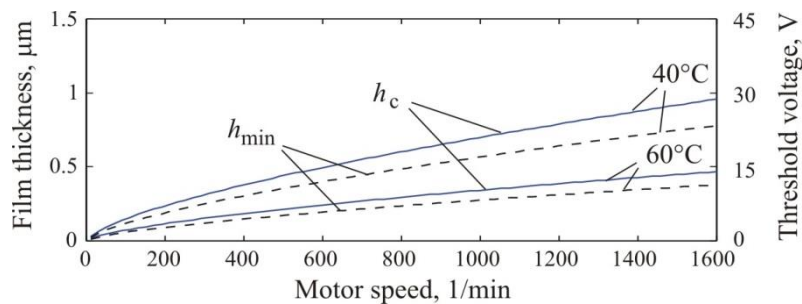


Figure 2.4-4 Calculated minimum and central film thickness for the 1.5 kW machine DE bearing with the Hamrock and Dowson's equations at an equivalent bearing load of $F = 160 \text{ N}$; the threshold voltage scale is set for a lubricant breakdown strength of 30 kV/mm .

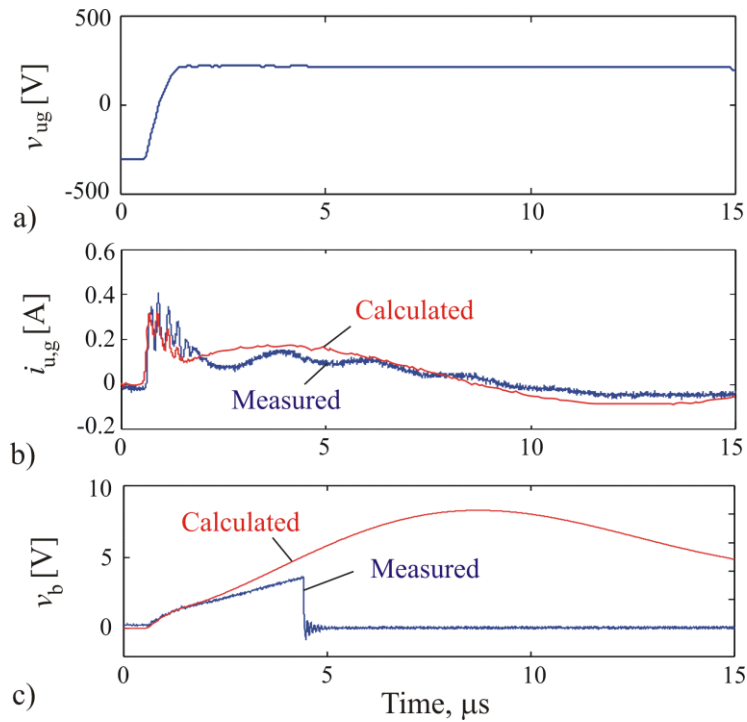


Figure 2.4-5 1.5 kW induction machine: a) - Measured line-to-ground voltage, b) - Measured and calculated CM stator ground current and c) - Measured and calculated bearing voltage at operation with 2 m cable length, 560 V DC link voltage, 5 kHz switching frequency.

As example, at 60°C and 450 rpm, for a $BVR \cong 3.0\%$ (Table 2.4-1), the bearing voltage can be calculated from the integral of the calculated CM current $i_{u,g}$, assuming $i_{v,g} = 0$ and $i_{w,g} = 0$ (Fig. 2.4-5):

$$v_b = BVR \cdot \frac{1}{3 \cdot C_{WS}} \int i_{u,g} dt \quad (5)$$

Because of the simplifications of the model of Fig. 2.4-2 [12], small differences may exist between the measured and calculated CM current. However, in the very first moment of the DC link voltage switching, the bearing voltage is well estimated. For a longer time, a better match is obtained when the measured CM current is used to calculate the bearing voltage [12]. Thereby, whenever the measurements of the common mode or bearing voltages are not possible, the CM stator ground current may be used to calculate them.

2.4.3. Calculation of EDM Current and Discharge Energy

A. Equivalent circuit representation

Electrically, a bearing can be modeled at larger speed than 10% of the motor rated speed, as a capacitance C_b , which is connected in parallel to a bearing arc resistance R_b , (Fig. 2.4-6). Compared with other inductances on the EDM current path, the inductive components of the bearings are very small, and therefore, they are neglected. As long as the bearing voltage v_b is less than the threshold voltage v_{TH} , the lubricant film insulates the contact surfaces between the roller and bearing outer and inner race, and only a small capacitive current may flow during the charging and discharging of the capacitance C_b . The bearing resistance R_b gets values in order of tens or hundreds of MΩ, depending on the lubricant resistivity (Section 2.5). When the threshold voltage is reached, an electric spark occurs, forming a plasma channel between the balls and bearing race. An increased current may flow through the discharge channel by means of the ions and electrons [16]. The electrical behavior of the discharge channel is described here by the discharge current-threshold voltage relationship, which is represented as a bearing arc resistance $R_b = R_b(h_{min})$ in the

electrical model of bearing. A switch is introduced in the bearing resistance branch to simulate the electric discharge, connecting in parallel the capacitances of the drive-end and non-drive-end bearings C_{bDE} and C_{bNDE} and the rotor-to-stator frame capacitance C_{RS} to the bearing arc resistance R_b . The switch models the behavior of the lubricant, which is non-conductive before breakdown, but becomes conductive immediately after breakdown. In Fig. 2.4-6, the rotor-to-stator frame capacitance C_{RS} is connected at the DE bearing where the discharge event is modeled. During the breakdown, the capacitances C_{bDE} , C_{RS} and C_{bNDE} discharge on the bearing arc resistance R_b .

When no discharges occur, the bearings are modeled by two capacitances C_{bNDE} and C_{bDE} , which at the same loading and temperature, are assumed to be equals $C_{bNDE} \cong C_{bDE} \cong 130$ pF [11]. The lubricant resistance is neglected, being in order of 100 M Ω . The two bearing capacitances are interconnected by the shaft resistance and inductance: $R_{Sh}(f)$ and $L_{Sh}(f)$. Fig. 2.4-7 shows the measured shaft resistance and inductance depending on the frequency f . For measurements, the rotor was inserted into the stator bore and separated from the stator lamination package by two insulating layers at the two rotor ends. Added at the stator frame, the end-shields had no noticeable influence on the shaft and rotor inductance and resistance. For the tested 1.5 kW machine, the stator frame impedance is much smaller than the shaft impedance, and it is therefore neglected. The measurement setup (Fig. 2.2-1c) is represented by the resistance $R_c = 6$ m Ω and the inductance $L_c = 0.06$ μ H of the copper litz wire loop and the insulating capacitances $C_{insDE} = 2.4$ nF and $C_{insNDE} = 2$ nF. Due to end-shields manufacturing, the insulating DE and NDE capacitances are different.

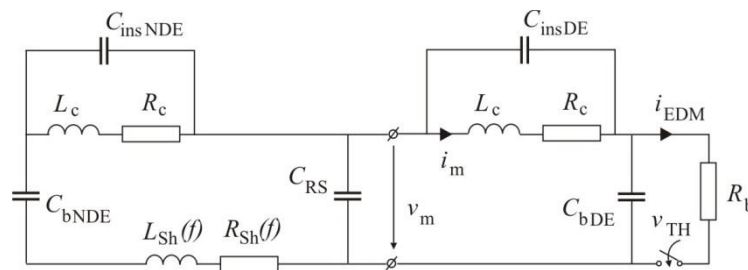


Figure 2.4-6 An equivalent circuit used for the calculation of EDM currents; the switch simulates a flashover at the DE bearing, connecting the DE bearing capacitance, the NDE bearing capacitance and the rotor-to-stator frame capacitance to the bearing resistance.

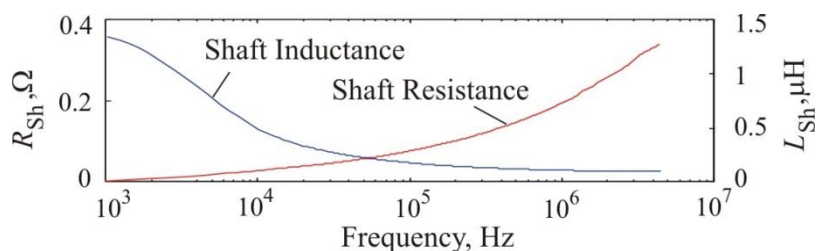


Figure 2.4-7 Measured shaft and rotor resistance and inductance for the 1.5 kW machine.

B. Measurements on bearing arc resistance

For a radial load $F_r = 63$ N and an axial load $F_a = 50$ N, acting on the machine bearings [8], the average of the maximum values of the peak-to-peak EDM current $i_{b,pp}$ (Fig. 2.4.8a) and the average of the maximum values of the peak-to-peak bearing voltage after the lubricant breakdown $v_{b,pp}$ (Fig. 2.4.8b) are measured. At each point of bearing operation, 50 discharges were counted from a single measurement and, in order to determine the average of the maximum values, the measurement was repeated 5 times. At different speeds and temperatures, 120 operating points

were selected, such as $30 \cdot 10^3$ measured values were taken into account to represent the current $i_{b,pp}$ and the voltage $v_{b,pp}$ in Fig. 2.4-6 a&b. Because of the bearing vibrations, polarization and breakdown mechanisms [16], the threshold voltage characteristic may show several fluctuations [8]. By neglecting these fluctuations and considering the real peak value of the EDM current $\hat{i}_b \approx \frac{2}{3} \cdot i_{b,pp}$ [4], and the threshold bearing voltage as $v_{TH} = \hat{v}_b \approx \frac{2}{3} \cdot v_{b,pp}$, the bearing arc resistance is roughly estimated at each operating point:

$$R_b = v_{TH} / \hat{i}_b = \hat{v}_b / \hat{i}_b \approx v_{b,pp} / i_{b,pp} \tag{6}$$

At the same temperature and bearing load, the bearing resistance R_b is almost constant until the “critical” lubricant thickness h_{cr} is surpassed (Fig. 2.4.9). When the lubricant thickness is smaller than the critical thickness h_{cr} , the peak value of the EDM bearing current is limited by a constant bearing resistance R_b in order of tens of ohms. When the lubricant thickness exceeds the critical thickness, the bearing resistance may increase and yield the decrease of the EDM current. Above an operating speed n_s , (larger than 2000 rpm, for $F_r/F_a = 63 \text{ N}/50 \text{ N}$, acting on the bearings type 6205 C3) the EDM currents get harmless peak-to-peak values.

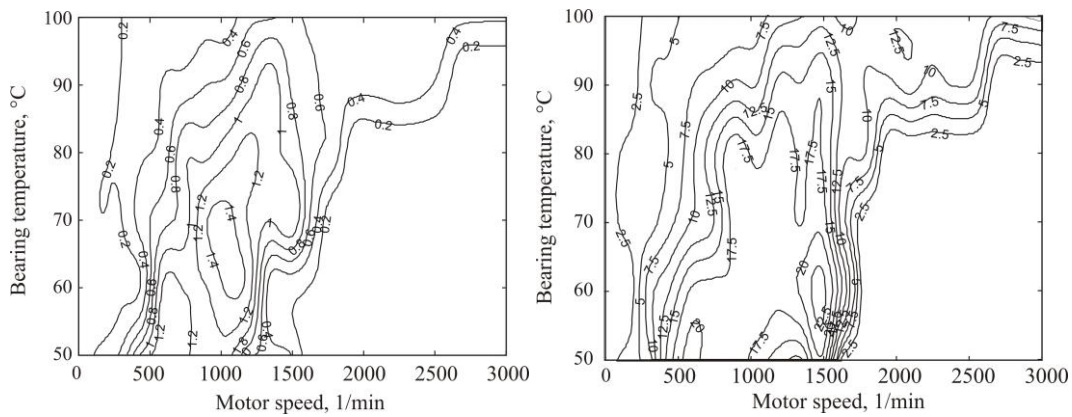


Figure 2.4.8 Equipotential lines of the measured a) - peak-to-peak EDM current (A) and b) – peak-to-peak bearing voltage (V), for the DE bearings type 6205 C3 of the 1.5 kW machine of Fig. 2.2.1, axially and radially loaded with $F_r/F_a = 63 \text{ N}/50 \text{ N}$.

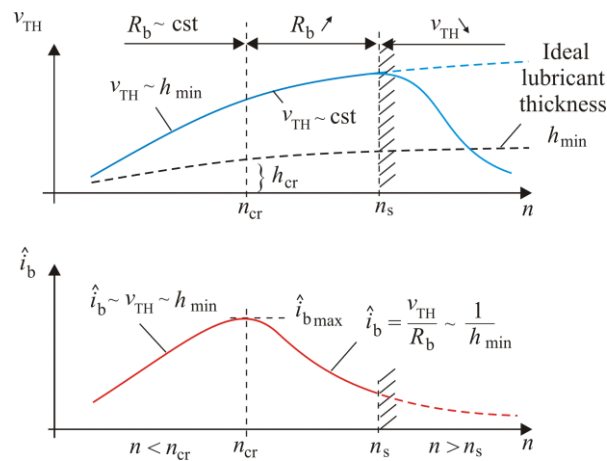


Figure 2.4.9 The EDM current – threshold voltage relationship at different steady state speeds. The bearing resistance is almost constant up to a critical speed n_{cr} , where the EDM currents reach their maximum. Depending on the bearing load and temperature, the lubrication effects and breakdown mechanisms occur at the speed n_{cr} , and the EDM current begins to decrease. After a speed n_s , the threshold voltage strongly decreases and the EDM current as well.

A method to calculate the EDM current-threshold voltage relationship is missing. For a particular case, the behavior of the conductive rough surfaces, separated by thin insulating films, was described in [17] with a mathematical model considering the film properties, current flow, surface topology, mechanical properties and contact loads. Since the electrical, thermal and mechanical mechanisms take place simultaneously, for the bearing lubricated surfaces, a more comprehensive study is necessary. Furthermore, when the speed n_{cr} is reached, the breakdown mechanisms or the lubrication effects may change the structure and consistency of the lubricant at the minimum contact point. The speed n_{cr} at which the EDM current begins to decrease, or the speed n_s at which the threshold voltage v_{TH} strongly decreases, are difficult to be predicted. Sometimes, for the bearings of the tested 1.5 kW machine, the speeds n_{cr} and n_s were very close one to each other.

C. EDM Currents - comparative results

For the 1.5 kW machine, operating at 300 rpm and a lubricant temperature of 40°C, the bearing voltage equals the threshold voltage at $v_{TH} = 8$ V, corresponding to a minimum lubricant thickness of 0.25 μm (Fig. 2.4-4). A bearing resistance of $R_b = 12 \Omega$, is determined for the best fitting between the measured EDM current i_m and the calculated one (Fig. 2.4-10). Thus: $\hat{i}_b = v_{TH}/R_b = 8 \text{ V}/12 \Omega = 0.67 \text{ A} \cong 2/3 \cdot i_{b,pp}$. The measured and calculated EDM currents are slightly shifted. To ionize the atoms and to create conditions for current to flow through the lubricant, the electric field has to exist for a short time [17]. Because at 40°C and 300 rpm, the current density $J_b = \hat{i}_b/A_{Hz} = 0.67\text{A}/0.84 \text{ mm}^2 \cong 0.81\text{A}/\text{mm}^2$ exceeds the limit of the safe operation of 0.8 A/mm² [5], the bearing life is affected. If the bearing temperature rises at 60°C, as example after two hours operation, the current density decreases at almost half ($J_b \sim i_{b,pp} \sim h_{min}$, $h_{min,60^\circ\text{C}} \cong h_{min,40^\circ\text{C}}/2$), in a safe operation area. The prediction shows that at low speed, the bearings can be quickly damaged at 40°C, but they can operate longer at 60°C.

The measurement setup has a strong influence on the EDM current. By eliminating the measurement setup, the EDM current is calculated (Fig. 2.4-11). The discharge time is given by:

$$t_d \cong 3 \cdot R_b \cdot (C_{RS} + C_{bDE} + C_{bNDE}) \cong 31 \text{ ns} \quad (6)$$

In the assumptions of Fig. 2.4-6, i.e. a discharge event at the DE bearing, more than half of the harmful electric energy is stored in the machine air gap and it is transmitted to the DE bearing during the arcing effect. A smaller part of the discharge energy is transferred from the capacitance of the opposite bearing to the bearing where the discharge occurs. The discharge current that flows through the shaft impedance, from one bearing to another, becomes the source of the radio frequency emissions, in the range of 50 MHz ... 100 MHz, at short distances around the motor. These frequencies are measurable with radio antennas [18].

D. Discharge Energy

For a maximum voltage of 8 V, at 300 rpm, 40°C and an equivalent bearing load of $F = 160$ N, an energy level of 41.9 nJ is calculated. According to [8], craters with a diameter less than 1.35 μm are predicted, but they do not necessarily indicate a bearing failure. These small craters could be flattened by the roller elements during the bearing operation.

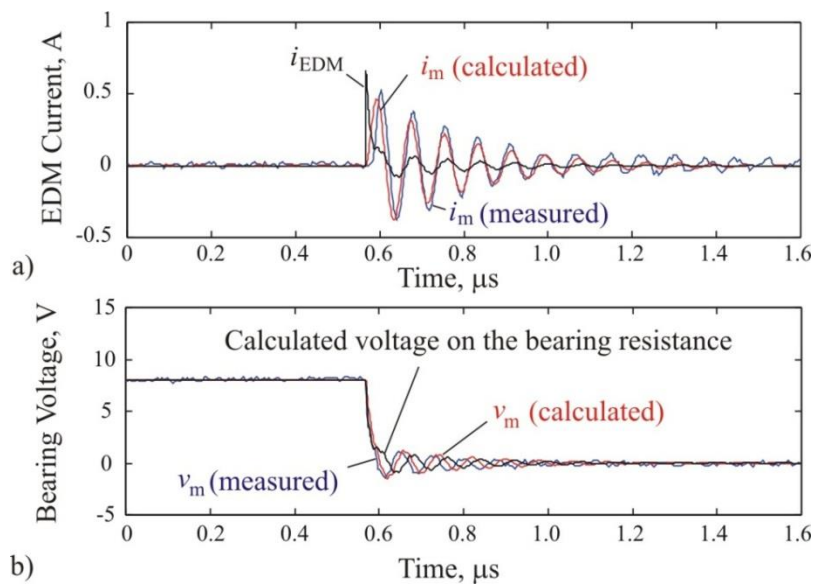


Figure 2.4-10 1.5 kW inverter-fed induction machine operating at 300 rpm, 40°C lubricant temperature and an equivalent bearing load of 160 N: a) - Measured and calculated bearing current, b) - Measured and calculated voltage across the bearing.

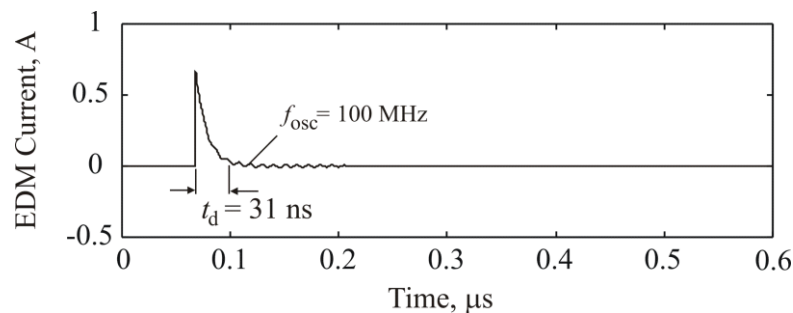


Figure 2.4-11 Calculated EDM current with the circuit of Fig. 2.5-8. The measurement setup was removed. Radio frequency emissions in the 100 MHz frequency range, are possible due to the shaft impedance and bearing capacitances working as a radio antenna [18].

2.5. Bearing impedance measurements

Usually, the bearing capacitance is measured together with the stator-to-rotor frame capacitance C_{RS} and the stator winding-to-rotor capacitance C_{WR} [11]. This method has been used to measure the bearing capacitances in the DFG FOR 575, Annual Report 2009. To avoid the major influences of the capacitances C_{RS} and C_{WR} on the measured bearing capacitance and, therefore, on the bearing impedance, a test machine with the removed stator yoke has been prepared for bearing impedance measurements with an RLC -meter, connected between the shaft (via a silver brush) and stator housing. According to Section 2.2, the bearing operation conditions were modified in a three machine test bench. Two lubricants G1 – High Impedance Grease and G4 – Low Impedance Grease were selected to measure the bearing impedance (Fig. 2.5-1). For both the tested lubricants, the effective bearing impedance and the equivalent bearing resistance have decreased with the frequency increasing. In the MHz range the equivalent bearing resistance is in order of tens of ohms. For the tested lubricant G1 the equivalent bearing capacitance was mainly constant with the frequency variation (Fig. 2.5-2b). For the other lubricant G4, the bearing capacitances has decreased with the frequency increasing. Thus, those simple measurements of the

bearing capacitances at low frequency may fail in the evaluation of the bearing capacitances for the entire frequency spectrum, i.e. 1 kHz ... 30 MHz.

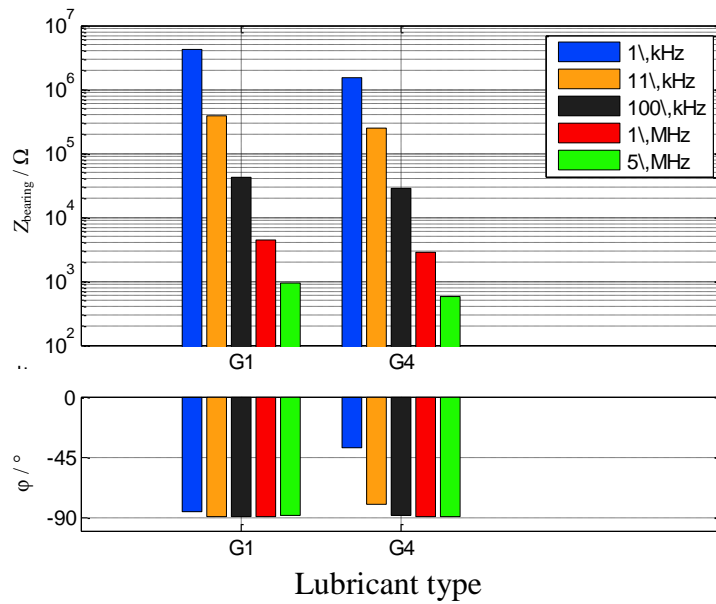


Figure 2.5-1 Measurements of lubricant impedance and phase with an *RLC*-meter at a speed of 1500 rpm, at an equivalent radial load of 650 N ($F_r \gg F_a$) and at 40°C bearing temperature.

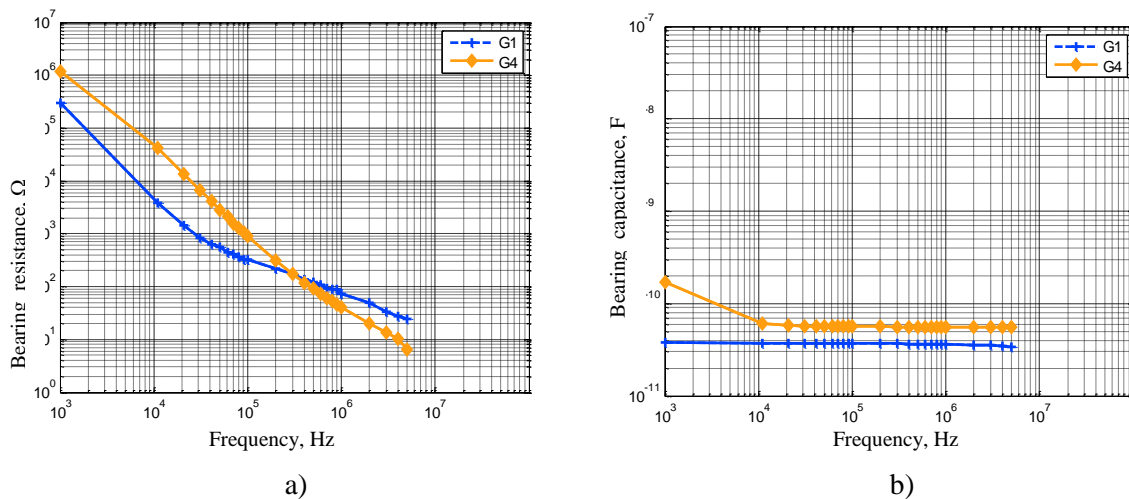


Figure 2.5-2 Measured bearing resistance R_b (a) and capacitance C_b (b) of Fig. 2.6-1, in the conditions of Fig. 2.5-1.

2.6. The bearing impedance model at steady state

At steady state, the electrical model of bearings consists of combinations of the inner and outer bearing capacitances, $C_{i,ball}$ and $C_{o,ball}$, and lubricant resistances $R_{i,ball}$ and $R_{o,ball}$ (Fig. 2.6-1). The equivalent impedance for a single ball is, therefore, defined [19]:

$$\underline{Z}_{ball} = \underline{Z}_{i,ball} + \underline{Z}_{o,ball} \tag{7}$$

$$\underline{Z}_{i,ball} = \frac{jX_{i,ball} \cdot R_{i,ball}}{R_{i,ball} + jX_{i,ball}} \tag{7a}$$

$$\underline{Z}_{o,ball} = \frac{jX_{o,ball} \cdot R_{o,ball}}{R_{o,ball} + jX_{o,ball}} \quad (7b)$$

which gives the equivalent resistance of one ball:

$$R_{ball} = \frac{X_{i,ball}^2 X_{o,ball}^2 \cdot (R_{i,ball} + R_{o,ball}) + R_{i,ball} R_{o,ball} \cdot (X_{o,ball}^2 R_{i,ball} + X_{i,ball}^2 R_{o,ball})}{(R_{i,ball} R_{o,ball} - X_{i,ball} X_{o,ball})^2 + (X_{o,ball} R_{i,ball} - X_{i,ball} R_{o,ball})^2} \quad (8)$$

and the equivalent capacitance of one ball, defined for each frequency f :

$$C_{ball} = \frac{1}{2\pi f \cdot X_{ball}} \quad (9)$$

where:

$$X_{ball} = \frac{R_{i,ball}^2 R_{o,ball}^2 \cdot (X_{i,ball} + X_{o,ball}) + X_{i,ball} X_{o,ball} \cdot (R_{o,ball}^2 X_{i,ball} + R_{i,ball}^2 X_{o,ball})}{(R_{i,ball} R_{o,ball} - X_{i,ball} X_{o,ball})^2 + (X_{o,ball} R_{i,ball} - X_{i,ball} R_{o,ball})^2} \quad (10)$$

The bearing capacitance is calculated for roller bearings and ball bearings, considering the number of roller elements from the loaded zone N_z as equally loaded [19]:

$$C_b = N_z \cdot C_{ball} \quad (11)$$

Similarly, the bearing resistance [19] is given as:

$$R_b = R_{ball} / N_z \quad (12)$$

For much larger radial loads than the axial loads, the number of roller elements from the loaded zone N_z is generally less than half of the total number of rolling elements in a bearing $N_z \leq N_b/2$ [19]. Thus, for the following calculation it is assumed that $N_z \cong N_b/2 \approx 4$. As a result, for the lubricant G1, the calculated bearing impedance matches well with the measured one (Fig. 2.6-2).

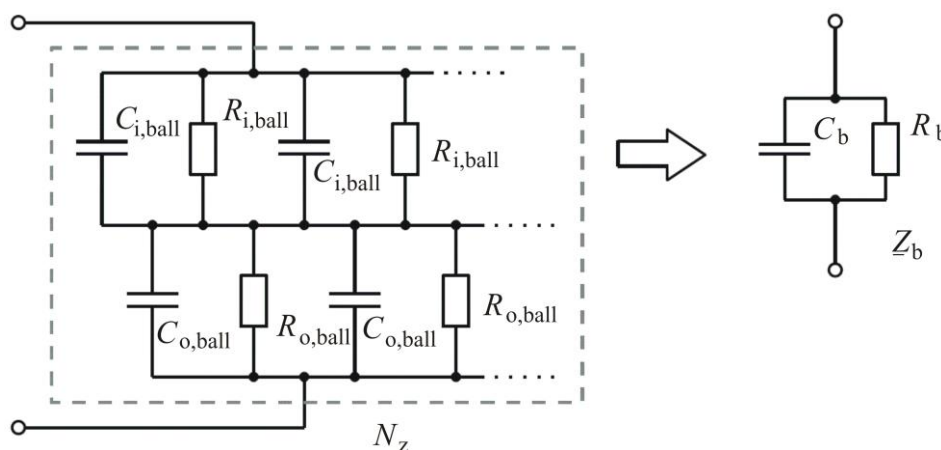


Figure 2.6-1 The bearing impedance model at steady state. The ball bearing resistances $R_{i,ball}$ and $R_{o,ball}$ and the ball bearing capacitances $C_{i,ball}$ and $C_{o,ball}$ are connected in series and parallel.

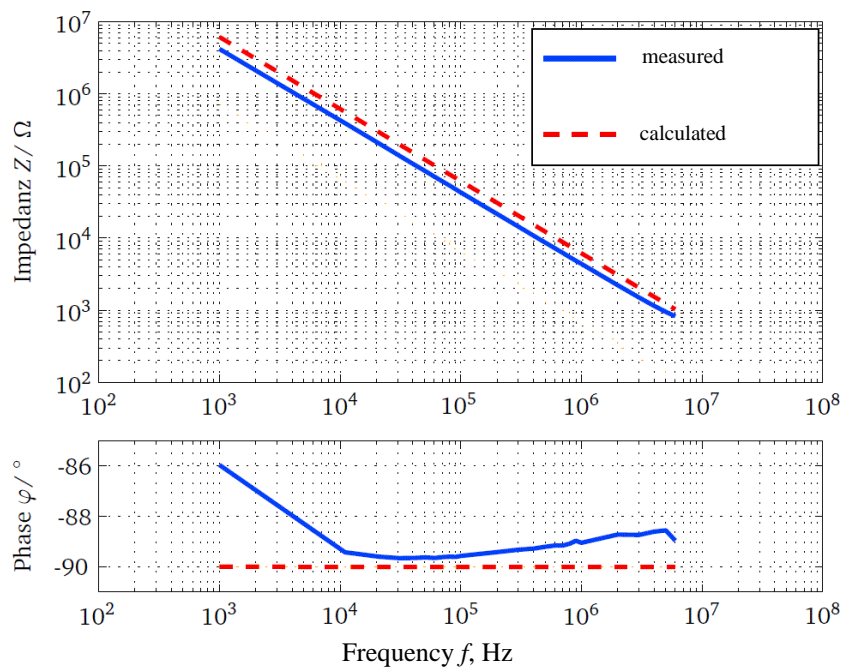


Figure 2.6-2 Measured and calculated bearing impedance Z_b and phase φ for the lubricant G1 in the conditions of Fig. 2.5-1. The bearing impedance (Fig. 2.6-1) is calculated as the equivalent bearing capacitance C_b of (11) in parallel to the bearing resistance R_b of (12). For the calculation N_z is assumed to be one. Taking N_z two balls into account, a good agreement between measurement and calculation exist.

2.7. Tests for detection of bearing failures caused by rotor-to-ground currents

When the rotor is grounded, important high frequency rotor-to-ground currents flow through the bearings of the inverter-fed AC machines [1]. With short time tests, the influence of the bearing operating parameters on the rotor-to-ground current can be analysed, if for example, the method of [1] is used, and in order to increase the line-to-ground voltage, capacitors are added between the motor terminals and ground (Fig. 2-7.1a) [1]. Three technical setups were tested for 500 h to find stable operating conditions: 1) -both the DE and the NDE are grounded (T1 = 500 h), 2) - the NDE is grounded (T2 = 500 h), and 3) - the DE is grounded (DFG FOR 575 -Annual Report 2010). The Test 3 showed stable operating conditions and constant rotor-to-ground currents during the 500 h test period (Fig. 2-7.1b). After T3a = 500 h, for different operating bearing conditions (Table 2.7-1 and 2.7-2), only the grey race was visible, and therefore, the test duration was increased at T3b = 1000 hours. A switching frequency of 10 kHz was imposed from the inverter and a bearing current density bigger than 3 A/mm^2 was imposed by increasing the line-to-ground voltage [1]. In this case, bearing damage by fluting was found.

Fig. 2.7-2 shows the fluting of the DE bearing of the 1.5 kW induction machine (Setting “9”, Table 2.7-1) after 1000 hours. The rotor-to-earth current measurements (Fig. 2.7-2a) show a stable current of 4 A (current density of 4.5 A/mm^2). The discharge activity was lower at the beginning of the test ($DA = 5000$ rotor-to-earth currents per second), and after 500 hours, it was stabilized at a constant discharge activity ($DA = 9500$ rotor-to-earth currents per second) (Fig. 2.7-2c). Fig. 2.7-3 shows the evaluation results for the DE bearing of the 11 kW induction machine (Setting “10”, Table 2.7-2). For this test, the fluting occurs only at the inner bearing race (Fig. 2.7-3b), while the grey race occurs at the outer bearing race (Fig. 2.7-3c). For this case, the rotor-to-earth current was not constant from the test beginning. It reached a stable value after 15 days, approximately 40% of the test time period. The discharge activity was stabilized at $DA = 5000$ rotor-to-earth currents per second.

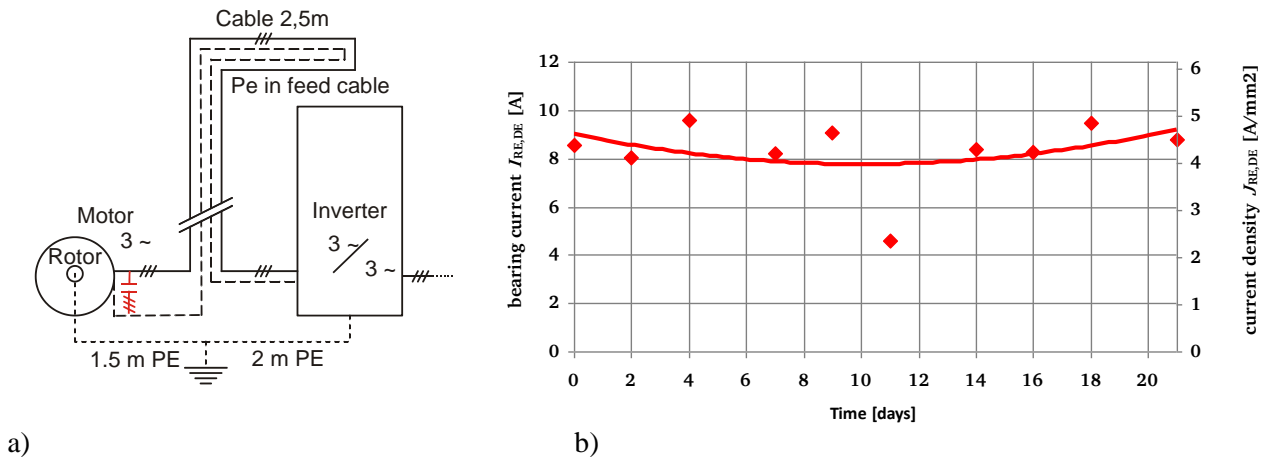


Figure 2.7-1

- a) Technical setup, 1.5 kW and 11 kW induction machines, for bearing current damage assessment
- b) Current distribution for 500 h for 1.5 kW induction machine; only the DE bearing is grounded; 270 N radial and 150 N axial load, 58°C bearing temperature and 450 rpm

Table 2.7-1 Rotor-to-earth current tests performed for the 1.5 kW induction machines at different operating parameters¹

- 3 x 1.5 kW induction machines
- 3 bearings for each cycle of tests (T3)
- 16 different settings and 6 bearings per setting, resulting in 96 tests
- 3 bearings can be tested in 2 month (T3)

	Setting 1	Setting 2	Setting 3	Setting 4	Setting 5	Setting 6	Setting 7	Setting 8
Speed	1500 rpm (H)	1500 rpm (H)	1500 rpm (H)	1500 rpm (H)	1500 rpm (H)	1500 rpm (H)	1500 rpm (H)	1500 rpm (H)
Axial Bearing Load	50 N (L)	150 N (H)	50 N (L)	150 N (H)	50 N (L)	150 N (H)	50 N (L)	150 N (H)
Radial Bearing Load	63 N (L)	63 N (L)	63 N (L)	63 N (L)	270 N (H)	270 N (H)	270 N (H)	270 N (H)
Bearing Temperature	58 °C (L)	57 °C (L)	100 °C (H)	100 °C (H)	55 °C (L)	54 °C (L)	100 °C (H)	100 °C (H)
Number of Bearings Measured	T1: 2 T2: 6 T3b: 3	T3b: 3	T1: 2 T3b: 3	T1: 2 T3b: 3	T3b: 3	T3b: 3	T3b: 3	

	Setting 9	Setting 10	Setting 11	Setting 12	Setting 13	Setting 14	Setting 15	Setting 16
Speed	450 rpm (L)	450 rpm (L)	450 rpm (L)	450 rpm (L)	450 rpm (L)	450 rpm (L)	450 rpm (L)	450 rpm (L)
Axial Bearing Load	50 N (L)	150 N (H)	50 N (L)	150 N (H)	50 N (L)	150 N (H)	50 N (L)	150 N (H)
Radial Bearing Load	63 N (L)	63 N (L)	63 N (L)	63 N (L)	270 N (H)	270 N (H)	270 N (H)	270 N (H)
Bearing Temperature	50 °C (L)	53 °C (L)	100 °C (H)	100 °C (H)	51 °C (L)	52 °C (L)	100 °C (H)	100 °C (H)
Number of bearings Measured	T2: 6 T3b: 3	T3b: 3			T2: 6	T3a: 3		

¹ green = test complete, blank = no tests done yet; T1 = 500 h test duration with the earth connection setup 1, T2 = 500 h test duration with the earth connection setup 2; T3a = 500 h test duration with the earth connection setup 3; T3b = 1000 h test duration with the earth connection setup 3.

Table 2.7-2 Rotor-to-earth current tests performed for the 11 kW induction machines at different operating parameters²

- 3 x 11 kW induction machines
- 3 bearings for each cycle of tests (T3)
- 16 different settings and 6 bearings per setting, resulting in 96 tests
- a single test at the beginning increase (the sum of tests has increased from 96 to 112)
- 3 bearings can be tested in 2 month (T3)
- 10 month test time – 60 bearings each year

	Setting 1	Setting 2	Setting 3	Setting 4	Setting 5	Setting 6	Setting 7	Setting 8
Speed	1500 rpm (H)	1500 rpm (H)	1500 rpm (H)	1500 rpm (H)	1500 rpm (H)	1500 rpm (H)	1500 rpm (H)	1500 rpm (H)
Axial Bearing Load	240 N (L)	720 N (H)	240 N (L)	720 N (H)	240 N (L)	720 N (H)	240 N (L)	720 N (H)
Radial Bearing Load	325 N (L)	325 N (L)	325 N (L)	325 N (L)	995N (H)	995N (H)	995N (H)	995N (H)
Bearing Temperature	62°C (L)	59°C (L)	100°C (H)	100 °C (H)	ca 60°C (L)	ca 60°C (L)	100°C (H)	100 °C (H)
Number of bearings Measured	T1: 6 T3b: 3	T3b: 3	T3b: 3	T3b: 3				

	Setting 9	Setting 10	Setting 11	Setting 12	Setting 13	Setting 14	Setting 15	Setting 16
Speed	450 rpm (L)	450 rpm (L)	450 rpm (L)	450 rpm (L)	450 rpm (L)	450 rpm (L)	450 rpm (L)	450 rpm (L)
Axial Bearing Load	240 N (L)	720 N (H)	240 N (L)	720 N (H)	240 N (L)	720 N (H)	240 N (L)	720 N (H)
Radial Bearing Load	325 N (L)	325 N (L)	325 N (L)	325 N (L)	995N (H)	995N (H)	995N (H)	995N (H)
Bearing Temperature	62°C (L)	59°C (L)	100°C (H)	100 °C (H)	ca 60°C (L)	ca 60°C (L)	100°C (H)	100 °C (H)
Number of Bearings Measured	T2: 6 T3b: 3	T2: 6 T3b: 3					T3a: 3	

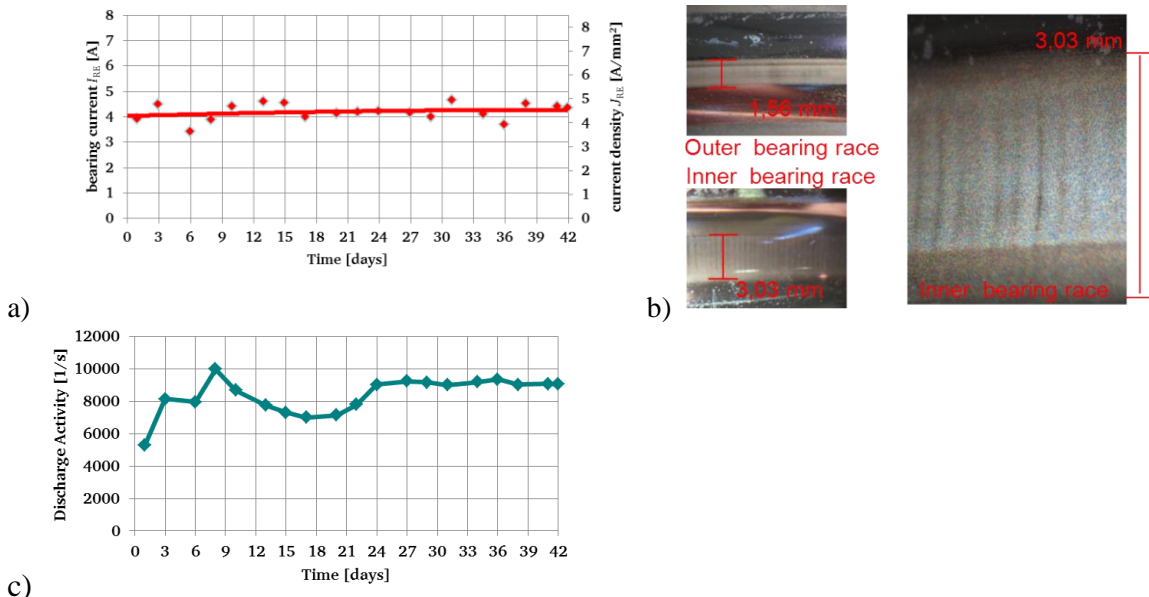


Figure 2.7-2 1000 h DE bearing test with the 1.5 kW induction machines of Setting “9“, Table 2.4-1: Current distribution for 1000 h (a), Photos of the ball bearing race after 1000 h (b), Discharge activity (c).

² green = test complete, blank = no tests done yet; T1 = 500 h test duration with the earth connection setup 1, T2 = 500 h test duration with the earth connection setup 2; T3a = 500 h test duration with the earth connection setup 3; T3b = 1000 h test duration with the earth connection setup 3

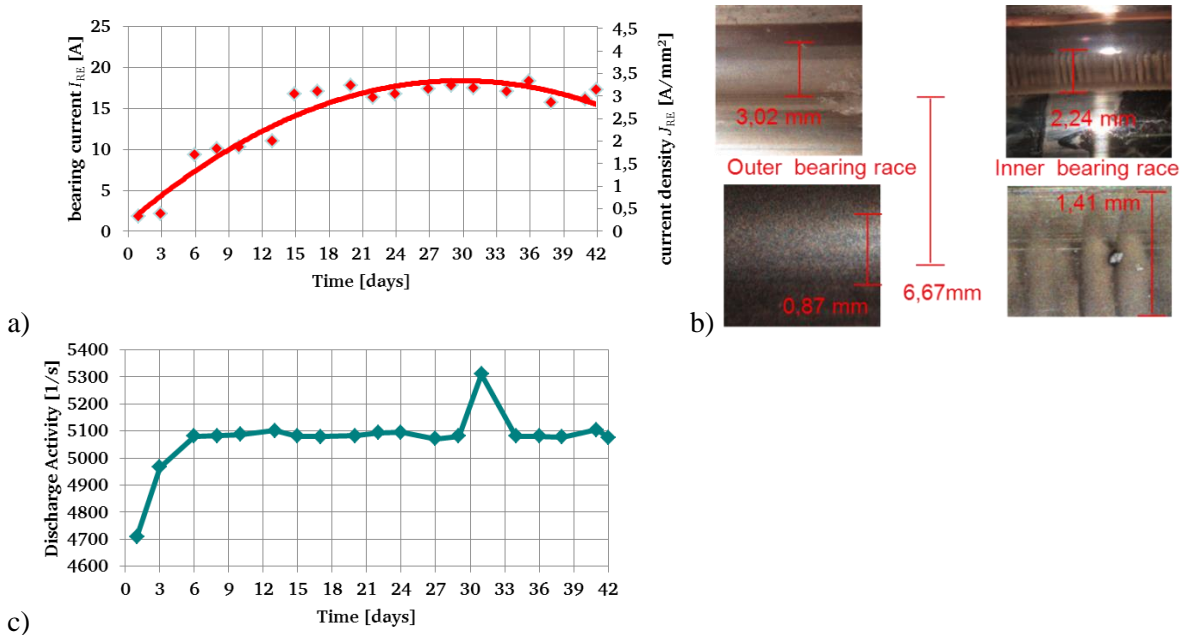


Figure 2.7-3 1000 h DE bearing test with the 11 kW induction machine of “Setting 10”, Table 2.4-2: Current distribution for 1000 h (a), Photos of the ball bearing race bearing (b), Discharge activity (c).

One of the 11 kW machines (Setting “10”, Table 2.7-2) produced big noises, after already 300 hours, and it was stopped. The dissembling of the machine showed broken balls (Fig. 2.7-4a). The bearings were changed and the machine was driven for the remained time of 700 h of the total time of 1000 h. The analyses of the bearing showed grey race (Fig. 2.7-4b).

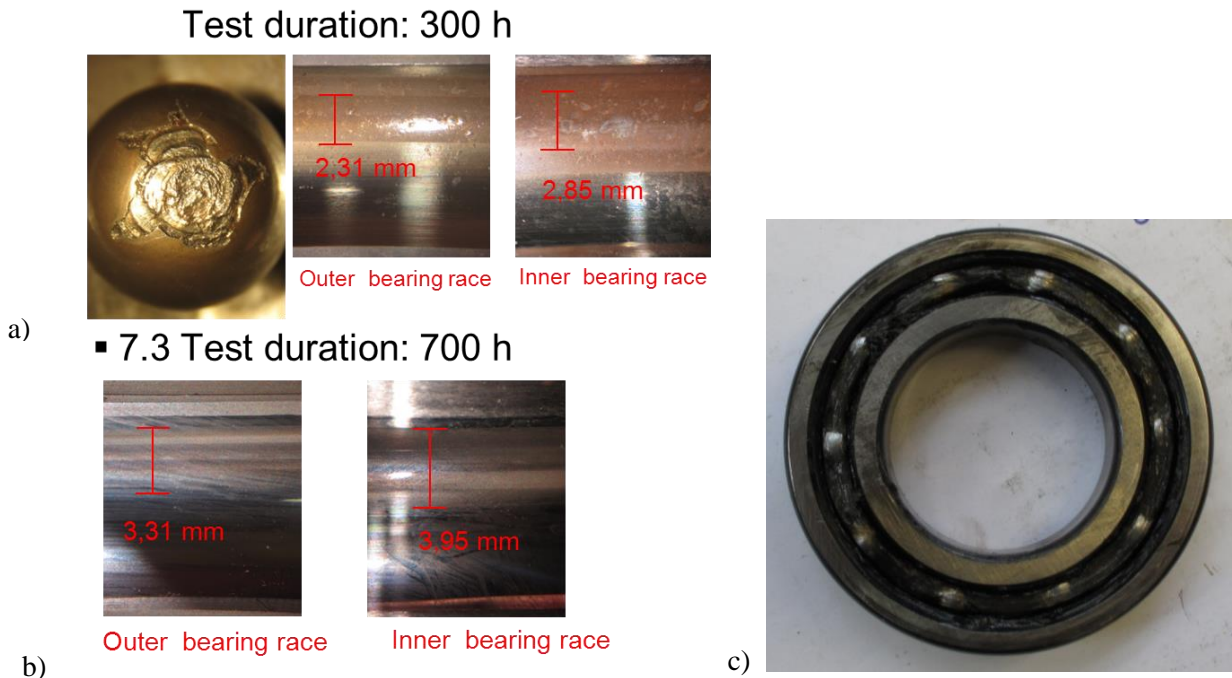


Figure 2.7-4 Bearing evaluation for the 11 kW induction machine (“Setting 10”, Table 2.7-2): a) after the ball failure (300 h test), b) after bearing replacing (700 h test), c) the grease color after rotor-to-ground current tests.

Because of the rotor-to-ground currents, the grease properties are changed dramatically (Fig. 2.7-4c), the lubricant colour changed from the light brown to a dark black). Thus, not only the fluting may occur in the bearings of the inverter-fed AC machines, but also mechanical problems may occur.

2.8. Conclusions

The extensive measurements performed here have shown that for the PWM controlled low-voltage 4-pole squirrel-cage induction machines, the shaft speed, the bearing load and the bearing temperature significantly affect the peak-to-peak values of the bearing currents and their rate of occurrence. By changing the ratio radial/axial bearing load, the peak-to-peak values of the EDM current are reduced and a stable grey surface may occur at the bearing race. For a longer life the bearings have to operate under load.

The main indicators of the bearing failures: the apparent bearing current density and the discharge energy were calculated and compared with the degree of degradation of bearings. For the bearings of a 1.5 kW inverter-fed AC machine, the apparent current density of 0.8 A/mm^2 indicates correctly the bearing failure. No bearing damages were found for a current density less than 0.3 A/mm^2 . The discharge activity and the energy value have to be considered when the current density value is between $0.3 \dots 0.8 \text{ A/mm}^2$. If the discharge activity cannot be counted, the bearing temperature and the radial and axial bearing load have to be considered for a rough prediction of the bearing failures. For all the tested bearings, a bearing temperature of 100°C and a much larger radial load than the axial load has significantly reduced the degree of bearing degradation. A current density lower than 0.8 A/mm^2 , a bearing temperature of 100°C and a much bigger radial bearing load than the axial load can keep the bearings safe.

The bearing impedance model has been verified. For standard mineral lubricant oils the measured bearing impedance fits with the calculated one. It generally decreases with the frequency increasing.

From the tests it is visible that test duration of 500 h is not sufficient to induce fluting. It was possible during the project to finish all the tests for the EDM current analyses. The rotor-to-ground current tests were not finished yet, because it was first necessary to find stable test conditions. After they were found the test had started. At the moment the evaluated results are not sufficient to give a clear tendency.

Closed to the end of the DFG-FOR 575 it was possible to be a part of a project managed by the organization FVA. This project continues the research on EDM and Rotor-to-Earth bearing currents, where the results of this report are one manger input of the project of the FVA.

References

- [1] A. Muetze, *Bearing Currents in Inverter-Fed AC Motors*, Ph.D. thesis, Darmstadt Univ. of Technology, Shaker Verlag, Aachen 2004.
- [2] A. Muetze, A. Binder, H. Voegel, J. Hering, "What can bearing bears?“, IEEE Industry Application’s Magazine, pp. 57-64, November/ December, 2006.
- [3] T. A. Harris, M. N. Kotzalas, *Advanced Concepts of Bearing Technology*, CRC Press, New York, 2006.
- [4] O. Magdun, Y. Gemeinder, A. Binder, "Investigation of Influence of Bearing Load and Bearing Temperature on EDM Bearing Currents“, Proceedings of ECCE’10, pp.2733-2738, Atlanta, USA, September 12-16, 2010.
- [5] D. Busse, J.Erdman, R.J. Kerkman, D. Schlegel, G.Skibinski, "The Effects of PWM Voltage Source Inverters on the Mechanical Performance on Rolling Bearings“, IEEE Transactions on Industry Applications, vol. 33, no. 2, pp. 567-576, March/April 1997.
- [6] D. Busse, J.Erdman, R.J. Kerkman, D. Schlegel, G.Skibinski, "Bearing currents and Their Relationship to PWM Drives“, IEEE Transactions on Power Electronics, vol. 12, no. 2, pp. 243-252, March 1997.

- [7] H.Prashad, “Appearance of craters on track surface of rolling element bearings by spark erosion”, *Tribology International*, vol.34, no.1, pp.39-47, January 2001.
- [8] H. Tischmacher, S. Gattermann, “Bearing Currents in Converter Operation”, XIX Conference on Electrical Machines - ICEM’10, CD-ROM, 8 pages, Rome, Italy, September 6-8, 2010.
- [9] A. Muetze, A. Binder, ”Calculation of Motor Capacitances for Prediction of the Voltage Across the Bearings in Machines of Inverter-Based Drive Systems”, *IEEE Transactions on Industry Applications*, vol. 43, no. 3, pp. 665-672, May /June 2007.
- [10] P. Maeki-Ontto, J. Luomi, “Design of Converter-Fed Induction Motors to Reduce Bearing Currents”, Proceedings of ICEM’04, CD-ROM, 6 pages, Cracow, Poland, 2004
- [11] O. Magdun, Y. Gemeinder, A. Binder, “Prevention of harmful EDM currents in inverter-fed AC machines by use of electrostatic shields in the stator winding overhang”, Proceedings of IECON’10, pp.962-967, Glendale, USA, November 7-10, 2010.
- [12] O. Magdun, Y. Gemeinder, A. Binder, K. Reis, „Calculation of Bearing and Common-Mode Voltages for the Prediction of Bearing Failures Caused by EDM Currents“, Proceedings of SDEMPED’11, pp.462-467, Bologna, Italy, September 5-8, 2011.
- [13] O. Magdun, A. Binder, Y. Gemeinder, “Representation of Iron Core and Dielectric Losses for Calculation of Common Mode Stator Ground Currents in Inverter-Fed AC Machines”, Proceedings of OPTIM’10, pp.371-376, Brasov, Romania, May 20-22, 2010.
- [14] A. Harnoy, *Bearing Design in Machinery: Engineering Tribology and Lubrication*, CRC Press, New York, 2002.
- [15] H. Tischmacher, S. Gattermann, M. Kriese, E. Wittek, “Bearing Wear Caused by Converter-Induced Bearing Currents”, Proceedings of IECON’10, pp.784-791, Glendale, USA, November 7-10, 2010
- [16] G. Preisinger, *Cause and effect of bearing currents in frequency converter driven electrical motors-investigations of electrical properties of rolling bearings*, Ph-D Thesis, Vienna University of Technology, 2002.
- [17] A. Jagenbrein, *Investigations of bearing failures due to electric current passage*, Ph-D Thesis, Vienna University of Technology, 2005.
- [18] A. Muetze, J. Tamminem, J. Ahola, „Influence of Motor Operating Parameters on Discharge Bearing Current Activity“, *IEEE Transactions on Industry Applications*, vol. 47, no. 4, pp. 1767-1777, July/August 2011.
- [19] H. Prashad, *Tribology in Electrical Enviroments*, Elsevier Ltd., 2006.

6.2. Subproject 2: Extended Transmission Line Models for Inverter-fed Electrical Drives using Multi-rate Time Integration

Dipl.-Ing. Hai Van Jorks

PD Dr.rer.nat. habil. Erion Gjonaj

Institut für Theorie Elektromagnetischer Felder, TU Darmstadt

E-Mail: jorks@temf.tu-darmstadt.de

1. Summary

The aim of the project is the numerical investigation of high frequency parasitic effects in inverter controlled induction machines. This is performed by first extracting a transmission line model of the machine and then incorporating this model into transient network simulations including the switching network. The main achievements of this work are:

1. A parallel high order 3D FE code which is well suited for the simulation of eddy currents in laminated cores was developed.
2. The validity of equivalent material (homogenization) models as used in 2D and 3D simulation tools was thoroughly investigated for frequencies up to 1MHz.
3. A direct parameter extraction procedure from FE discretization matrices was implemented.
4. A general matrix projection approach for the calculation of the common mode impedance from impedance matrices for arbitrary winding schemes and given symmetries is introduced.

The main finding is that equivalent material models for laminated cores as commonly proposed in the literature are not appropriate for eddy current simulations in the interesting high frequency range. Full scale 3D simulations including the lamination geometry are necessary for the investigation of parasitic machine currents at these frequencies. Also, we show that when properly implemented the 3D simulation approach is indeed viable and that it can be successfully applied in modeling and simulation with realistic motor geometries.

2. Work schedule and accomplished tasks

Nr	Duration (months)	Content	Status
1	2	Porting of FEMM to 64-bit	Completed
2	4	Implementation of parallelization in FEMM	Completed
3	2	Extraction of transmission line parameters for the stator windings by 2D FE analysis	Completed
4	6	Application of 2-1/2-D homogenization formulations for core laminations. Investigation of the validity of these approaches at higher frequencies	Completed
5	0	Extraction of effective electromagnetic material parameters for the stator block using a homogenization approach in 3D	Not considered due to the resulting low accuracy of homogenization approaches at higher frequencies
6	10	Implementation of a specialized parallel finite element code for eddy current simulations in 3D geometry	Completed
7	6	Extraction of transmission line impedance parameters for the stator windings by 3D FE analysis	Completed for test problems; ongoing for the full 240 kW motor model
8	6	Investigation of stator end-effects by full-geometry 3D simulations	Intended
9	4	Transient simulations of the coupled transmission line cable and machine models using multi-rate time integration	Intended

3. Introduction

When a motor is fed by an inverter switched power supply, the vector sum of the three phases does not cancel. This additional voltage component can be considered as a common mode voltage source which alternates with the switching frequency. The stray capacitances in the machine provide a low impedance path to the ground at higher frequencies. The resulting common mode ground voltage evokes circulating currents which may damage the bearings of the machine [9]. The calculation of the common mode machine impedance is, thus, crucial for the investigation of the bearing and EDM current phenomena in inverter-fed induction machines. Due to the very short rise times of the inverter pulses, however, a broad range of frequencies reaching up to a few MHz needs to be considered in the investigation [10].

The transient behavior of machine currents can be described by a Transmission Line Model (TLM) consisting of a set of frequency dependent impedance parameters, which can be extracted from eddy current simulations. For this purpose, 2D as well as 3D Finite Element (FE) analysis can be applied. Hereby, the motor geometry is usually divided into three parts. Front and rear end of the device form the so called end-windings. In order to investigate these parts of the machine, several analytical [3,12] as well as numerical techniques [1] have been proposed. In this project, however, end-windings have not been considered so far although they will constitute one of the main research topics of our future work. The laminated middle part of the motor is the most important part of the device, as it accounts for the largest contribution in the coupling impedances. It represents a geometrically periodic structure with periodicity given by the thickness of the lamination sheets. A cross-sectional view of a 240 kW induction motor which is considered in more detail in the following is shown in Fig. 7b. Obviously, the main difficulty in the numerical analysis of this part of the machine is the modeling of the eddy currents in the laminated cores. Due to the presence of laminations, the induced current flow in the stator and rotor blocks is intrinsically three dimensional. On the other hand, the complex motor geometry as well as the small skin depth in the iron at higher frequencies makes the application of conventional 3D eddy current simulation tools for realistic motor geometries virtually impossible.

In order to cope with this difficulty, several solutions have been proposed. A common approach is based on 2D FE simulations of the motor cross-section including a frequency dependent permeability (or conductivity) for the iron parts which takes into account the current flow in the lamination [7]. Another, technique employs an anisotropic but otherwise homogeneous conductivity tensor which can be introduced in fully 3D FE eddy current simulations. The validity of these approaches in the interesting higher frequency range is, however, not obvious. Also in the literature no detailed studies on the accuracy of these models at high frequencies are reported. This is why the investigation of these most commonly used homogenization approaches constituted one of the main tasks of the project. For this purpose, we have developed a very efficient 3D simulation tool which enables explicit modeling of eddy currents even for complex motor geometries. Thus, simulation results using homogeneous and 3D-laminated motor models can be directly compared. The final goal of the project, however, is the extraction of a higher frequency equivalent TLM and, in particular, the computation of the common mode input impedance for an existing 240 kW induction motor taking into account the full eddy current distribution in the laminated rotor and stator cores.

4. Eddy current modelling in laminated cores

4.1. Equivalent permeability model

Eddy currents in laminations cannot be taken into account explicitly in 2D FE simulations since the stacking direction is perpendicular to the simulation plane. However, the impact of eddy currents in the flux distribution can be partially included by a simple one-dimensional analytical model [11]. This model is incorporated, e.g., in the FEMM code [7] by means of an equivalent iron permeability given by

$$\mu_{eq} = \frac{\mu_0 \mu_r \sinh \alpha b}{\alpha b \cosh \alpha b}, \quad \alpha = \frac{(1+j)}{\delta} \quad (1)$$

with $2b$ being the lamination's thickness. In the following, the iron core is assumed to be linear with relative permeability $\mu_r = 1000$ and electric conductivity $\sigma = 2.63 \text{ MS/m}$. For these parameters, the penetration depth of the eddy currents, $\delta = 1/\sqrt{\pi f \sigma \mu}$, in the core becomes comparable to the lamination thickness (0.65 mm), for frequencies above 200 Hz. This model is exact if the lamination sheets extend to infinity and the applied magnetic field strength is constant

all over the sheet. This is, clearly, not the case on the cross-section of a realistic induction motor. The electric losses and magnetic energy at different frequencies for a simple one conductor case resulting from the application of this simulation model are shown in the comparative study shown in Fig. 2 and 3.

4.2. Anisotropic conductivity approach

In conventional 3D FE motor simulations, the individual laminations cannot be resolved by the mesh. Resolving the small skin depth at higher frequencies and the thin oxide layer ($\approx 5 \mu\text{m}$) separating the iron sheets would lead to an enormous number of elements, which is far beyond today's computing capacity. A simplification which is often employed consists in assuming an anisotropic conductivity tensor in the bulk iron material with zero conductivity in the direction perpendicular to the lamination as [6,8]:

$$[\sigma] = \begin{bmatrix} \sigma_x & & \\ & \sigma_y & \\ & & \sigma_z \end{bmatrix} \rightarrow \begin{bmatrix} F\sigma_{Fe} & & \\ & F\sigma_{Fe} & \\ & & 0 \end{bmatrix} \quad (2)$$

where F is the stacking factor and σ_{Fe} is the conductivity of the iron sheet. This approach is quite accurate at low frequencies. The investigations discussed in Sec. 4.3 indicate an error of less than 4% when the model is applied at 50 Hz. This certainly justifies the application of this model in a number of commercial simulation tools. Nevertheless, as soon as the skin effect becomes significant, this simple homogenization technique becomes very inaccurate.

4.3. Full scale 3D FE simulations using prismatic elements

When interested in the middle part of the motor, it is possible to perform 3D simulations with full geometrical resolution of the lamination stack by taking advantage of the periodicity of the lamination structure. In this case, it is sufficient to include in the longitudinal direction of the computational model only half of a lamination sheet and half of the oxide layer, respectively (see Fig. 1). On the top and bottom faces, periodic boundary conditions can be imposed. Furthermore, given the geometry of the lamination stack, the model may be discretized by prismatic elements, thus, reducing the number of degrees of freedom needed in the computation.

Based on these ideas, a new 3D eddy current simulation tool was developed in the framework of this project [14, 15]. The code makes use of high order hierarchic basis functions on prismatic elements which allows for extremely accurate computations even on coarse meshes. This high accuracy is necessary, in particular, in the high frequency range where the skin depth is underresolved by the computational mesh. In order to be able to simulate complicated motor geometries, the code allows for large scale parallel computations on high performance computer clusters. Thus, the new simulation framework allows for efficient calculations of the actual eddy current distribution in the iron without any further assumption even at high frequencies. This enables, in particular, a thorough numerical investigation of the accuracy of the 2D and 3D homogenization approaches described in Section 4.1 and 4.2.

5. Validation studies

5.1. Single conductor test case

For validation purposes, the simple geometry shown in Fig. 1 is considered. It consists of a single rectangular copper conductor, which is embedded in a piece of laminated iron core with dimensions $10 \times 10 \times 0.655 \text{ mm}^3$. The iron sheet is covered on the top side by a thin oxide layer. The model geometry is only 0.3275 mm thick in the z-direction, which corresponds to half of a

lamination sheet plus half of an oxide layer thickness. Due to symmetry only one eighth of the geometry needs to be considered in the simulations. In the 2D simulation model, the lamination in the z-direction was considered using the equivalent permeability (1). Furthermore, 3D simulations were performed using, both, the anisotropic conductivity (1) as well as a full geometry model where the lamination sheets are discretized by high order prismatic elements. Figure 1 shows exemplarily the computational mesh used. For visibility, the geometrical dimensions are scaled by a factor 10 in the z-direction.

Figure 2 shows the calculated overall electric losses (P_{el}) and the stored magnetic energy (W_{mag}) for all three simulation approaches in the frequency range 10 Hz...1 MHz. Obviously, the 3D anisotropic conductivity model is the least accurate approach when compared with the full geometry simulations. In this case, large deviations in the electric losses are observed already at low frequencies. On the contrary, 2D simulations using the equivalent permeability model agree well with the reference in the low and medium frequency range. At 1 kHz the simulations show a difference of less than 7% for the electric losses and 1% for the magnetic energy, respectively. However, as the frequency increases the deviations become larger. As shown in Fig. 3, the differences between 2D and 3D results at 1 MHz amount to 9% for P_{el} and to 18% for W_{mag} , respectively. These observations provide a first indication on the necessity for full geometry 3D eddy current simulations in the investigation of higher frequency parasitic machine currents.

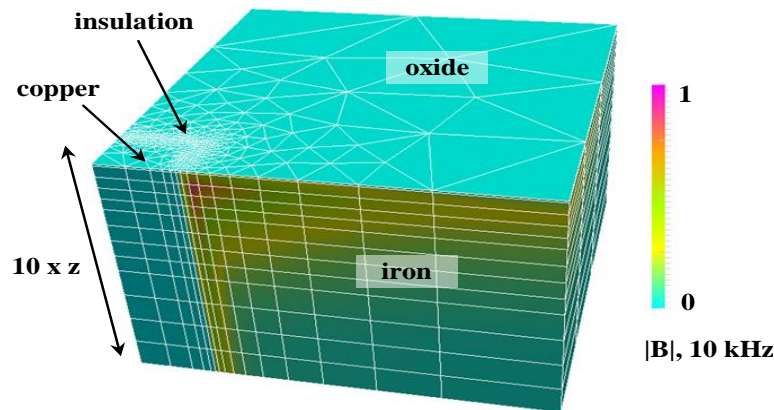


Figure 1 Simulation mesh and magnitude of the magnetic flux density (a.u.) resulting from a 3D simulation at 10 kHz. For better visibility, the model is scaled by a factor 10 in the z-direction.

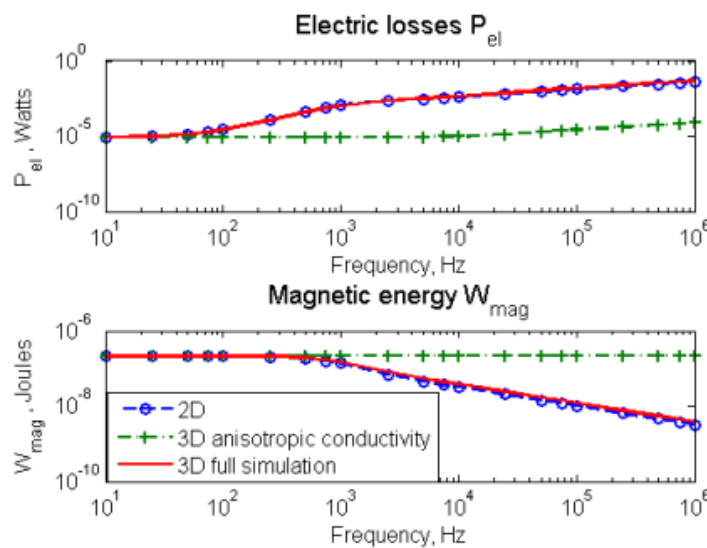


Figure 2 Total electric losses (top) and stored magnetic energy (bottom) obtained by numerical simulations using different approaches (2D, 3D homogenized and 3D full geometry).

5.2. Numerical accuracy

In the following, the numerical efficiency and accuracy of the 3D simulation approach described in Section 4.3 is investigated. This is done by means of a numerical convergence study for the single conductor case where a set of meshes with different resolutions as well as with different approximation orders is applied. Figure 3 shows that employing higher order basis functions improves accuracy significantly even for coarse meshes. This allows for reliable results, especially at high frequencies, where the skin depth is difficult to be resolved by the mesh. Full numerical convergence is obtained in the single conductor test case by using an extremely coarse mesh (with only 7,000 elements) and either quadratic or cubic FE basis functions. Also in the figure, the relative deviations between the 2D equivalent permeability model and the full geometry 3D eddy current simulations are shown.

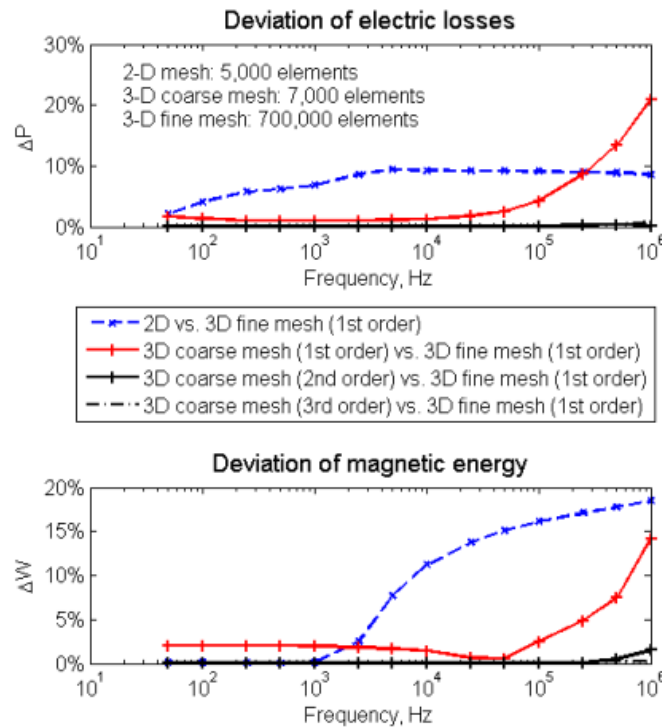


Figure 3 Numerical convergence of 3D eddy current simulations. Relative error of the computed electric loss and magnetic energy for different mesh resolutions and approximation orders.

Table 1 summarizes the computational parameters used in the simulations. As seen in the table, apart from providing more accurate results, the high order simulation approach does also reduce simulation times. A 2nd order computation on a coarse mesh is ~4 times faster than a fine mesh 1st order simulation for the same accuracy. The tuning of simulation parameters for optimal efficiency, however, depends also on the number of parallel computing nodes involved in the simulation. The 3rd order computation on a coarse mesh using 60 nodes appears less efficient than the 2nd order setup. This is due to well known the deterioration of the parallel speed-up in the computations when the numbers of parallel computing processors becomes too large.

Table 1 Computational parameters and CPU times for a full frequency sweep in the range 10 Hz...1MHz.

Simulation setup	Mesh elements	Approximation order	CPU time (hh:mm:ss)	No. of parallel computing nodes
2D	5,000	1	00:02:00	1
3D fine	700,000	1	02:08:33	30

3D coarse	7,000	1	00:02:59	10
3D coarse	7,000	2	00:28:24	24
3D coarse	7,000	3	01:06:05	60

5.3. 3D lamination effects on winding impedances

In order to investigate the influence of the lamination stack on the winding impedances, a simple two conductor network is considered. The cross-section of the model is depicted in Fig. 4. The two conductors are assumed to be connected so that

$$\underline{u}_1(l) = \underline{u}_2(l), \quad \underline{i}_1(l) = -\underline{i}_2(l), \quad (3)$$

where $\underline{u}_1(l), \underline{u}_2(l), \underline{i}_1(l), \underline{i}_2(l)$ are voltages and currents of line 1 and 2, respectively, at the rear end of the winding. The common mode voltage is applied to conductor 1 on the top side of the winding, whereas conductor 2 is left open ended, i.e.

$$\underline{u}_1(0) = U_{com}, \quad \underline{i}_2(0) = 0. \quad (4)$$

The current $\underline{i}_1(0)$ is calculated by solving telegrapher's equations taking into account the winding scheme (3-4). The common mode impedance is then derived as $\underline{Z}_{com} = U_{com}/\underline{i}_1(0)$.

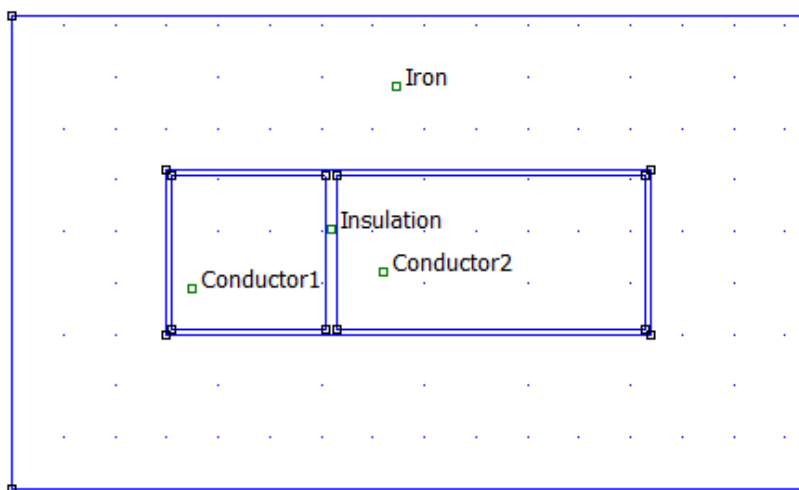


Figure 4 Top view of the two conductor winding and iron core. The insulation gap width as well as the lamination stack assembly is the same as in Section 5.1.

Figure 5 shows the relative deviation between some of the TLM network parameters extracted by 2D and 3D simulations, respectively. There, R_{11} denotes the self-resistance and L_{11} the self-inductance of conductor 1. For comparison purposes, the case of a massive iron core was considered in the simulations as well. In the latter case, 2D and 3D simulations should produce the same results since no eddy currents are induced in the horizontal plane. Indeed, the deviations between the computed parameters are extremely small, except for at higher frequencies (>100 kHz). This is due to the insufficient resolution of the mesh used in the simulations. In order to resolve the skin depth in this frequency range, both, 2D and 3D meshes must be refined drastically on the copper and iron surfaces.

The deviations in the laminated core case (see Fig. 5), however, are distinctly higher almost in the full frequency range. Already at 1 kHz, the deviation in the self-resistance and self-inductance amounts to more than 10%. The systematic errors in the parameters extracted by 2D simulations

are due to the use of the equivalent permeability lamination model (1). This behavior confirms again the previously obtained result that 2D simulation models employing homogenization approaches are generally not sufficiently accurate for the characterization of eddy currents in laminated cores in the interesting higher frequency range.

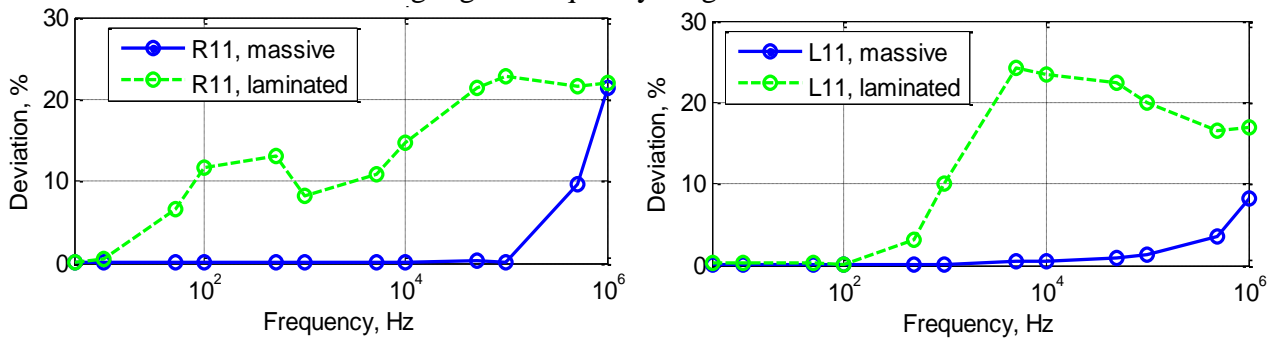


Figure 5 Relative deviations between the self-resistances (left) and self-inductances (right) of conductor 1 extracted by 2D and 3D simulations, respectively. The cases of a massive iron core (solid line) and that of a laminated core (dashed line) are considered.

For the calculation of the common mode impedance, a conductor length of $l = 0.35m$ was assumed. The capacitance matrix was obtained by electrostatic field simulations using $\epsilon_r = 2$ for the relative permittivity of the insulation. Figure 6 shows the computed common mode resistances and inductances, respectively, in the laminated case. Notable deviations are observed close to the first resonance frequency ($f \approx 100$ Hz). This is due to the shift in the resonance frequency caused by the application of the homogeneous core material model (1) in the 2D case. Also at higher frequencies beyond the resonance point a large discrepancy in the computed common mode input inductance is observed. Although not visible in the figure scaling, this difference amounts to ~22% at 100 kHz. Larger discrepancies are observed in the real part of Z_{com} whereas the imaginary parts extracted by 2D and 3D simulations show reasonable agreement.

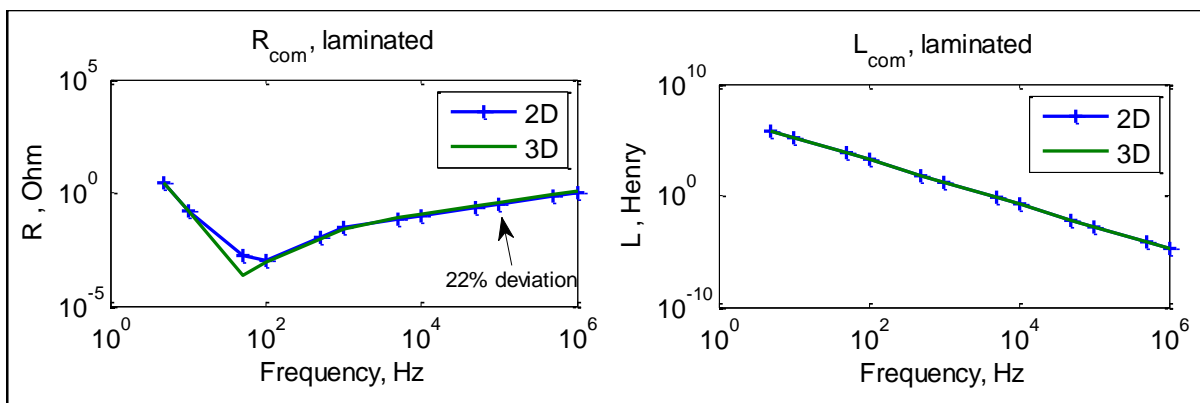


Figure 6 a) Common mode resistance (left) and inductance (right) for the two conductor model extracted by 2D and 3D simulations, respectively.

5.4. Influence of lamination on energy distribution in materials

To investigate the causes of inaccuracy in homogenized lamination models we compute the stored magnetic energy and electrical losses in each of the relevant materials of the conductor slot (iron and copper) separately by analytical calculations as well as by 2D and 3D simulations. For this purpose, the circular single conductor model shown in Fig. 7 (left) is considered. As seen in the figure, the equivalent permeability model is inaccurate for the electric losses in iron throughout the entire frequency range. Iron losses, however, are usually negligible at low frequencies compared

to the copper losses. Thus, at these frequencies the homogenization approach may be still applicable. In the higher frequency range, however, the deviations between the 2D homogenized model and reference solutions are noticeable for the electric losses in copper as well for the stored magnetic energies in both iron and copper.

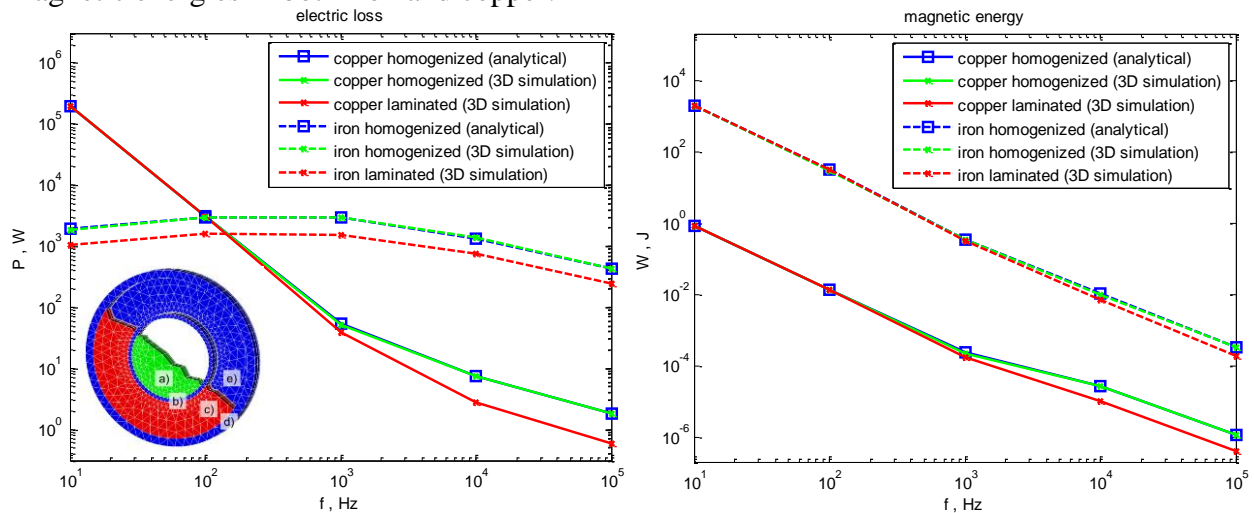


Figure 7 Electric losses (left) and stored magnetic energy (right) in the copper and iron parts of the model, respectively. The analytical solutions as well as results obtained by the 2D equivalent permeability approach and the fully 3D simulation (reference) are shown.

6. Simulation of a 240 kW motor

1.1. 2D eddy current simulations

A full cross-sectional view of the 240kW motor considered in the simulations is shown in Fig. 8b. The stator winding consists of 60 conductor slots with 12 conductors each where each conductor is split into two strands of rectangular cross-section (see Fig. 8a). Further 48 conductors are embedded in the rotor block. For the 2D eddy current simulations of the motor cross-section a 64bit version of FEMM [7] including the equivalent permeability model (1) was used.

The first investigation concerns the possibility of using a reduced size geometrical model by considering in the simulations a small number or possibly a single conductor slot. This approach was used in earlier publications (cf. [2,4,5]), where it was assumed that due to the small penetration depth in the iron core, the magnetic flux at high frequencies does not cross the slot boundary. Thus, the inductive coupling between conductors in neighboring slots was neglected. The simulation area was restricted to a single slot where the iron core was considered as the perfectly conducting solid boundary of the slot (see Fig. 8a).

Table 2 Comparison of selected mutual conductor impedances at 1MHz computed by single-slot and full cross-section simulations of the 240kW motor.

Impedance (Ω / m)	Slot	Single slot simulation	Full cross-section simulation
$Z_{1,1}$	1	$0.121 + 1.031i$	$14.332 + 18.830i$
$Z_{1,2}$	1	$0.046 + 0.717i$	$14.324 + 18.763i$
$Z_{1,13}$	2	-	$11.415 + 13.392i$
$Z_{1,121}$	10	-	$1.967 + 1.685i$

Our simulations, however, show that due to the flux penetration through the lamination the inductive coupling between the slots cannot be neglected. Even when reducing the full motor cross-section to a 90° (or 180°) section, inaccurate results for the coupling impedances are

obtained. This is demonstrated in Table 2 where the mutual impedances between selected conductors at 1MHz are computed by single-slot and full cross-section motor simulations, respectively. In the table, the self-impedance $Z_{1,1}$ of conductor 1 as well as the mutual impedances $Z_{1,2}$, $Z_{1,13}$ and $Z_{1,121}$ with conductors 2, 13 (on the neighboring slot) and 121 (conductor on distant slot) are given. In all cases, large discrepancies between the parameters obtained by the two approaches can be noticed. In full the cross-section simulations, it can be observed that the mutual impedance between distant slot conductors may be as large as 10% of its self-impedance. Thus, due to the lamination the entire cross-section of the motor must be taken into account even at very high frequencies. This poses a major challenge on the simulations (even in 2D) since the discretization of the full motor cross-section leads to extremely large computational models.

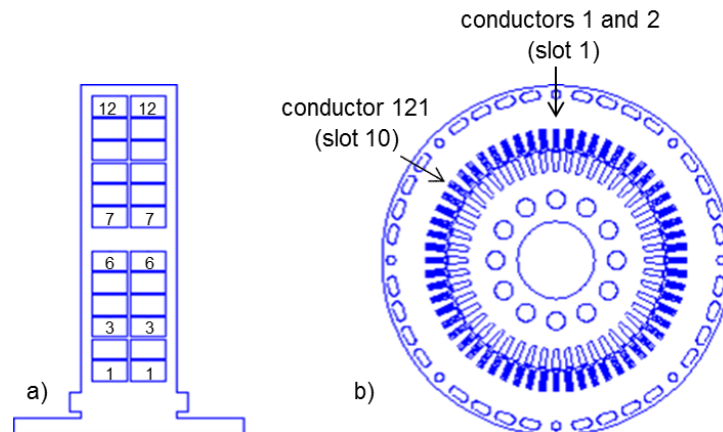


Figure 8 a) A single conductor slot including 24 rectangular cross-section conductor strands. b) Full cross-section of the 240kW motor including 60 stator slots as well as 48 conductors of the rotor winding.

1.2. 3D simulations

In these simulations the actual geometry of the 240 kW motor including the lamination layers is considered. An exemplary 3D mesh using prismatic elements is shown in Fig. 9. It consists of about 3 million elements. In the case of low order elements this figure corresponds to more than 5 million discrete degrees of freedom for the vector potential solution. The computation time for a parallel simulation using 60 computing nodes is about 1h for a full frequency sweep with 32 frequency points in the range 10 Hz...1MHz.

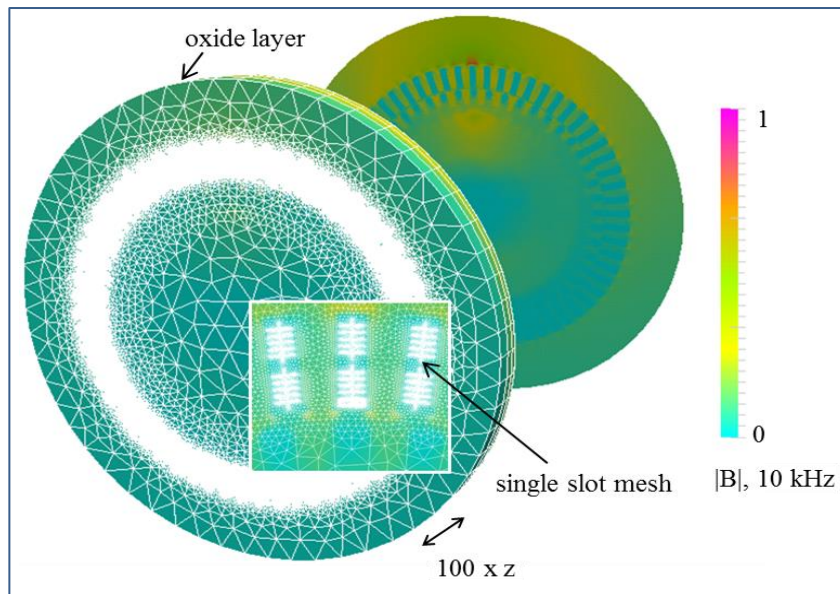


Figure 9 Simulation mesh and distribution of the magnetic flux density (a.u.) for the 3D model when a single conductor is excited at 10 kHz. For visibility, the model is scaled by a factor 100 in the z-direction.

The standard procedure for computing the inductance matrix consists in a large number of independent computations where each conductor is excited with an impressed current at each frequency. This approach is hardly applicable in the 3D case. Even though the simulation code with prismatic elements allows for large scale simulations of the entire motor cross-section, the computational time for extracting the full inductance matrix would become very large. For this reason, a parameter extraction procedure which is applied directly on the FE matrices has been developed. The implementation of this method in the 3D code is presently being carried out and will be presented in the forthcoming report.

7. Common mode impedance calculation

In order to obtain full impedance and admittance matrices, the coupling capacitances and conductances of the motor windings are additionally needed. The extraction procedure is based on electro-quasistatics simulations in the frequency domain which are typically much less challenging than the previously described eddy current calculations. This part of the work will, therefore, not be further discussed here.

When these TLM parameters are available the common mode input impedance of the machine can be computed. The starting point is telegrapher's equation:

$$\frac{d}{dz} \begin{pmatrix} \underline{\mathbf{u}}(z) \\ \underline{\mathbf{i}}(z) \end{pmatrix} = \begin{pmatrix} 0 & -\underline{\mathbf{Z}}'(\omega) \\ -\underline{\mathbf{Y}}'(\omega) & 0 \end{pmatrix} \cdot \begin{pmatrix} \underline{\mathbf{u}}(z) \\ \underline{\mathbf{i}}(z) \end{pmatrix}, \quad (5)$$

where $\underline{\mathbf{Z}}'(\omega) = \underline{\mathbf{R}}'(\omega) + j\omega\underline{\mathbf{L}}'(\omega)$ and $\underline{\mathbf{Y}}'(\omega) = j\omega\underline{\mathbf{C}}'$ are the complex impedance and admittance matrices per unit length, respectively, whereas $\underline{\mathbf{u}}(z)$ and $\underline{\mathbf{i}}(z)$ are vectors of voltages and currents. Since the conductors can be considered electrically short, an approximate solution of (1) can be used. Applying the so called Pi-equivalent circuit approximation, one mesh voltage equation and two node current equations are obtained as

$$\begin{aligned} \underline{\mathbf{u}}(0) - \underline{\mathbf{u}}(l) &= \underline{\mathbf{Z}} \cdot \underline{\mathbf{i}}_z, \\ \frac{1}{2}\underline{\mathbf{Y}} \cdot \underline{\mathbf{u}}(0) - \underline{\mathbf{i}}(0) + \underline{\mathbf{i}}_z &= 0, \end{aligned} \quad (6)$$

$$-\frac{1}{2}\underline{Y} \cdot \underline{u}(l) - \underline{i}(l) + \underline{i}_z = 0,$$

where $\underline{u}(0)$, $\underline{u}(l)$, $\underline{i}(0)$ and $\underline{i}(l)$ are the voltage and current vectors at the front ($z = 0$) and rear end ($z = l$) of the motor, respectively, whereas \underline{Z} and $\frac{1}{2}\underline{Y}$ are lumped element matrices in the Pi-equivalent circuit approximation. The vector of currents through the impedances, \underline{i}_z can be easily eliminated from the system of equations (1). Furthermore, symmetries of the motor can be exploited, in order to reduce the number of unknowns. The 240 kW motor has 60 stator slots and 48 rotor conductors. Hence, considering only conductors within a 60 degree section is sufficient. The reduction is done by substituting, $\underline{u}(z) = \underline{M} \cdot \tilde{\underline{u}}(z)$ and $\underline{i}(z) = \underline{M} \cdot \tilde{\underline{i}}(z)$, where $\tilde{\underline{u}}(z)$ and $\tilde{\underline{i}}(z)$ are the vectors of voltages and currents in the 60 degree section and \underline{M} is a projection matrix imposing the symmetry conditions on the voltages. The resulting system of equations is

$$\begin{pmatrix} \underline{E} + \frac{1}{2}\tilde{\underline{Z}} \cdot \tilde{\underline{Y}} & -\underline{E} & -\tilde{\underline{Z}} & 0 \\ \underline{E} & -[\underline{E} + \frac{1}{2}\tilde{\underline{Z}} \cdot \tilde{\underline{Y}}] & 0 & -\tilde{\underline{Z}} \end{pmatrix} \cdot \begin{pmatrix} \tilde{\underline{u}}(0) \\ \tilde{\underline{u}}(l) \\ \tilde{\underline{i}}(0) \\ \tilde{\underline{i}}(l) \end{pmatrix} = 0, \quad (7)$$

where $\tilde{\underline{Z}}$, $\tilde{\underline{Y}}$, $\tilde{\underline{u}}(0)$ etc. are symmetry reduced submatrices and subvectors, respectively, and \underline{E} represents the unity matrix. The remaining voltage and current unknowns can be eliminated from the system of equations by taking the winding scheme of the motor into account. This is achieved in a similar way as above by using a projection matrix approach. For example, if conductors i and j are connected at the rear end of the motor ($z = l$), this implies $\underline{u}_i(l) = \underline{u}_j(l)$ and $\underline{i}_i(l) = -\underline{i}_j(l)$. The projection matrix imposes these constraints explicitly such that the projected vectors contain only the voltages and current unknowns $\underline{u}_i(l)$ and $\underline{i}_i(l)$ at the rear end of the motor.

In the last step, the conditions at the motor terminals ($\underline{u}_1(0) = U_{com}$) and at the star point are included. The latter is $\underline{i}_{120}(0) = 0$, where the index 120 denotes conductor connected to the star point. Imposing these conditions and solving the resulting system of equations allows to calculate the common mode impedance as $\underline{Z}_{com} = U_{com}/\underline{i}_1(0)$.

In Fig. 10, the simulation results obtained by 2D simulations and the application of the above procedure are compared to measurement data. The reference impedance curve was obtained by the group of Magdun/Gemeinder/Binder (TP1-Binder) by direct measurements on the 240kW motor. While excellent agreement is found for low frequencies, high frequency results show major differences. This might be due to simplifications made in the numerical model where, e.g., the end-windings are omitted. Also a number of material parameters such as the permittivity of the insulation material in the motor are not exactly known. However, as shown in Section 5, the most important source of discrepancy between simulation and measurements at high frequencies is the homogenized equivalent material model for the core laminations which needs to be assumed in 2D simulations. The impedance matrix extraction by 3D simulations including eddy currents in the laminations is presently being carried out. In the forthcoming report, the common mode impedance of the 240kW motor extracted from these simulation data will be presented.

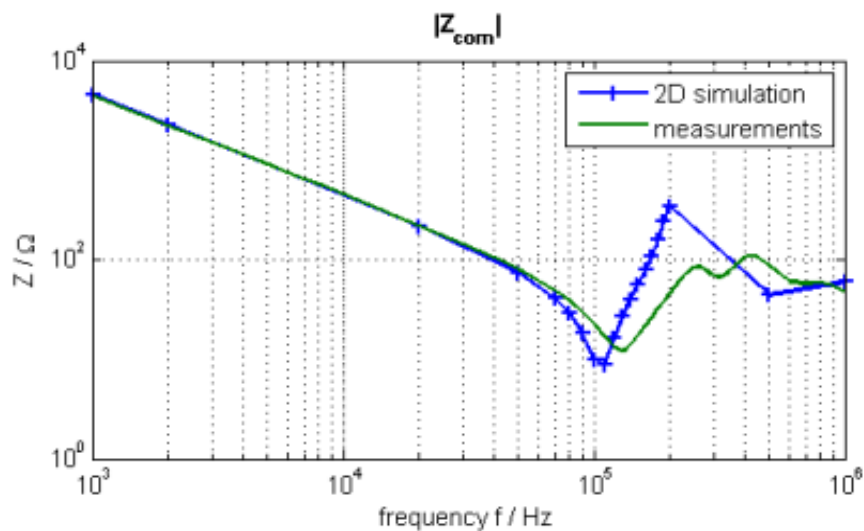


Figure 10 Comparison between the $|Z_{com}|$ of the 240 kW motor extracted from 2D simulations and from measurement data (TP1-Binder).

8. Conclusions

A 3D simulation approach was presented which can be used for full scale eddy current motor simulations including effects of core laminations. The application of high order FE methods on prismatic meshes allows for efficient simulations even for very complicated motor geometries. Furthermore, the results obtained by 3D simulations have been used to validate the commonly used lamination homogenization approaches. Our investigations show that the anisotropic conductivity approach is highly inaccurate except for at very low frequencies. 2D FE simulations based on the equivalent permeability model (1) can be utilized for frequencies of up to 1 kHz where the modeling error remains below 1%. At higher frequencies, however, also this approach fails to properly describe eddy current phenomena in laminated cores. Thus, for the investigation of higher frequency parasitic effects in inverter controlled induction machines full scale 3D eddy current analysis including the lamination geometry is necessary.

9. Final remarks

The closing of the present subproject is scheduled for October, 30 2012. Presently, work is going on for the extraction of the full impedance matrix of the 240kW motor from 3D simulations. This task together with the calculation of the common mode impedance will be concluded by the end of the funding period. The necessary tools for this purpose (the 3D simulation code, the inductance extraction procedure from FE matrices as well as the calculation of the common mode impedance for arbitrary windings) are available. The results of this final investigation will be submitted to the DFG in a separate research report.

The originally planned investigation of the end-windings as well as the implementation of a multi-rate time integration method for transient TLM simulations could not be accomplished according to the schedule. The main reason is the immense effort which was spent in the development and testing of a completely new 3D code for eddy current simulations in core laminations. We were not aware of the large errors resulting from lamination homogenization approaches at high frequencies. This fact has not been pointed out previously, also in the relevant literature. Thus, the development of a new 3D code which is specialized for the simulation of laminated structures was necessary. By this means, however, our group now owns a powerful tool will be used in future work. In particular, the high frequency modeling of the end-windings remains one of our main objectives for future research.

References

- [1] BEDROSIAN, G. et al. "Axiperiodic finite element analysis of generator end regions. II. Application," IEEE Trans. Magn. Vol. 25, No. 4. 1989, pp. 3070–3072.
- [2] BOLDEA, I., and NASAR, S. A. "The Induction Machine Handbook". CRC Press. 2002, Chapter 21.
- [3] CARPENTER, C.J., "The application of the method of images to machine end-winding fields". Proceedings of the IEE - Part A: Power Engineering. Vol. 107, No. 35. 1960, pp. 487–500.
- [4] DE GERSEM, H., and MUETZE, A. "Simulation of electric machine common-mode impedance using a combined TL-FE-analytic model". *Proceedings of ISEF'09*. 2009, paper no. 278.
- [5] DE GERSEM, H., et al. "Transmission-line modelling of wave propagation effects in machine windings". *Power Electronics and Motion Control Conference, EPE-PEMC, 13th*. 2008, pp. 2385-2392.
- [6] DULAR, P., et al. "3-D magnetic vector potential formulation taking eddy currents in lamination stacks into account". *IEEE Trans. Magn.*, vol. 39. 2003, pp. 1147–1150.
- [7] FEMM by David Meeker, vers. 4.2. www.femm.info.
- [8] GAO, Y., et al. "Loss calculation of reactor connected to inverter power supply taking account of eddy currents in laminated steel core." *IEEE Trans. Magn.*, vol. 45, no. 3. 2009, pp. 1044–1047.
- [9] MAGDUN, O., et al. "Prediction of common mode ground current in motors of inverter-based drive systems". *International Aegean Conference on Electrical Machines and Power Electronics, ACEMP '07*. 2007, pp. 2385-2392.
- [10] MAKI-ONTTO, P., and LUOMI, J. "Induction motor model for the analysis of capacitive and induced shaft voltages". *IEEE International Conference on Electric Machines and Drives*. 2005, pp. 1653-1660.
- [11] STOLL, R. L. "The analysis of eddy currents". *Oxford University Press*. 1974.
- [12] TEGOPOULOS, J.A., "Current sheets equivalent to the end-winding currents of turbine generator stator and rotor," AIEE Trans. Pt. III. Vol. PAS-81. 1963, pp. 695–700.
- [13] WANG, Y.-J., and LIU, S.-J. "A Review of Methods for Calculation of Frequency-dependent Impedance of Overhead Power Transmission Lines". *Proc. Natl. Sci. Coun. ROC(A)*, Vol. 25, No. 6. 2001, pp. 329-338.
- [14] JORKS H.; GJONAJ E.; WEILAND T., "Simulation of an induction motor including eddy-current effects in core laminations", IET 8th International Conference on Computation in Electromagnetics (CEM 2011), Wroclaw, Poland, 11-14 April 2011, pp. 54-55.
- [15] JORKS H., GJONAJ E., and WEILAND T., "Three-dimensional simulations of an induction motor including eddy current effects in core laminations," accepted for publication to IET Science, Measurement & Technology, May 2012

6.3. Subproject 3: Microvaristors in the insulation of inverter-fed drives

Dipl.-Ing. Sébastien Blatt

Prof. Dr.-Ing. Volker Hinrichsen

Fachgebiet Hochspannungstechnik, Institut für Elektrische Energiesysteme, TU Darmstadt

E-Mail: blatt@hst.tu-darmstadt.de

1. Work schedule and methods:

Duration (Month)	Description
4	Explanation of the circumstances by estimation and calculations (using TNA software).
5	Fabrication of microvaristor filled test items in cooperation with manufactures under usage of existing (non optimized) materials
1	Planning and construction of test arrangement
2	Performing of measurements of the voltage distribution with steep voltage impulses; use of conventional microvaristor filled isolation
3	Fabrication of microvaristor filled bands and / or varnishes in cooperation with manufactures by using different materials with optimized properties (results from simulations of the other sub-projects)

6	Planning and construction of a test set up for an accelerated electric-thermal aging as well as an aging by partial discharges
5	Performing partial discharges aging tests at microvaristor filled insulation systems and performing of accelerated electric-thermal aging test at different microvaristor filled insulation systems
2	Optimization of the material properties
2	Planning and procurement of a machine with a microvaristor filled insulation system
3	measurements at the machine
3	End of project (publication, final report)

2. Einleitung

In der heutigen Zeit werden zur Regelung von Maschinen immer häufiger Umrichter verwendet. Moderne Umrichter beziehen ihre Spannung aus einem Gleichspannungszwischenkreis, weswegen sie nahezu unabhängig von der Netzspannung betrieben werden. Bei einer Netzspannung von 400 V beträgt die Zwischenkreisspannung 560 V, und die Ausgangsspannung des Umrichters hat einen Wert von +/- 560 V. Die Taktfrequenz der vom Umrichter erzeugten Impulse liegt im Kilohertzbereich mit Anstiegszeiten von weit unter einer Mikrosekunde. Da Umrichter und Maschine häufig räumlich voneinander getrennt betrieben werden, sind Zuleitungen notwendig, die eine Länge von hundert Meter überschreiten können. Aufgrund dieser Länge und der kurzen Anstiegszeiten treten Wanderwelleneffekte auf der Zuleitung auf. Durch den hohen Eingangswiderstand der Maschine, der viel größer als der Wellenwiderstand der Zuleitung ist, kommt es zu Reflexionen der Wanderwellen an den Maschinenklemmen. Im ungünstigsten Fall führen diese Reflexionen zu einer Spannungsverdoppelung am Eingang der Maschine. Diese Überspannungen treten, bedingt durch die hohe Taktfrequenz des Umrichters, mehrere tausend Mal pro Sekunde auf und können zu Teilentladungen führen, die langfristig möglicherweise die Isolation der Ständerwicklung der Maschine zerstören. Weiterhin kommt es durch die kurzen Anstiegszeiten der Umrichterausgangsspannung zu einer ungleichmäßigen Spannungsverteilung innerhalb der Wicklung, was wiederum zu einer zusätzlichen partiell höheren Beanspruchung der Wicklungsisolation führt.

3. Grundsätzliche Fragestellungen

Frühere Untersuchungen haben gezeigt, dass der Einsatz von Metalloxid-(MO-)-Varistoren an den Eingangsklemmen der Maschine, die durch die Wanderwelleneffekte verursachten Überspannungen begrenzen kann [2]. Weiterhin wurde dort nachgewiesen, dass durch die hohe Kapazität der MO-Varistoren die Anstiegszeiten der Spannung am Eingang der Maschine verlängert werden, was sich positiv auf die Spannungsverteilung innerhalb der Ständerwicklung auswirkt. Es stellt sich die Frage, ob Mikrovaristoren, eingebracht in die Isolierlacke oder -bänder der Wicklungsisolation, die gleichen positiven Effekten bewirken können.

Es wird vermutet, dass Mikrovaristoren in der Isolation umrichtergespeister Maschinen die Überspannungen, welche durch die Wanderwelleneffekte entstehen, auf ein akzeptables Maß begrenzen werden. Weiterhin könnten die Anstiegszeiten durch die hohe Permittivität der Mikrovaristoren verlängert werden, was insbesondere die Beanspruchung der Isolation der ersten Windungen vermindern würde.

Um den Einsatz von Mikrovaristoren in der Isolation umrichtergespeister Antriebe untersuchen zu können, ist zunächst ein allgemeines elektrisches Ersatzschaltbild der Ständerwicklung der Maschine in Form eines Netzwerks aus passiven Bauelementen erforderlich. Das Ersatzschaltbild muss in einem weiteren Schritt um weitere nichtlineare Elemente, die den mikrovaristorgefüllten Isolierstoff darstellen, ergänzt werden. Dazu muss das derzeit noch

unbekannte elektrische Verhalten mikrovaristorgefüllter Isolierstoffe bei den in Frage kommenden Frequenzen ermittelt werden. Weiterhin ist das Langzeitverhalten mikrovaristorgefüllter Isolierstoffe unter dem Einfluss von Teilentladungen zu untersuchen. Auch das Langzeitverhalten solcher Isolierstoffe bei dieser speziellen Beanspruchungsform ist noch unbekannt.

4. Mikrovaristorgefüllte Isolierstoffe

4.1. Allgemeines

Mikrovaristoren bestehen genau wie MO-Varistoren aus dotiertem und gesintertem Zinkoxid. Durch spezielle Herstellverfahren entsteht ein Endprodukt in Granulatform im Gegensatz zu den sonst meist zylinderförmigen großvolumigen Energievaristoren. Die Granulatkörner weisen Durchmesser von (10...200) μm auf und besitzen eine nichtlineare Spannungs-Strom-(U-I)- bzw. Feldstärke-Stromdichte-(E-J)-Kennlinie. Ein moderater Anstieg der Spannung führt oberhalb eines bestimmten Schwellwerts zu einem Anstieg des Stromes um mehrere Dekaden. Werden Mikrovaristoren einem Isolierstoff beigemischt, geben sie ihre nichtlinearen elektrischen Eigenschaften teilweise an das resultierende Gesamtsystem weiter. Die hohe Dielektrizitätszahl von Mikrovaristoren ($\epsilon_r = 300 \dots 1000$) führt auch zu einer hohen resultierenden Permittivität des mikrovaristorgefüllten Materials, weshalb die heutige Anwendung von Mikrovaristoren im Wesentlichen in feldsteuernden Kabelgarnituren zu finden ist. Das elektrische Ersatzschaltbild mikrovaristorgefüllter Materialien kann vereinfacht als Parallelschaltung aus einem nicht linearen spannungsabhängigen Widerstand und einem Kondensator angenommen werden. **Abbildung 4.1** zeigt eine Mikroskopaufnahme von Mikrovaristoren. Zu erkennen sind die einzelnen, hier überwiegend kugelförmigen Granulatkörner sowie in jedem dieser Körner eine Vielzahl einzelner zusammengesinterteter ZnO-Partikel, an deren Grenzflächen zueinander jeweils der Varistoreffekt auftritt. Durch die Serien- und Parallelanordnung der vielen ZnO-Partikel innerhalb eines Granulatkorns stellt sich das nichtlineare elektrische Verhalten als intrinsische Eigenschaft jedes einzelnen Granulatkorns ein. Das Mikrovaristorpulver wird mit einem Volumenanteil weit oberhalb der Perkulationsgrenze in eine Polymermatrix (z.B. Epoxidharz) eingemischt, so dass sich relativ stabile feldsteuernde Eigenschaften des resultierenden Isolier- und Feldsteuermaterials einstellen.

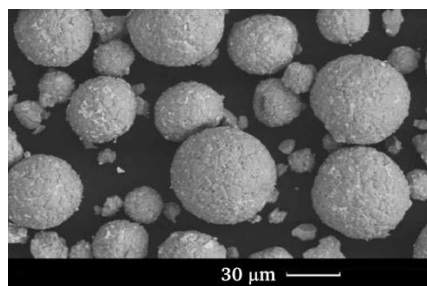


Abbildung 4.1: Mikroskopaufnahme von Mikrovaristoren [1]

4.2. Aufnahme der Kennlinien und Prüfaufbau

Um die elektrischen Eigenschaften mikrovaristorgefüllter Isolierstoffe aufnehmen zu können, ist ein spezieller Prüfaufbau erforderlich, weil die Spannung aus dem Netz stark mit Oberschwingungen belastet ist. Der für die Messungen verwendete Prüfaufbau (siehe **Abbildung 4.2**) besteht unter anderem aus einem Frequenzgenerator, einem linearen Verstärker und einem Transformator. Da der Verstärker nur eine maximale Spannung von 50 V liefern kann, muss die Spannung mit einem Transformator auf höhere Werte hochgespannt werden. Der Vorwiderstand ist notwendig, um den Stromfluss im Falle eines Durchschlages des Prüflings zu

begrenzen. Die Spannung am Prüfling wird mit einem 1000:1-Tastkopf gemessen, und die Strommessung erfolgt durch einen Shunt, der wahlweise auf 1 k Ω oder 100 k Ω umgeschaltet werden kann und geerdet ist.

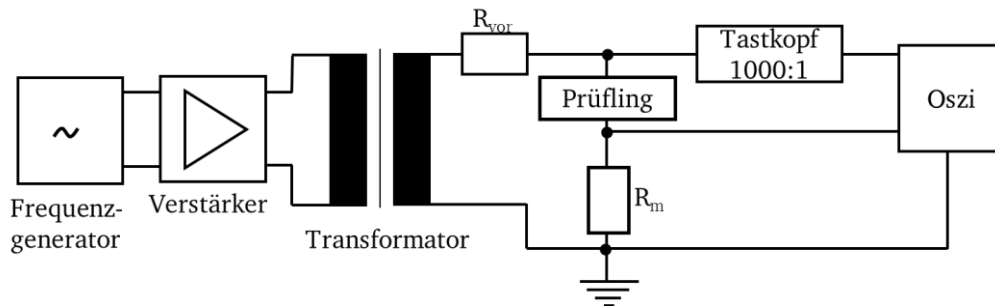


Abbildung 4.2 Prüfaufbau zur Messung der Kennlinie von mikrovaristorgefüllten Isolierstoffen.

Da nur der Volumenwiderstand des Prüflings von Interesse ist, wird der Strom in einer Schutzringkonfiguration gemessen. Bei dieser Anordnung ist die Erdelektrode in eine innere kreisförmige Platte und einen äußeren Ring unterteilt, wobei der äußere Ring direkt und die innere Platte über den Messshunt geerdet ist. Oberflächenströme werden über den Schutzring nach Erde abgeleitet. Die Spannungs- und Stromverläufe werden am Oszilloskop ausgegeben.

4.3. Prüflinge und Auswertung der Ergebnisse

Als möglicher neuartiger mikrovaristorgefüllter Werkstoff für die Isolation umrichter gespeister Maschinen ist unter anderem auch mikrovaristorgefüllter Lack vorgesehen. Zur Prüflingsherstellung wird der Lack in einen Messingteller gegossen. Nach dem Aushärten wird die Oberfläche plangeschliffen und anschließend eine Schutzringanordnung aus Silberleitlack direkt auf die Oberfläche aufgetragen.

Um die Wechselspannungs-Kennlinie des mikrovaristorgefüllten Lacks ausmessen zu können, wird der Prüfling mit einer ideal sinusförmigen Spannung beansprucht. Die resistive Komponente lässt sich zum Zeitpunkt des Spannungsmaximums ermitteln. Zu diesem Zeitpunkt ($dU/dt = 0$) enthält der gemessene Gesamtstrom bei dem angenommenen Modell einer einfachen RC-Parallelschaltung nur die resistive Komponente.

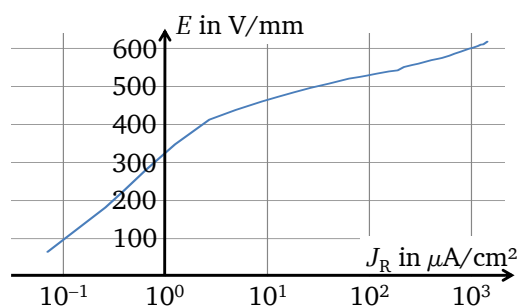


Abbildung 4.3 Gemessene Kennlinie einer Probe mit mikrovaristorgefülltem Lack

Abbildung 4.3 zeigt die gemessene Feldstärke in Abhängigkeit der resistiven Komponente der Stromdichte. Der Schwellenwert (per Definition diejenige elektrische Feldstärke, bei der sich eine Stromdichte von 1 $\mu\text{A}/\text{cm}^2$ einstellt) beträgt hier ca. 330 V/mm. Die kapazitive Komponente des gemessenen Gesamtstroms lässt sich zum Zeitpunkt des Spannungsnulldurchgangs ermitteln. Die Auswertung des kapazitiven Stroms ergibt eine relative Permittivität von 25 mit steigender Tendenz bei steigender Spannung

5. Simulation der elektrische Maschine

5.1 Allgemeines

Um den Einsatz von Mikrovaristoren in der Isolation der Maschine untersuchen zu können, wird ein Simulationsmodell der Maschine benötigt. Das Simulationsmodell muss derart aufgebaut sein, dass eine Simulation der Spannungsverteilung in der Maschine bei identischem Eingangsimpuls möglichst die Messergebnisse wiedergibt, die in [2] dargestellt sind. Diese Messungen wurden an einem dreiphasigen 7,5-kW-Motor, der mit Anzapfungen versehen ist (siehe **Abbildung 5.1**), durchgeführt. Die Maschine wurde ausschließlich im Leerlauf betrieben und mit Impulsen mit einer Anstiegszeit von 100 ns (siehe graue Kurve in **Abbildung 5.2**) beansprucht. Das Kabel zwischen Frequenzumrichter und Maschine hatte eine Länge von 98 Meter [2]. **Abbildung 5.2a** zeigt die Leiter-Erd-Spannung, wie sie an dieser Maschine aufgenommen wurde.

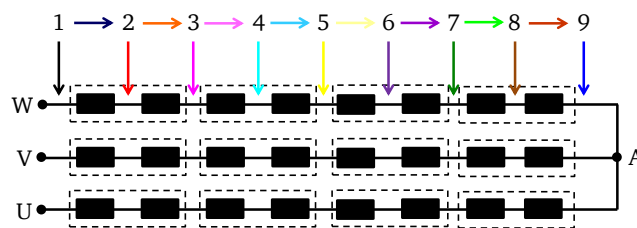


Abbildung 5.1 Position der Abgriffe in der Maschine sowie die Spannungsfälle über den einzelnen Spulen [2]

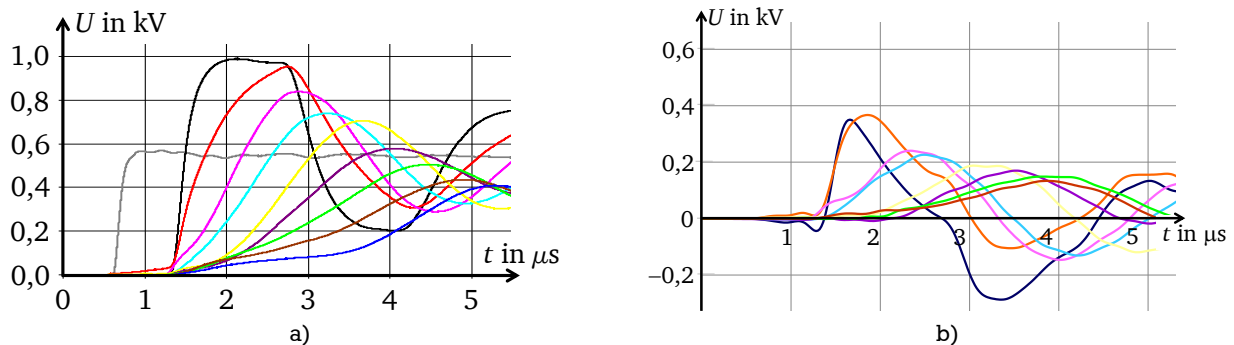


Abbildung 5.2 Gemessene Leiter-Erdspannungen (a) und Spannungsdifferenzen (b) zwischen den Spulen innerhalb der Maschine. Jede Farbe in a) steht für eine Spule der Wicklung. Es sind somit die Verhältnisse an den ersten neun Spulen dargestellt. b) zeigt die Spannungsdifferenzen zwischen je zwei aufeinanderfolgenden Spannungen in a).

Wie in **Abbildung 5.2a** zu sehen ist, weist die Leiter-Erd-Spannung am Eingang der Maschine (schwarze Kurve) annähernd die doppelte Amplitude auf wie die Zwischenkreisspannung des Umrichters. Weiterhin sind die Leiter-Erd-Spannungen an den ersten vier Spulen ebenfalls überhöht. Ebenfalls von Interesse sind die Spannungsdifferenzen zwischen den Spulen (siehe **Abbildung 5.2b**) innerhalb der Maschine, da die Isolation auch gegen diese Spannungen ausgelegt sein muss.

5.2. Simulationsmodell

Um untersuchen zu können, ob Mikrovaristoren in der Isolation der Maschine überhaupt die gewünschten positiven Effekte haben, muss ein elektrisches Ersatzschaltbild bestehend aus passiven Bauelementen (d.h. Widerstände, Spulen und Kondensatoren) erstellt werden. Die

Wicklung einer Maschine kann in einzelne Spulen unterteilt werden, die wiederum mehrere Windungen enthalten. **Abbildung 5.3** zeigt ein einfaches Ersatzschaltbild der Windung einer Spule einer Maschinenwicklung.

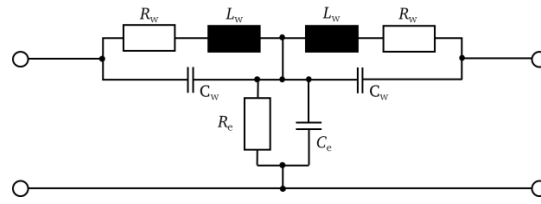


Abbildung 5.3 Ersatzschaltbild einer Windung

Die Elemente R_w in **Abbildung 5.3** beschreiben den Leiterwiderstand, die Elemente L_w die Induktivität einer Windung. Die Kondensatoren C_w im Ersatzschaltbild beschreiben die Kapazitäten zwischen zwei benachbarten Windungen. C_e ist die Kapazität zwischen Windung und geerdetem Statorgehäuse ("Erdkapazität"). Der Widerstand R_c stellt den Isolationswiderstand der Leiterisolierung dar. Dieser ist so hochohmig, dass er für alle folgenden Betrachtungen vernachlässigt werden kann. Für die Aufstellung des Ersatzschaltbildes einer kompletten *Spule* muss das Ersatzschaltbild nach **Abbildung 5.3** mehrmals in Reihe geschaltet werden. Dabei ist zu berücksichtigen, dass sich die Kapazitätswerte für jede Windung ändern. Das liegt daran, dass die Position des Leiters in der Spule immer eine andere ist. Ferner existieren weitere Kapazitäten auch zwischen nicht direkt benachbarten Windungen, die im Model ebenfalls berücksichtigt werden müssen. Parallel zu den Kondensatoren werden spannungsabhängige Widerstände angeordnet, die die resistiven Eigenschaften der Mikrovaristoren in der Maschinenisolation darstellen. Um schließlich das vollständige Ersatzschaltbild der Maschine zu erhalten, müssen mehrere Spulen hintereinander zu einer *Wicklung* geschaltet werden. Das komplette Ersatzschaltbild einer Spule ist in **Abbildung 5.4a** gezeigt.

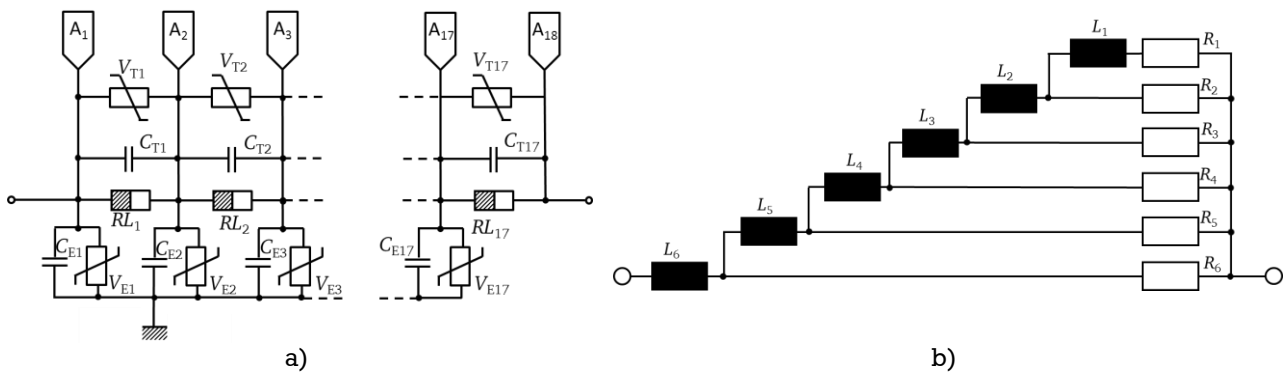


Abbildung 5.4 Elektrisches Ersatzschaltbild einer Spule (a) mit dem „Leiterkreis“ (Erläuterung siehe Text)(b)

Da bei dem Einsatz von Umrichtern höhere Frequenzen, bedingt durch die kurzen Anstiegszeiten der Umrichterspannung und die hohe Taktfrequenz, auftreten, muss das Ersatzschaltbild der Maschine modifiziert werden. Induktivität und Widerstand einer Windung müssen zur Berücksichtigung des Skin-Effekts durch einen sogenannten „Leiterkreis“ (siehe **Abbildung 5.4b**) ersetzt werden. Für niederfrequente Ströme wirkt diese Anordnung insgesamt niederimpedant, hochfrequente Ströme dagegen werden abhängig von der Frequenz in unterschiedliche Zweige gedrängt. Die Werte für die passiven Bauelemente wurden aus [3] entnommen.

5.3. Simulation

5.3.1 Allgemeines

Die Simulationen wurden hier mit der Software „Simplorer“ der Firma „Ansoft“ durchgeführt. Das, in „Simplorer“ aufgebaute Simulationsmodell beinhaltet die drei Abschnitte, welche in **Abbildung 5.5** gezeigt sind.

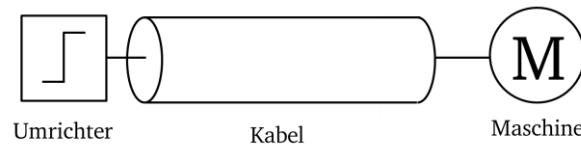


Abbildung 5.5 Blockschaltbild Umrichter-Maschine (a) und innere Aufteilung der Maschine in Spulen (b).

Der Umrichter wird in dem Simulationsmodell als Impuls-Spannungsquelle mit einer Anstiegszeit 100 ns und einer Impulsdauer von 50 μ s modelliert. Bei einer Gesamtsimulationsdauer von 100 μ s wird bei einer Taktfrequenz von 10 kHz eine Periode nachgebildet. Die Zuleitung zwischen Umrichter und Maschine wird durch ein Kettenleiterersatzschaltbild bestehend aus passiven Elementen, ähnlich dem der Windung einer Maschine (siehe **Abbildung 5.3a**), nachgebildet. Um den Skineneffekt zu berücksichtigen, wird für das Kabel ebenfalls ein „Leiterkreis“, wie in **Abbildung 5.4b** gezeigt, verwendet. Allerdings unterscheiden sich die Werte der Elemente von denen der Maschinenwicklung und wurden aus [4] entnommen. Durch das Zufügen von Mikrovaristoren in der Isolation der Maschine kommt es, bedingt durch die nichtlineare Leitfähigkeit des Materials, zu einem Stromfluss durch die Isolation der Maschine und damit zu einer erhöhten Verlustleistung. Um diese zusätzliche Verlustleistung bestimmen zu können, werden mittels der Simulationssoftware Spannungsfall und Stromfluss an den Elementen $C_{E,n}$ und $V_{E,n}$ ermittelt. Die Multiplikation beider Größen ergibt die Verlustleistung in Abhängigkeit von der Zeit, über eine Periodendauer integriert die mittlere Verlustleistung (Gleichungen 5.1 und 5.2).

$$P(t) = \sum_{n=1}^{17} U_n(t) \cdot I_n(t) \quad (5.1)$$

$$P_M(t) = \frac{1}{T} \int_0^T P(t) \cdot dt \quad (5.2)$$

5.3.2. Simulation ohne Mikrovaristoren in der Maschinenisolation der

Mit einer Simulation ohne Mikrovaristoren in der Maschinenisolation wird das elektrische Ersatzschaltbild überprüft. Hierfür werden die Zweige, in denen sich die nichtlinearen Widerstände befinden, offen gelassen. Eine Simulation mit den Werten nach [3] ergibt, dass die simulierten Spannungen in der Maschine sich in ihren Anstiegszeiten von den gemessenen Spannungen unterscheiden. Um die Ergebnisse zu optimieren, wird die relative Permittivität von zwei auf vier erhöht. Dadurch können die Ergebnisse verbessert werden, und die simulierten Spannungsverläufe und -verteilungen sehen für zumindest für die ersten vier Spulen den gemessenen Spannungen in [2] recht ähnlich (**Abbildung 5.6a**).

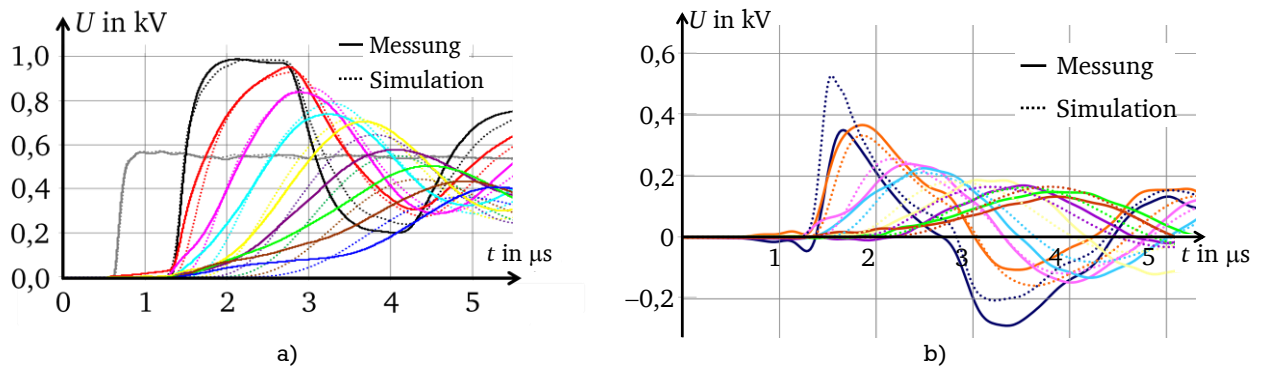


Abbildung 5.6 Gemessene und simulierte Leiter-Erdspannung (a) und Spannungsdifferenzen (b) entlang den Spulen innerhalb der Maschine.

Abbildung 5.6b zeigt die die aus **Abbildung 5.6a** errechneten Spannungsdifferenzen entlang den Spulen. Die in der Isolation umgesetzte Verlustleistung ist mit ca. 13 mW sehr gering und wird durch Umladevorgänge der parasitären Kapazitäten hervorgerufen.

5.3.3. Simulation mit erhöhter Permittivität

Durch die Zugabe von Mikrovaristoren in der Isolation steigen bedingt durch die hohe Permittivität von Mikrovaristoren die Kapazitäten in der Wicklung. Um diesen Einfluss untersuchen zu können, werden im folgenden Schritt die Kapazitäten im Modell angepasst und die resistive Komponente als unendlich groß angenommen. Dabei wird der Einfachheit halber eine konstante relative Permittivität von 25 angenommen. Die simulierten Leiter-Erd-Spannungen und die daraus errechneten Spannungsdifferenzen zwischen den Spulen sind im Vergleich zu der Simulation mit normaler Permittivität in **Abbildung 5.7** zu sehen. In dieser Abbildung ist zu erkennen, dass sich die Spannungsanstiegszeiten in der Wicklung verlängern. Dadurch sinkt die maximale Spannung um ca. 6,6 % auf ca. 920 V. Die dielektrische Verlustleistung steigt wegen der höheren Permittivität auf ca. 126 mW an.

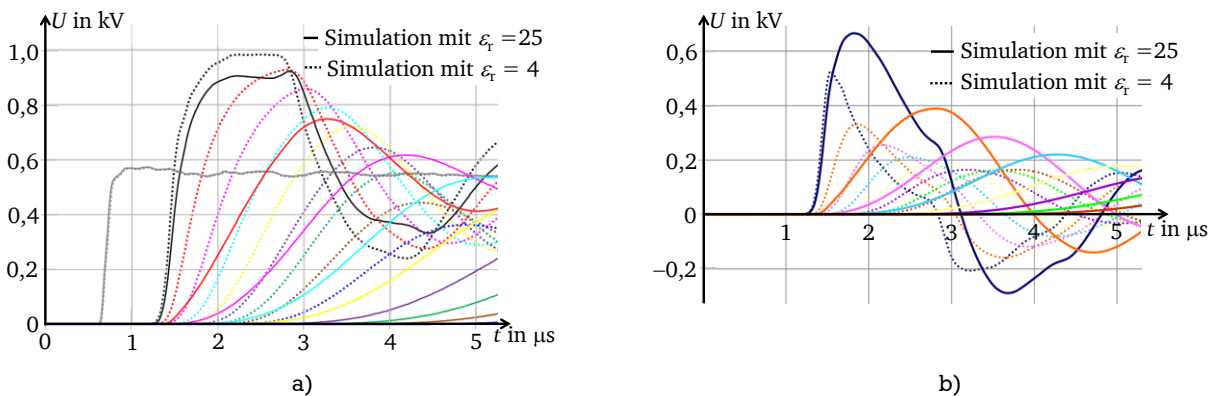


Abbildung 5.7 Simulierte Leiter-Erdspannung (a) und Spannungsdifferenzen (b) entlang den Spulen innerhalb der Maschine bei einer Permittivität von 4 und 25.

Weiterhin ist nach **Abbildung 5.7b** die Amplitude der Spannungsdifferenz zwischen erster und zweiter Spule gestiegen. Für kurze Zeit wird sogar die die Amplitude der Zwischenkreisspannung überschritten.

5.3.4. Simulation mit Mikrovaristoren in der Maschinenisolation

Um eine Simulation mit Mikrovaristoren in der Maschinenisolation durchführen zu können, müssen die nichtlinearen Widerstände in **Abbildung 5.4a** berücksichtigt werden. Für den resistiven Anteil werden im Simulationsmodell die gemessenen Kennlinien aus **Abschnitt 4** verwendet. Da mit der Software Simplorer nur absolute Größen (d.h. Spannungen und Ströme) verarbeitet werden können, müssen die Kennlinien aus **Abschnitt 4** in diese Größen umgerechnet werden. Durch den runden Querschnitt der Maschinenwindungen entsteht ein inhomogenes elektrisches Feld zwischen den Windungen. Hierdurch wird die Berechnung des nichtlinearen Widerstandes zwischen den Leitern wesentlich erschwert. Aus diesem Grund werden die nichtlinearen Widerstände aus der Geometrie eines Plattenkondensators aus den Kapazitäten nach [3] ermittelt. Mit dieser Vorgehensweise lassen sich näherungsweise die nichtlinearen Leitwerte aus der in **Abschnitt 4** Fehler! Verweisquelle konnte nicht gefunden werden. ermittelten nichtlinearen Leitfähigkeit bestimmen.

Im Folgenden wird die Kennlinie aus **Abbildung 4.3** betrachtet. Da dieser Prüfling nur bis 615 V ausgemessen werden konnte, wurde die Kennlinie logarithmisch bis zu einer Spannung von 1500 V extrapoliert, damit auch die auftretenden Überspannungen bei der Simulation berücksichtigt werden können. Für die Untersuchung verschiedener Schaltpunkte wurden weitere Kennlinien aus der gemessenen Kennlinie generiert. Die generierten Kennlinien beginnen alle bei der gleichen Leitfähigkeit und werden bis zum Schaltpunkt E_S angenähert, anschließend verlaufen die Leitfähigkeiten im logarithmischen Maßstab parallel zueinander. Die verwendeten Kennlinien sind in **Abbildung 5.8** gezeigt.

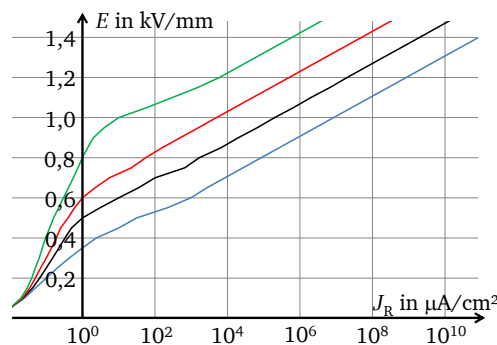


Abbildung 5.8 Gemessene und generierte Kennlinie.

Die Simulationsergebnisse (siehe **Tabelle 5.1** und in **Abbildung 5.9**) zeigen, dass das Hinzufügen der nichtlinearen Widerstände im Modell keine weitere Änderung der Anstiegszeiten (im Vergleich zu der Simulation mit erhöhter Permittivität) mit sich bringt. Mit sinkendem Schaltpunkt werden jedoch die Überspannungen zwischen Leiter und Erde (Statorgehäuse) und die Spannungsdifferenzen zwischen den Spulen geringer. Gleichzeitig erhöht sich aber auch die gemittelte Verlustleistung über eine Periode. Mit dem Extremfall ($E_S = 330$ V/mm) werden die Überspannungen vollständig eliminiert, dafür steigt die dielektrische Verlustleistung auf über 2 kW, was völlig inakzeptabel ist. **Tabelle 5.1** zeigt die maximale am Eingang der Maschine auftretende Spannung (U_{max}), die maximale prozentuale Überspannung an den Maschinenklemmen, die maximale Spannungsdifferenz zwischen erster und zweiter Spule (ΔU_{max}) sowie die über eine Periode gemittelte Verlustleistung (P_1), jeweils in Abhängigkeit vom Schaltpunkt (E_S) der verwendeten Kennlinie. Bei den Angaben der prozentualen Überspannung wurde von der mittelen gemessenen Zwischenkreisspannung (graue Kurve in **Abbildung 5.2**) von 550 V ausgegangen.

Tabelle 5.1: Simulierte Kennwerte bei verschiedenen Schaltpunkten und Permittivitäten

E_S in V/mm	ϵ_r	U_{max} in V	Überspannung in %	ΔU_{max} in V	P_I in W
-	4	985	79	527	13 m
-	25	920	72,7	665	126 m
800	25	828	50,5	641	18
600	25	730	32,7	595	43
500	25	642	16,7	536	173
330	25	550	0	465	2065

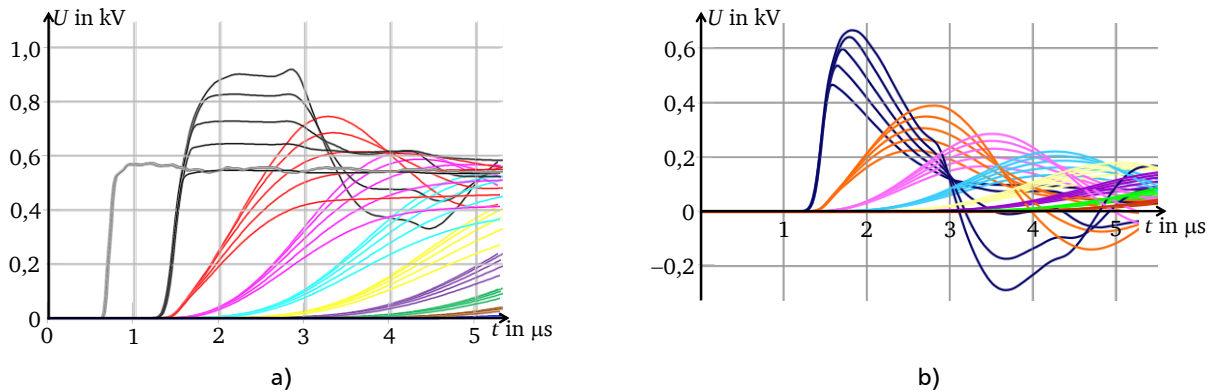


Abbildung 5.9 Simulierte Leiter-Erdspannung (a) und Spannungsdifferenzen (b) entlang der Spulen innerhalb der Maschine bei verschiedenen Schaltpunkten.

In **Abbildung 5.9a** und **5.9b** sind alle simulierten Spannungsverläufe mit erhöhter Permittivität ($\epsilon_r = 25$) dargestellt. Da durch Einbringen von Mikrovaristoren sich alle Kapazitäten erhöhen und somit die dielektrische Verlustleistung stark ansteigt, wird im Folgenden durch eine weitere Simulation die Auswirkung einer zwischen Wicklung und Statorgehäuse eingebrachten Schicht herkömmlichen Isoliermaterials untersucht. Diese Maßnahme wirkt der durch die Mikrovaristoren bedingten Erhöhung der Erdkapazität entgegen, während die übrigen Wicklungskapazitäten durch die Permittivität der Mikrovaristoren geprägt werden. Im elektrischen Ersatzschaltbild **Abbildung 5.4a** entspricht das dem zusätzlichen Einfügen kleiner Kapazitäten jeweils zwischen den parallelgeschalteten Elementen C_{en}/V_{en} und dem geerdeten Stator. Hierfür wird die Permittivität für die Kapazitäten $C_{E,n}$ in **Abbildung 5.4a** auf einen Wert von vier gesetzt, die Dielektrizitätszahl der übrigen Kapazitäten ($C_{T,n}$ **Abbildung 5.4a**) beträgt 25. Die nichtlinearen Widerstände, die parallel zu den Erdkapazitäten platziert sind, werden aus der Simulation herausgenommen Für die übrigen nichtlinearen Widerstände wird die blaue Kennlinie aus **Abbildung 5.8** verwendet.

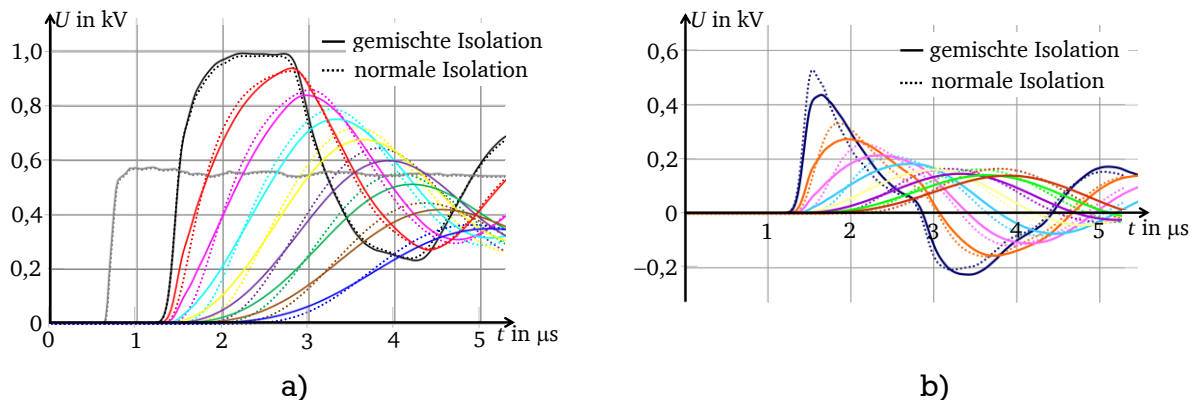


Abbildung 5.10 Simulierte Leiter-Erdspannung (a) und Spannungsdifferenz (b) entlang der Spulen innerhalb der Maschine bei gemischten Isolation und einer konstanten Permittivität von 4.

Die Simulationsergebnisse (siehe **Abbildung 5.10**) dieser Konfiguration zeigen, dass es bezüglich der Leiter-Erd-Spannungen keinen Unterschied macht, wenn in der Nut zusätzlich eine herkömmliche Isolation eingelegt wird. Die Eingangsimpedanz der Maschine ist in diesem Fall genauso hoch, wie bei der normalen Isolation. Dadurch wird die Spannungswelle reflektiert und es kommt wieder zu einer beinahe Verdopplung der Spannung am Eingang der Maschine. Die Spannungsfälle über den Spulen können hingegen etwas vergleichmäßigt werden. Der Spannungsfall über der ersten Spule konnte um 17 % auf 436 V gegenüber der Simulation mit herkömmlicher Isolierung verringert werden.

6. Zusammenfassung und Ausblick

In diesem Teilprojekt ist es durch ein aufwendig entwickeltes Simulationsmodell gelungen sowohl die Spannungsverteilung in der Maschine als auch die dielektrischen Verluste in der Maschinenisolation zu bestimmen. Durch Erweiterung dieses Modells war es schließlich möglich, den Einfluss von Mikrovaristoren zu untersuchen. Ein Problem in diesem Teilprojekt war die Herstellung von mikrovaristorgefüllten Prüflingen, mit denen die Kennlinie ausgemessen werden sollte. Es ließ sich kein Hersteller finden, der mikrovaristorgefüllte Bänder zur Verfügung stellen konnte. Mit dem mikrovaristorgefüllten Lack, der von der Firma „Von Roll“ zur Verfügung gestellt wurde, ist bisher noch kein stabiles Verfahren gefunden worden, einen geeigneten Prüfling zu erstellen. Der verwendete Lack wirft beim Aushärten Blasen, die vermutlich durch das Austreten des Lösungsmittels bei gleichzeitiger Vernetzung der Oberfläche entstehen. Aus diesem Grund konnte das Langzeitverhalten des mikrovaristorgefüllten Lackes unter Umrichterspannung noch nicht untersucht werden, obwohl hierfür bereits ein Alterungsversuchsstand aufgebaut wurde. Um wenigstens das Ausmessen der Kennlinie zu ermöglichen, wurde die Oberfläche des Prüflings plangeschliffen.

Da die Erstellung des Simulationsmodells wegen seiner Komplexität viel zeitintensiver war als ursprünglich angenommen, konnte die für dieses Teilprojekt angedachte Motorette nicht gebaut werden.

Mit dem erstellten Simulationsmodell konnte gezeigt werden, dass Mikrovaristoren einen positiven Einfluss auf die Spannungsverteilung in der Maschine haben. Die Überspannungen, die durch Wanderwelleneffekte auf dem Kabel zwischen Umrichter und Maschine entstehen, können durch Auswahl einer geeigneten Kennlinie bzw. eines geeigneten Schaltpunkts der Kennlinie reduziert werden. Allerdings steigt die Verlustleistung, bedingt durch Einbringen nichtlinear halbleitenden Materials in die Isolation der Maschine. Schon das Einbringen einer mikrovaristorgefüllten Isolation mit einem Schaltpunkt von 800 V/mm bringt eine Reduktion der absoluten Überspannung um 36 %, bei vertretbaren Verlusten von 18 W. Nach [5] muss eine 7,5-kW-Maschine mit vier Polen, der Klasse IE3 einen Wirkungsgrad von 90,4 % besitzen. Hierbei fallen zusätzliche 18 W (0,24 %) nicht stark ins Gewicht.

Insgesamt muss ein Kompromiss zwischen den zugelassenen Überspannungen und den auftretenden Verlusten in der Isolation gefunden werden. Wie auch schon in [2] ausgeführt, wird man sinnvollerweise eine Dimensionierung wählen, die im Dauerbetrieb die Überspannungen nur geringfügig begrenzt und dementsprechend nur Verlustleistungen im Promille-Bereich erzeugt, jedoch im Falle kurzzeitig auftretender erhöhter Spannungen (Bremsbetrieb, Richtungswechsel der Maschine) wirksam wird.

Um Aussagen über die Einsatzmöglichkeit von Mikrovaristoren in der Isolation umrichtergespeister Antriebe treffen zu können, sind (beschleunigte) Langzeitversuche an mikrovaristorgefüllten Isolierstoffen notwendig. Zum einen muss die Langzeit-Teilentladungsbeständigkeit untersucht werden. Weiterhin ist das Langzeitverhalten von

mikrovaristorgefüllten Isolierstoffen unter Dauerbeanspruchung von Umrichterspannung unbekannt. Diese Untersuchungen können durchgeführt werden, sobald es möglich ist, mikrovaristorgefüllte Prüflinge in reproduzierbarer Qualität zu fertigen. Daran wird derzeit noch gearbeitet. Die für die Versuche erforderlichen Alterungsversuchsstände sind aufgebaut und einsatzbereit. In diesen können in drei parallelen Versuchen die Temperatur, die Frequenz sowie die Zwischenkreisspannung als der in Frage kommenden Beschleunigungsfaktoren [2] variiert werden.

Quellenverzeichnis

- [1] H. Gramespacher, J. Svahn, F. Greuter, T.Christen, “Microvaristor based field grading elements for HV terminations”, XIIIth International Symposium on High Voltage Engineering, Rotterdam (NL) 2003.
- [2] A. Rocks: *Einsatz von Metalloxid-Varistoren zum Überspannungsschutz pulsumrichtergespeister Drehfeldmaschinen*, Dissertation, Darmstadt 2009.
- [3] O. Magdun, A. Binder, C. Purcarea, A. Rocks, “High-Frequency Induction Machine Models for Calculation and Prediction of Common Mode Stator Ground Currents in Electric Drive Systems”, 13th European Conference on Power Electronics and Applications, Barcelona (Spanien), 2009.
- [4] O. Magdun, A. Binder, C. Purcarea, A. Rocks, B. Funieru, “Modeling of Asymmetrical Cables for an Accurate Calculation of Common Mode Ground Currents”, Energy Conversion Congress and Exposition, San José (USA) 2009,
- [5] DIN EN 60034-30 (VDE 0530-30): 2009-08

6.4. Subproject 4: Motor-friendly and high efficient inverter for electrical drives

Dipl.-Ing. Calin Purcarea

M-Tech. Jayalakshmi Kedariseti, starting 1st November 2010

Prof. Dr.-Ing. Peter Mutschler

Institut für Stromrichtertechnik und Antriebsregelung, TU Darmstadt

E-Mail: purcarea@srt.tu-darmstadt.de, jaya@srt.tu-darmstadt.de

Work schedule and methods:

Phase	Period (Months)	Description	Obs.
A	10	Evaluation, Design and Simulations.	
A1	2	Derivation of expressions for optimal energy use (level of trip currents) in resonant cycle operation, dependent of instantaneous value of load current.	Ready
A2	1	Design of resonant circuit for desired dV/dt reduction.	Ready
A3	1	Circuit simulations, first with ideal elements.	Ready
A4	1	Improvement of simulation models for semiconductors to consider switching and conduction losses based on properties from datasheets.	Ready
A5	1	Design of an inductor model for core and copper losses.	Ready
A6	2	Design of control strategies for particularities of quasi resonant	Ready

		(QR) DC-link converter.	
A7	1	Circuit simulation, now with complete models of semiconductors and resonant inductor, including the losses. Determination of total losses.	Ready
A8	1	Losses comparison between hard-switched converters with output filters and studied QR topologies. Chose of QR converter topology to be implemented and realized.	Ready
B	8	Set-up hardware realisation (Power Part)	
B1	2	Design, construction and testing of resonant inductor.	Ready
B2	1	Chose of power semiconductors. Development of driving circuit.	Ready
B3	3	Design of mechanical construction (Low inductive current paths, reduced EMI, accessibility for separate losses measurements between resonant circuit and inverter bridge, cooling)	Ready
B4	2	Converter construction.	Ready
C	6	Set-up hardware realisation (Control Part)	
C1	2	Chose the control unit: FPGA or DSP? Switching instants of different transistors forming the resonant circuit must be provided from a fast information processing unit (in best case FPGA). On the other hand it must be clarified if FPGA capacity is sufficient for integrating the complex driving and control algorithms of both resonant converter and motor drive into one single system.	Ready
C2	4	Circuit design and construction of eventual interface units (Multi-layer design for external construction). Function test.	Ready
D	6	Design and implementation of firmware (FPGA) / software (DSP) for modulation techniques (special for resonant operation), control current and protection. Familiarization with specific development tools and environments for FPGA / DSP.	Ready
E	6	Measurements, comparisons and evaluations	
E1	2	Test set-up: commissioning and testing.	Ready
E2	2	Measurement of effective losses, current and voltage waveforms and harmonics content.	Ready
E3	2	Comparison of effective losses, current / voltage waveforms and harmonics content with conventional hard-switched converters + inverter output filters (both dV/dt and common mode reduction).	Ready

1.1. Introduction

Feeding electrical motors by long cables using PWM inverters has become lately problematic due to developments in semiconductor technology. Most used in converters, insulated gate bipolar transistors IGBTs switch voltages with high gradients, about $10\text{kV}/\mu\text{s}$. On one hand, faster switching transients lead to the reduction of switching losses and therefore, permissible higher switching frequencies, reduction of harmonics and audible noise at motors. On the other hand, bigger voltage gradients combined with long feeders lead to high frequency parasitic effects, like overvoltage at motor terminals leading to insulation stress, high common mode (CM) ground current, bearing currents, etc. The effects of using fast switching semiconductors with long cables are reported in the literature [1], [2]. Voltage reflections are produced due to the impedance mismatch between cable and motor. PWM waves traveling on long cable between inverter and motor behave like traveling waves on transmission line [1]. They produce high frequency (HF) oscillations and over voltages at motor terminals [1]. The ringing voltage at the motor terminals, due to high dv/dt and motor cable, causes HF noise [3]. HF noise is also caused by the CM voltage between phases and ground, and switching of the semiconductors [5]. The bearing currents due to

the fast switching IGBTs are reported in [6]. The bearing currents depend upon the size of the motor, rate of the rise of the CM voltage and level of the CM voltage.

The common solution for mitigating HF parasitic effects is the use of output filters [2]–[5], [7]. dV/dt filters increase the rise and fall time of the voltages and there by voltage peaks are reduced. This filter does not reduce the CM voltage and so the bearing stress is not eliminated [4]. With sine-wave EMC filters, the motor is fed by a sinusoidal phase voltage [5]. These filters completely eliminate the bearing damage. Because of high inductor L and capacitor C , these filters have a poor dynamic characteristic and cannot be used universally [4]. The other solutions used in the literature to mitigate HF parasitic effects are use of damping circuits [7], matching the cable and motor input impedance [8], better winding insulations, modified modulation techniques for CM voltage reduction [9] and soft gate drive techniques, etc. The resonant converters can also provide solutions for reducing the voltage gradients [10].

In the literature [11]–[22], the increased efficiency can be achieved with resonant converters. The resonant circuits are a combination of passive elements or passive and active elements. But the main operating principle of these converters is to bring a low voltage across and/or low current through semiconductor devices during a switching status change. There by switching losses in resonant converters are reduced. The rising and falling of voltage and currents can also be controlled to reduce the ringing effects.

For resonant DC-link converters, resonant circuit is located near to the DC-link side. The problem with some resonant DC-link converters is that pulse width modulation (PWM) cannot be used. In this case, the switching instants are determined by a resonant circuit [11], [12]. For some resonant DC-link converters, resonant circuit is not continuously oscillating. Whenever a switching is needed, the resonant circuit is initiated by active components. These converters are called quasi-resonant DC-link converters and are capable of PWM [13]–[22]. For motor-friendly inverter application, this type of inverters is suitable due to the voltage spectrum. A method to reduce the CM voltage in QRDCL inverters is proposed in [23]. This method of common mode voltage reduction is possible only when the inverter is completely separated from DC-link voltage. The quasi-resonant circuit must also provide variable zero voltage duration.

The QRDCL inverters in [13]–[17] use more than two auxiliary switches. The circuit presented in [19] requires a large capacitor for resonant operation, which keeps a nearly constant voltage during a resonant cycle and energy of the resonant circuit is not zero for the steady state. The resonant circuit presented in [20] needs only two additional switches and makes all the switches in the power inverter operate with zero switching losses. The energy of the resonant circuit is zero in the steady state. For a motor-friendly application, this circuit is investigated in this project.

In this research project, a motor friendly quasi-resonant dc-link inverter is being designed and experimentally tested. This soft switching inverter is then compared with the conventional hard switched voltage source inverter together with filter under identical load conditions. At low modulation index, the resonant cycles are longer due to long zero voltage vector. During a zero voltage vector, resonant inductor current free wheels through an auxiliary diode and inverter switches. Higher the freewheeling time, more losses will be produced. This effect is observed in efficiency measurements. So a lossless variable zero voltage duration is necessary for high efficiency of the QRDCL inverter. At the end, a motor friendly quasi-resonant DC-link inverter with loss less variable zero voltage is proposed. The performance of this QRDCL inverter is verified through the simulations.

1.2. Description of the work performed

1.2.1. Analysis of Quasi-resonant DC-Link Inverters

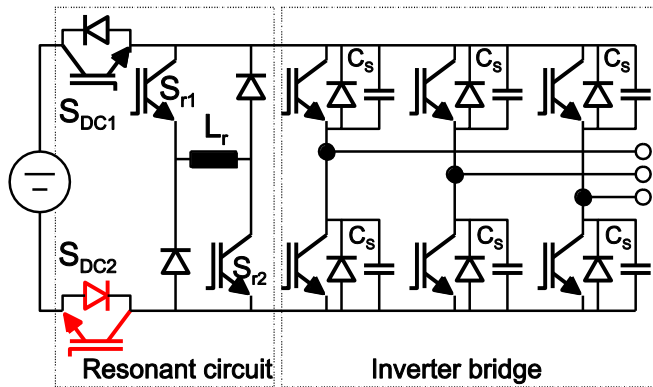


Figure 1 The parallel three switch quasi-resonant circuit (Topology T1)

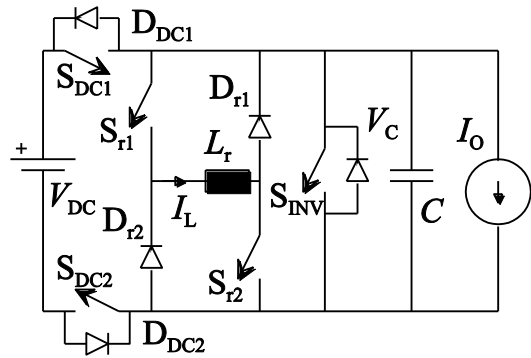


Figure 2 Simplified circuit of topology T1

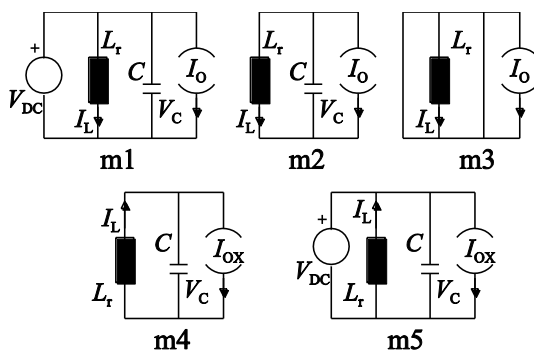


Figure 3 Operating modes of topology T1

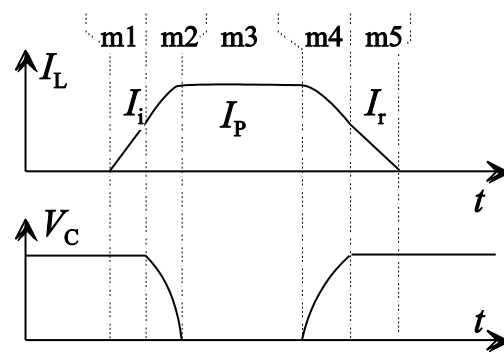


Figure 4 Theoretical waveforms of 'T1'

The circuits presented in [14] and [20] are designed, simulated and then compared. Finally, one QRDCL inverter is selected and implemented for the reduction of high frequency parasitic effects. The topology “T1” shown in Figure 1 uses three switches and one inductor for resonant circuit. To understand better the functionality, a simplified equivalent circuit is presented in Figure 2. The equivalent current source I_o represents the inverter’s DC-link current, whose value and direction depends on the individual phase currents of the machine and the actual PWM state [21]. The different operation modes are shown in Figure 3 and operational waveforms of the resonant circuit are in Figure 4. The switches S_{r1} and S_{r2} are closed and the current i_L in the inductor begins to increase linearly until trip current I_i is reached (m1, see Figure 4). When i_L reaches I_i , S_{DC1} and S_{DC2} can be turned off and the resonance between L_r and C yields a zero voltage condition on the inverter bridge (m2). At this point, i_L reaches its positive peak value I_p and V_C will be zero. Now the resonant current free wheels through paths $S_{r1}-D_{r1}$ and $S_{r2}-D_{r2}$ and the inverter bridge input voltage V_C is clamped to zero (m3). To end this mode the switches S_{r1} and S_{r2} are turned off and the current flows through the diodes and recharges the capacitor C to V_{DC} (m4). Now S_{DC1} and S_{DC2} can be turned on again while the anti parallel diodes D_{DC1} and D_{DC2} are conducting. The remained energy (I_r) in the inductor is returned to the DC voltage source (m5).

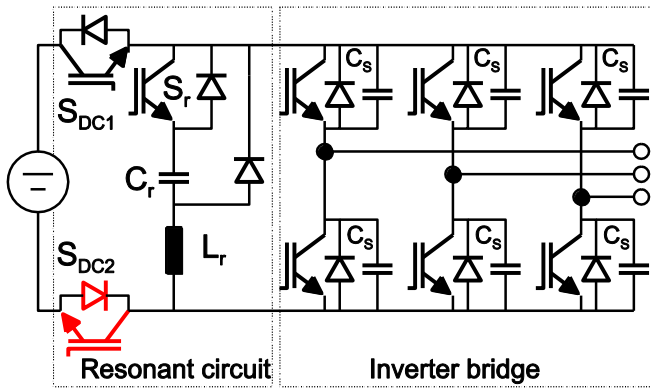


Figure 5 The parallel two switch quasi-resonant circuit (Topology T2)

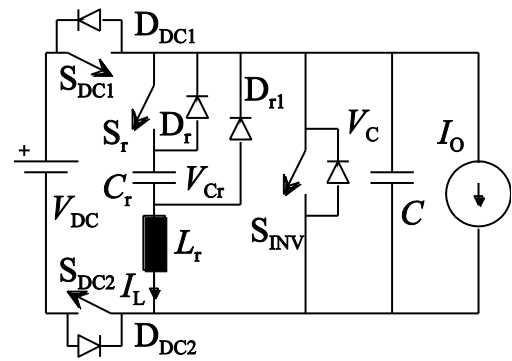


Figure 6 Simplified circuit of topology T2

Similar operation principle is valid for topology “T2” with simplified equivalent circuit presented in Figure 6 and with state variables’ wave forms in Figure 8. Individual states are depicted in Figure 7. The resonant cycle starts with the turn-on of the switch S_r (M1). As soon as the current i_L reaches the trip current I_{Tp1} , the switch S_{DC1} is turned off under ZVS conditions (M2). At this moment starts the resonance between L_r , C_r and C , which yields a zero voltage condition on the inverter bridge. When the zero voltage is obtained, the resonant current commutates to the inverter’s freewheeling diodes (M3). At ZVS condition, all six bridge switches are simultaneously turned on. This is done to provide a path for the resonant current i_L , since eventually its direction will change. The resonance between L_r and C_r decreases the inductor current and changes its direction.

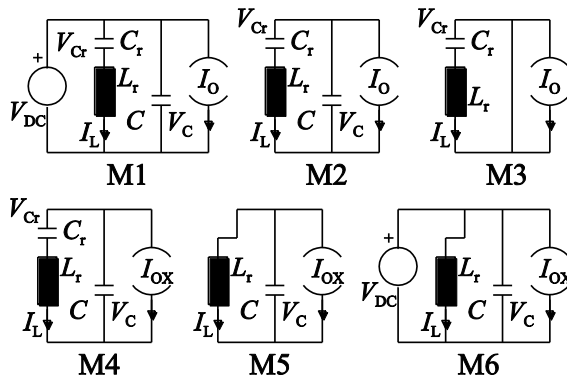


Figure 7 Operating modes of topology T2

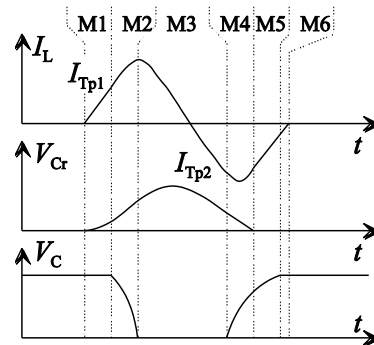


Figure 8 Theoretical waveforms of T2

At this moment the new switch state is set under ZVS condition (M4) and the load current is changed to the new value I_{Ox} , decided by the next PWM state. The resonant current i_L through the switches commutates to the snubber capacitors C and begins to charge them. The voltage V_C is restored to the level of the DC-link voltage (M6), where D_{DC1} and D_{DC2} become forward biased and the excess resonant energy is transferred back to the DC link capacitor. When D_{DC1} and D_{DC2} are conducting, S_{DC1} and S_{DC2} are turned on under ZVS conditions.

1.2.2. Design of the Quasi-resonant DC-Link Inverters

In order to determine the value of resonant elements for a certain dv/dt , a compromise should be found because: 1) The inductor L_r should be small so that resonant transition interval and peak resonant voltage V_{Cr} will be small. However, a small L_r could result in large peak resonant current of i_L and high dv/dt ; 2) An increase in the capacitor C_r can limit the peak resonant voltage of V_{Cr} at the cost of large peak resonant current of i_L and high dv/dt ; 3) The increase of the capacitor C_s results in low dv/dt but high peak resonant current i_L and resonant voltage V_{Cr} . From simulations of resonant circuit, the following values for passive elements lead to best compromise: $(dv/dt)_{min} = 600V/\mu s$; $L_r = 30\mu H$; $C_r = 0.44\mu F$; $C = 0.147\mu F$.

For the presneted QRDCL converter topologies, the trip currents for all load currents are calculated such that: a) at the end of the resonant cycle the DC-link voltage is restored; b) the amplitudes of the resonant current are minimized. The resonant cycle is heavily influenced by the initial load current I_O and by I_{OX} at the next switching state. Figure 9 shows the optimal values for trip currents for topology “T2”. It can be noticed that each case leads to different trip currents [21]. Thus, optimal resonant energy is provided for all possible cases of the DC-link currents.

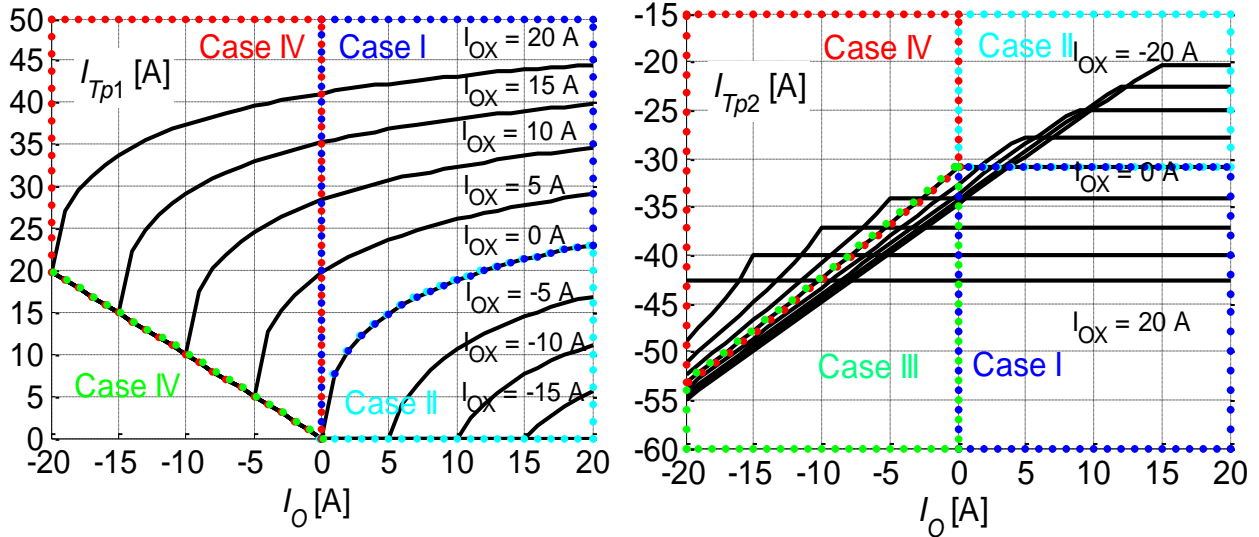


Figure 9: Optimal trip currents (I_{TP1} and I_{TP2}) for topology T2.

1.2.3. Modulation scheme

In the conventional space vector modulation, it requires 6 resonant cycles per switching period T_S , resulting in poor DC-link voltage utilization. Figure 10 shows a modified modulation where each active vector is followed by a zero vector. With an extended zero voltage period, it requires 2 resonant cycles per switching period. During the resonant operation, S_{DC2} is opened along with S_{DC1} . Then the dc link is completely separated from the inverter bridge and there by the common mode voltage is zero during the resonant operation. The zero voltage period (\dot{V}_{07}) during the resonant operation of Mode m3/M3 is effectively equivalent to the zero voltage vector (\dot{V}_0 or \dot{V}_7) of PWM. In order to accommodate the zero voltage vector within a resonant cycle, the zero voltage period can be extended. Then the CM voltage during zero vector reduces to zero (Figure 10). Thus, only during PWM periods, when an active voltage vector is selected, the CM voltage will be $\pm V_{dc} / 6$.

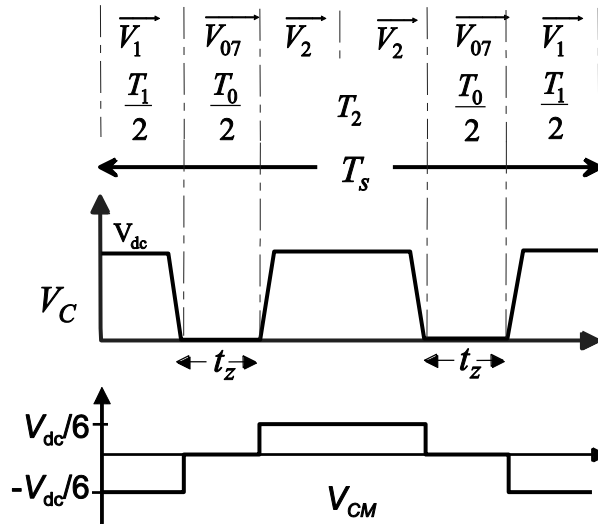


Figure 10: Modified SVPWM

1.2.4. Estimation of power losses

Simulation models for resonant converters are developed and implemented in Ansoft’s Simplorer® network simulation software. Reference [22] describes the estimation of power losses from simulations using ideal switches and post processor estimation program with the help of datasheets. This method of estimation of power losses decreases the simulation time and labour effort. For all the devices, the instantaneous on-state voltage versus current and the current versus turn-on and turn-off energy are read from the data sheets. The switching and conduction losses are roughly estimated for both quasi-resonant topologies. They are compared in Figure 11 for two points of load operation. The converter topology T2 has low conduction and switching losses compare to T1 because of less number of resonant switches required for resonant operation. Therefore, this topology is chosen further for practical implementation and testing.

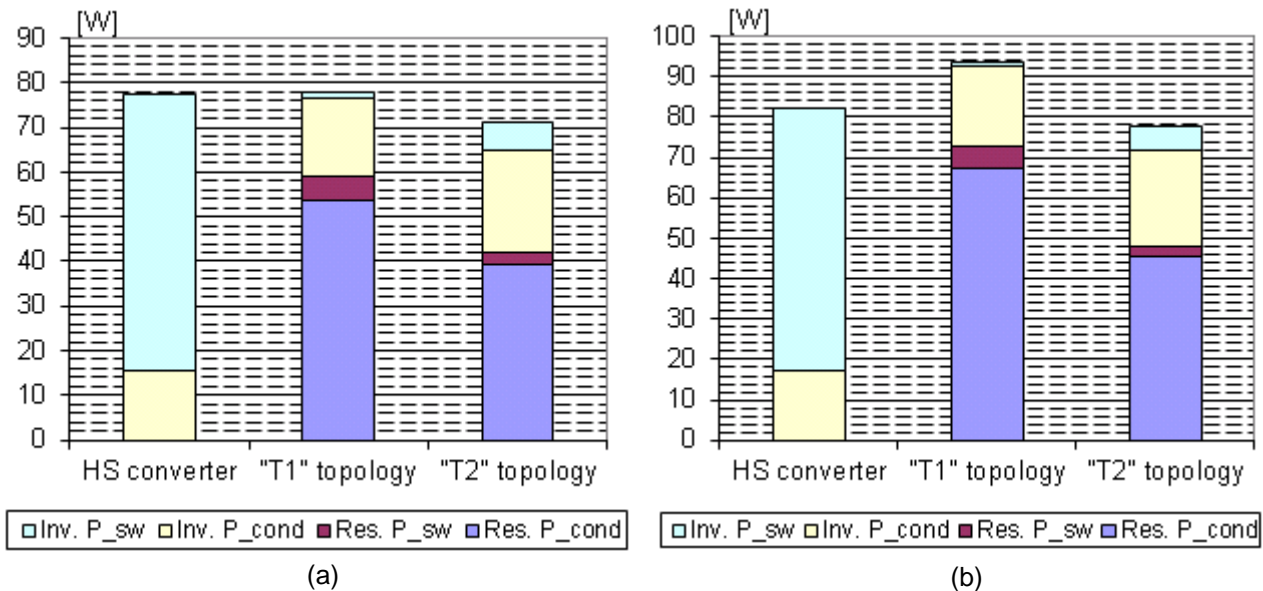


Figure 11 Semiconductor losses for (a) 2.8 kW motor load (b) 3.5 kW motor load

1.3. Experimental Setup

Figure 12 shows the hardware schematic. The diode bridge is connected to 415 V, 50 Hz, 3-phase power grid. The inverter is fed from a diode bridge rectifier and 4-Quadrant chopper. The inverter is controlled by using a FPGA. The laboratory setup consists of a 4 kW squirrel cage induction machine. In order to load the induction motor, a dc generator is coupled to the shaft of the induction motor. The electric power is fed back to the DC-link capacitor via a 4-quadrant chopper.

The inverter can operate as both hard switching (HS) and soft switching (SS) inverter. During the HS inverter mode, DC-link switches S_{DC1} and S_{DC2} are closed and resonant switch S_r is opened perpetually. The input voltage is measured after the DC-link switches. In order to reduce the parasitic effects for HS inverter, the output filters are connected to the inverter. The efficiency measurements are done with two different filters. In one case, the Schaffner FN510-24-33 output filter is connected in order to reduce the dv/dt gradients. In the other case, the EPCOS Sine-wave EMC output filter (B84143V0011R127) is connected to reduce the EMC effects. During the SS inverter mode, the DC-link switches S_{DC1} , S_{DC2} and the resonant switch S_r are controlled in such a way to have zero voltage switching. The resonant elements are designed for the maximum inverter output voltage gradient of $600\text{V}/\mu\text{s}$. With the help of an additional switch and extended resonant cycle, common mode voltage level is also reduced. So the output filters are not needed when the inverter is operating in SS mode. The efficiency is measured for inverter together with resonant circuit, i.e. QRDCL inverter.

The hardware setup of the inverter together with the FPGA board and interface board is shown in Figure 13. The induction machine is coupled to the DC generator and loaded electrically (Figure 15). The DC generator is fed with constant field current, and the armature current is controlled using a 4-Quadrant chopper. The chopper is controlled using a real time PC and an AMI (Antrieb Module Interface) board. In Figure 14, the 4-Q chopper together with AMI board is shown. Figure 16 shows the output filters along with the resonant inductor.

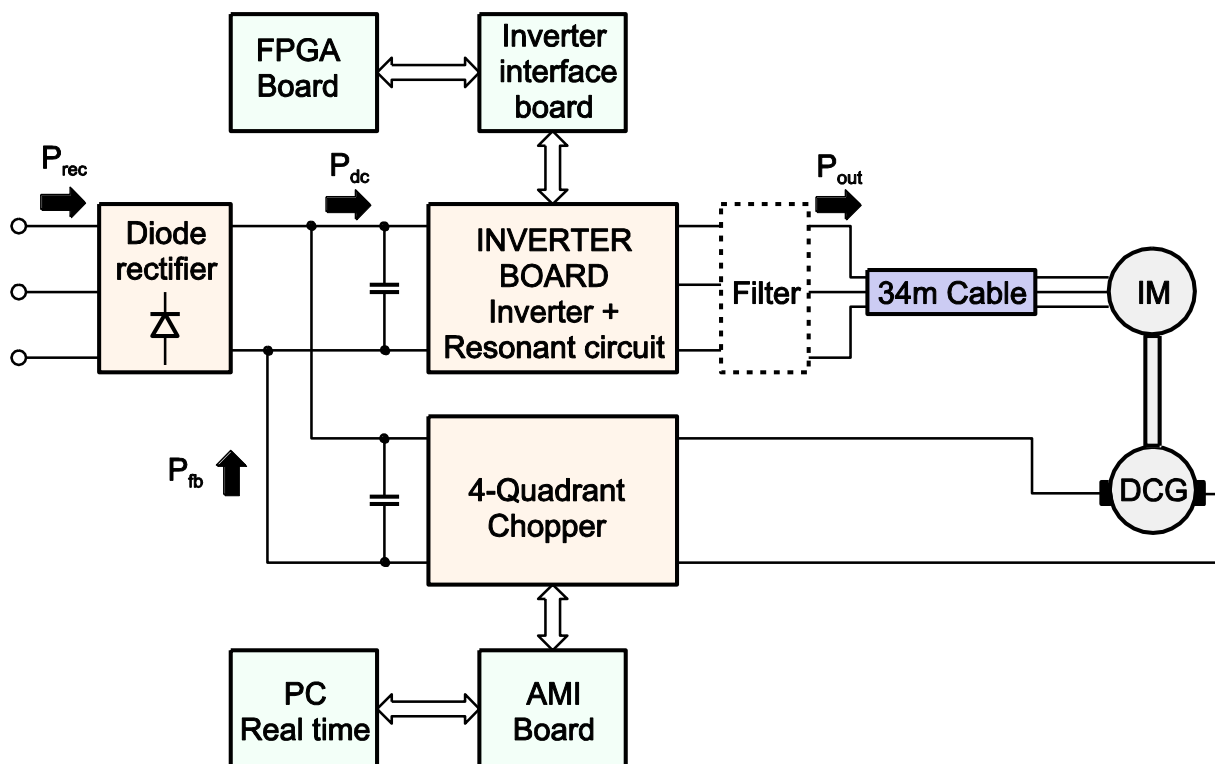


Figure 12: Hardware schematic

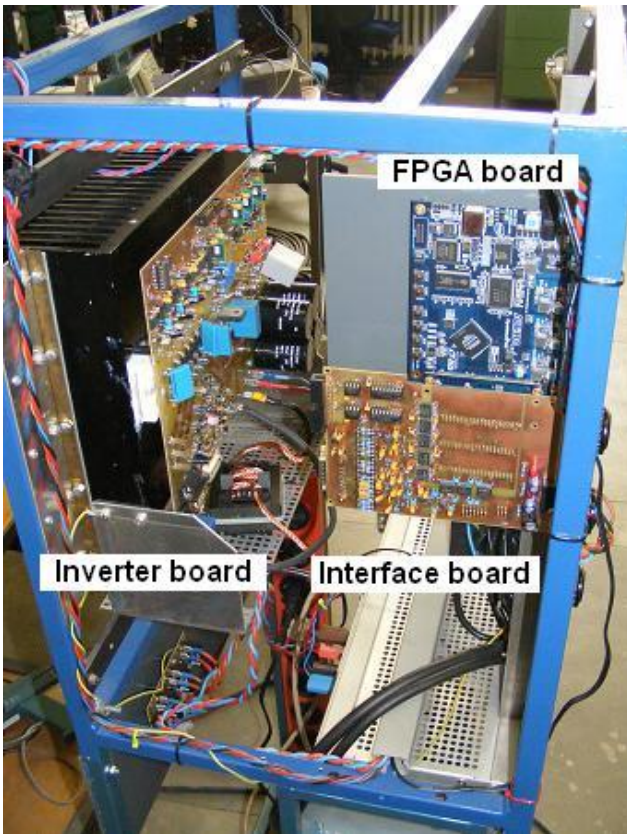


Figure 13: Laboratory setup : Inverter board with control unit

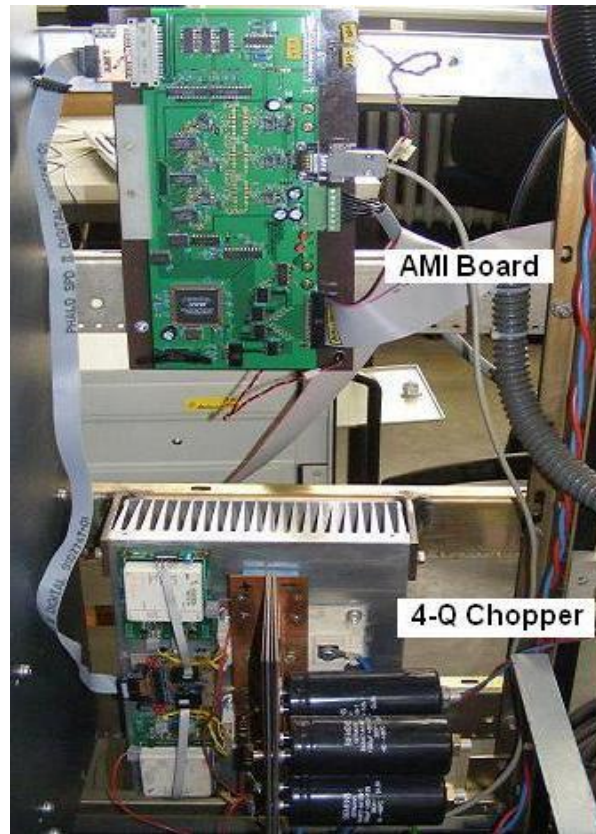


Figure 14: Laboratory setup : 4-Q chopper for DC machine braking

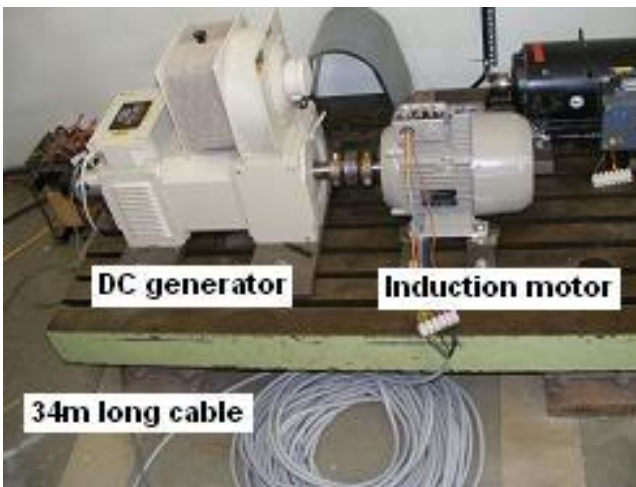


Figure 15: Induction motor coupled to DC generator



Figure 16: Output filters along with a resonant inductor (in oval)

1.4. FPGA Based Controller

The indirect field oriented controlled induction machine is fed by the quasi-resonant DC-link soft switching inverter. The total control of the soft switching inverter together with the motor has been realized in a single chip FPGA. Altera’s QUARTUS II ® web edition FPGA design software is used to implement the control of the inverter and the induction motor. The control is written in a very simple Altera Hardware Description Language (AHDL). The control algorithm has decomposed into several blocks. All the blocks execute in parallel with individual sampling rates.

TU Darmstadt FB18 ETit

DFG Forschergruppe FOR575
Sprecher: Prof. Dr.-Ing.habil Dr.h.c. A. Binder

By using a state machine, each of these individual blocks can be forced to execute sequentially, thereby having the advantages of both sequential and parallel processing. The firmware in the FPGA can be divided into sixteen major functional blocks and is shown in Figure 17.

1. ADC control – Controls the three analog to digital converters.
2. Encoder counter control – counts the periods (coarse position) based on the sign of incremental signals.
3. Speed calculation – The differentiation is implemented together with the low-pass filter of first order, which computes the speed signal from the position.
4. Speed reference value filter – It is a first order low pass filter with the time constant of speed control.
5. Speed controller – a PI controller with anti-windup is used.
6. Currents $\alpha\beta$ to abc transformation – Clarke transformation is used.
7. Currents abc to $\alpha\beta$ transformation – Park transformation is used.
8. Current (i_d) controller – a PI controller with anti-windup is used.
9. Current (i_q) controller – Identical to the current (i_d) controller.
10. Voltages dq to $\alpha\beta$ transformation – Park transformation is used.
11. Calculate switching times – Based on space vector PWM, switching times are calculated.
12. Calculation of modified switching times – For a resonant cycle implementation, short vector on times are eliminated.
13. Modulation scheme – The switching times are compared against a triangular carrier and switching instants are generated.
14. Control of a resonant circuit and inverter bridge – Every change in the inverter switching status is done during a resonant cycle zero voltage interval.
15. Trip currents look up table – Based on the inverter input currents, trip currents are recalled from the SSRAM memory.
16. Monitoring – This block monitors the signals and in case of fault, disconnects the DC link capacitor from the inverter bridge.

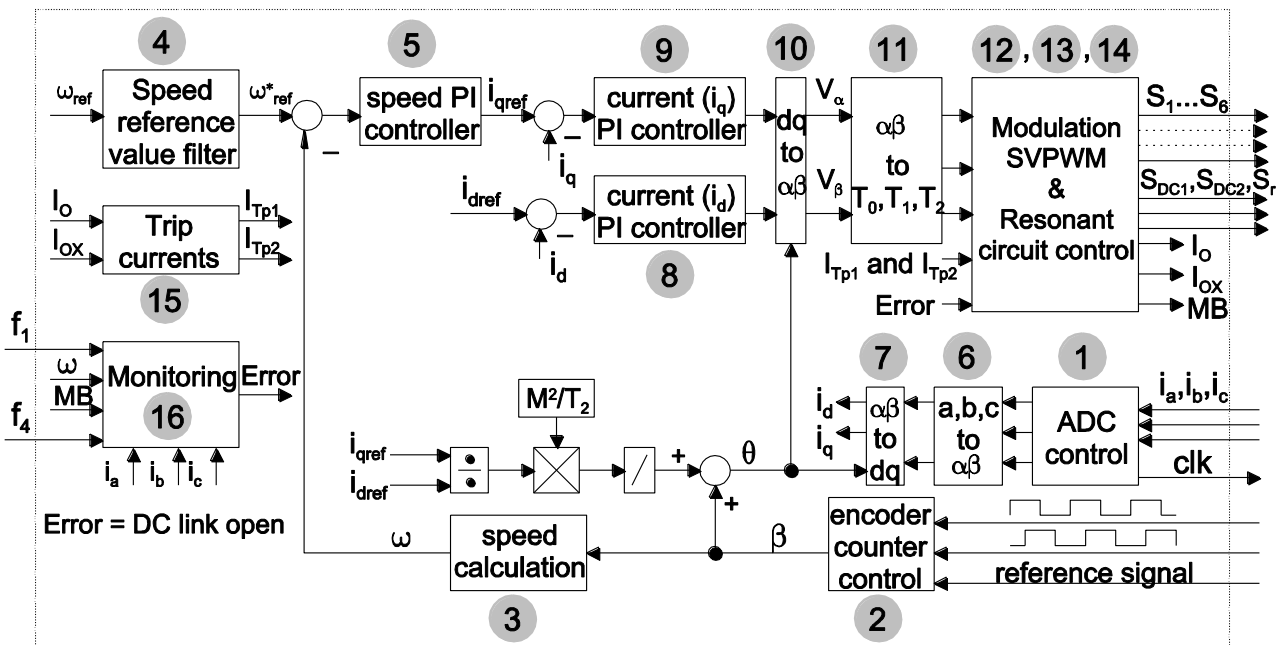


Figure 17 Block diagram of indirect field oriented control and quasi resonant DC-link inverter control in a FPGA

1.5. Experimental results

1.5.1. Resonant cycle

In Figure 18, the inverter bridge input voltage (V_C), resonant capacitor voltage (V_{Cr}) and resonant inductor current (i_L) are shown. The inverter bridge input voltage (V_C) is made to become zero by resonant operation. The inverter switches change their status within this zero voltage period. For the selected design parameters, the peak voltage (V_{Cr}) on the resonant capacitor will be always less than the DC-link voltage. Even though the peak currents in the resonant inductor are higher, the average value of the resonant inductor current is low.

As discussed in the section 1.2.3, the resonant zero voltage period is used for implementing zero vector intervals of PWM. As the duration of zero vector changes with the modulation index of PWM, the length of a resonant period also changes. At low modulation index, the duration of a zero vector is high and resonant cycles are longer as shown in Figure 18 (b). The zero voltage period can be prolonged by keeping shoot-through switching state of the inverter bridge longer. If we keep all the inverter switches closed further the capacitor voltage V_{Cr} discharges to zero and the total energy is stored in the resonant inductor only. Until we apply the next switching state to the inverter bridge, the inductor current i_L freewheels through the diode D_{r1} and the inverter switches. In ideal case, this current i_L will be constant. But under real conditions, the resonant inductor current (i_L) is slowly decreasing. It is due to the losses in the freewheeling path, i.e. resonant inductor losses, diode (D_{r1}) conduction losses and losses in the inverter bridge. If this decrease in the current is higher, at the end of a resonant cycle, the inverter bridge voltage will not be able to reach the DC-link source voltage again. So the energy stored in the inductor, i.e. the trip current level I_{Tp1} should be increased to compensate these losses.

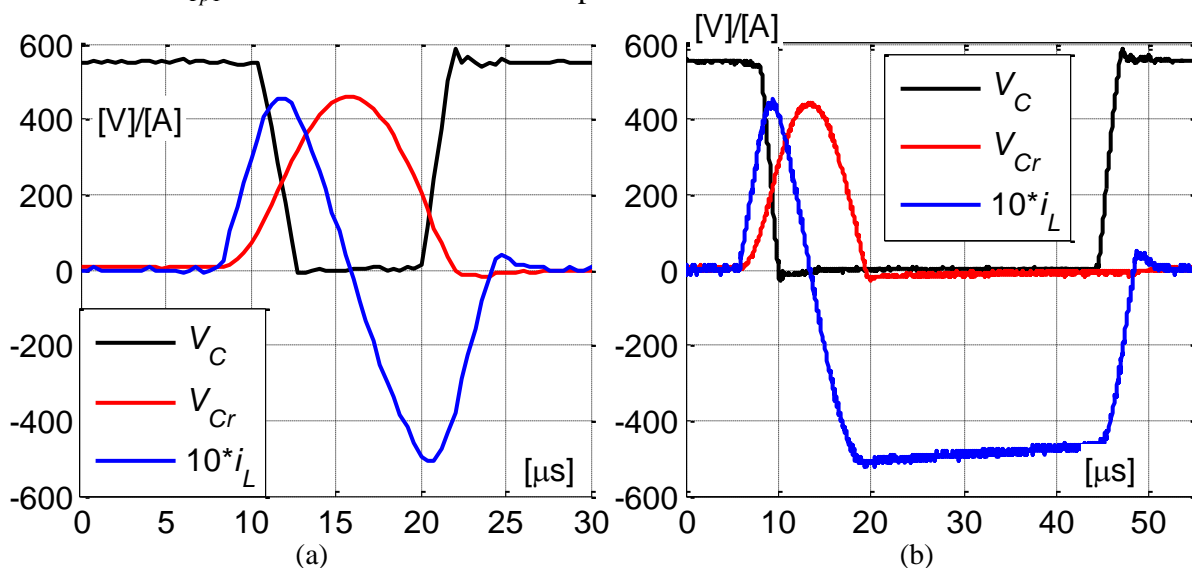
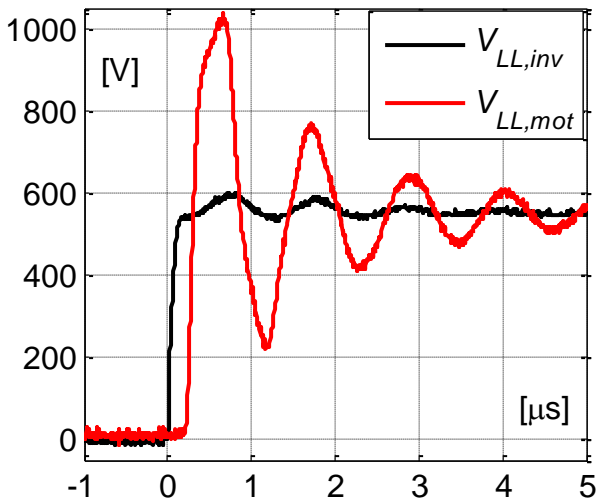


Figure 18 Resonant circuit waveforms (a) short resonant cycle (b) long resonant cycle

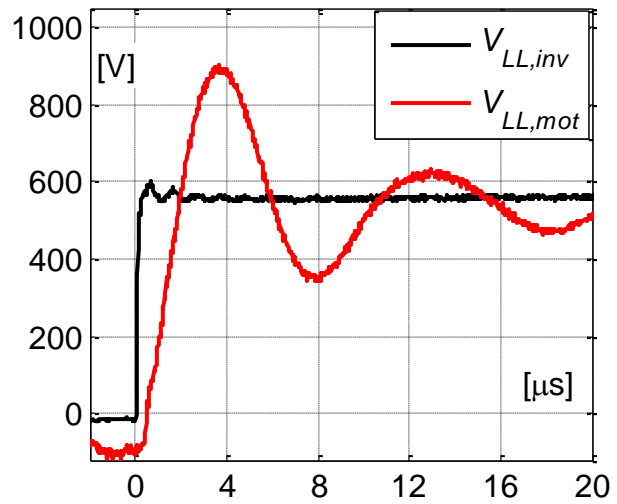
1.5.2. Motor friendly characteristics

In order to evaluate the motor friendly characteristics of QRDCL inverter, the experimental results regarding the line to line voltage, line to earth voltage and common mode voltage are taken at both the ends of the long cable. To appreciate the performance of QRDCL inverter, the measurements are also taken for the HS inverter with and without filters.

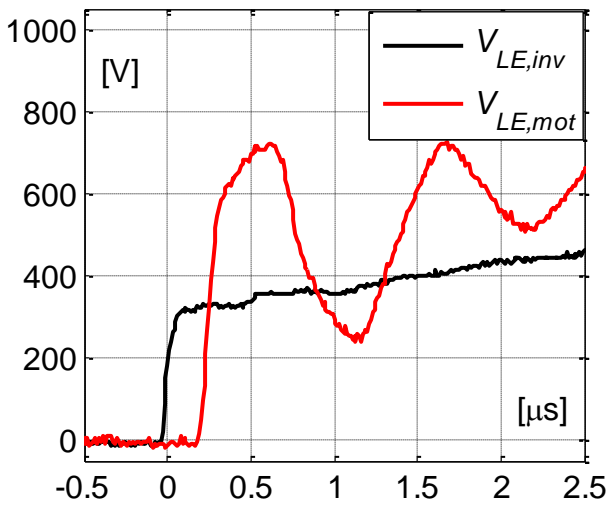
Hard switching inverter + Long cable + No filter (Figure 19): Over voltage at the motor side due to the high dv/dt and long cable can be observed. The oscillation period depends upon the cable stray elements. The common mode voltage has higher harmonics due to the long cable. Because of the high dv/dt in CM voltage, there will be a significant amount of leakage current through the capacitive coupling of stray capacitances.



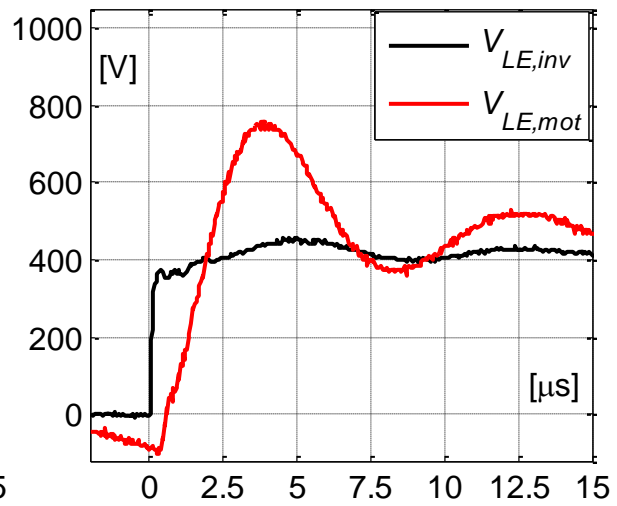
(a) Line to line voltage



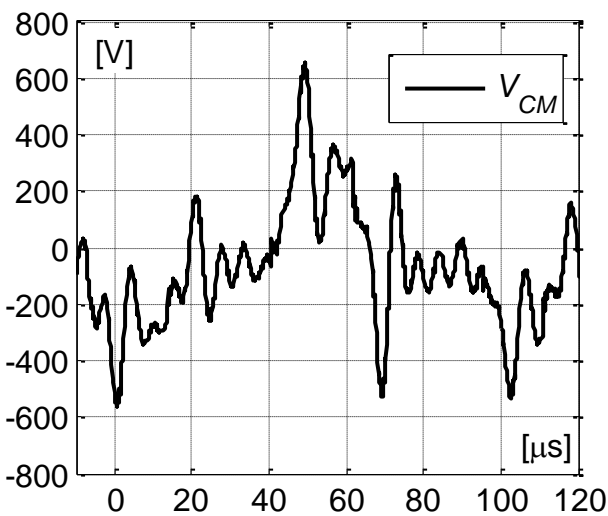
(a) Line to line voltage



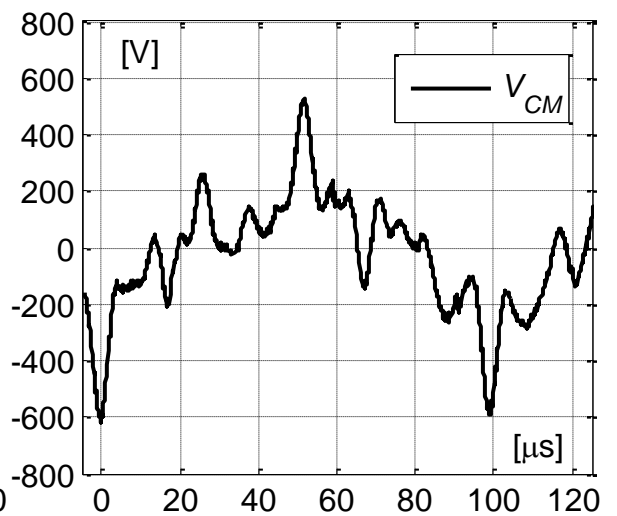
(b) Line to earth voltage



(b) Line to earth voltage



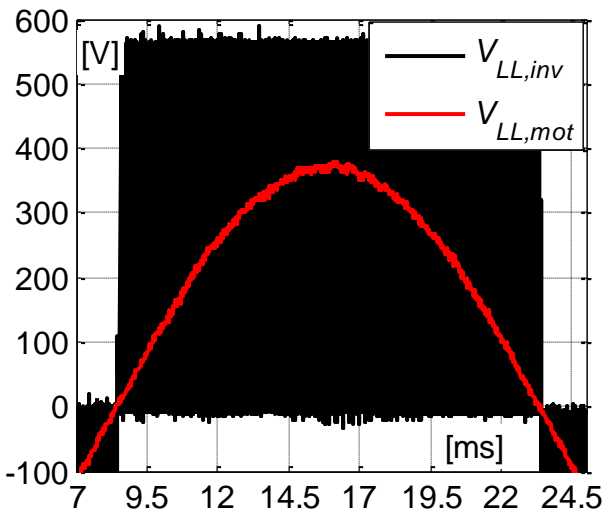
(c) Common mode voltage



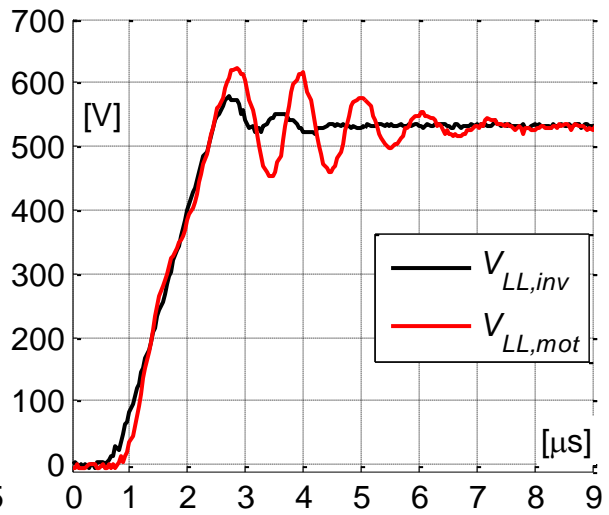
(c) Common mode voltage

Figure 19 HS inverter

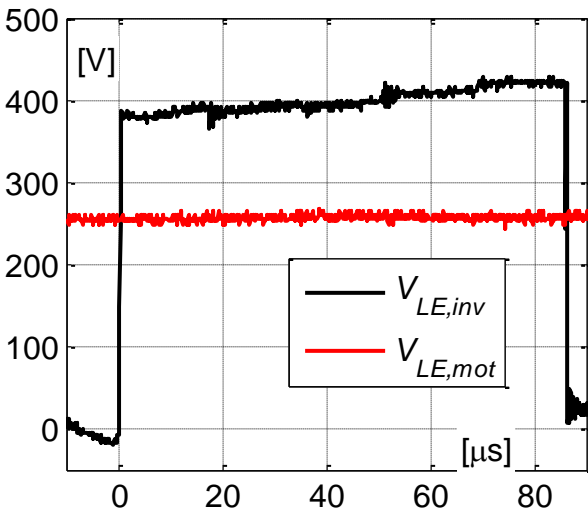
Figure 20 HS inverter with dv/dt filter



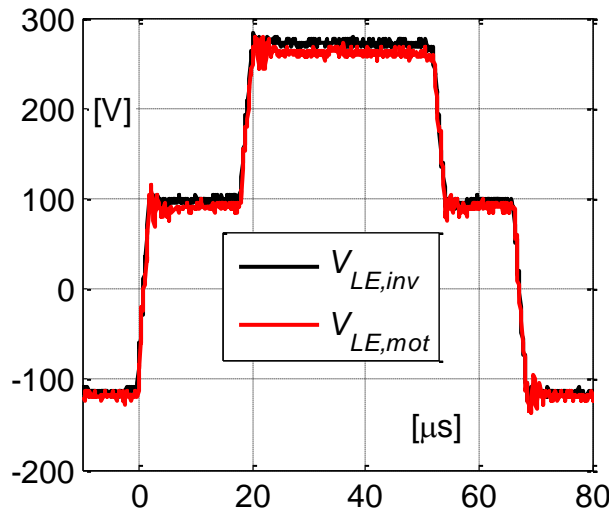
(a) Line to line voltage



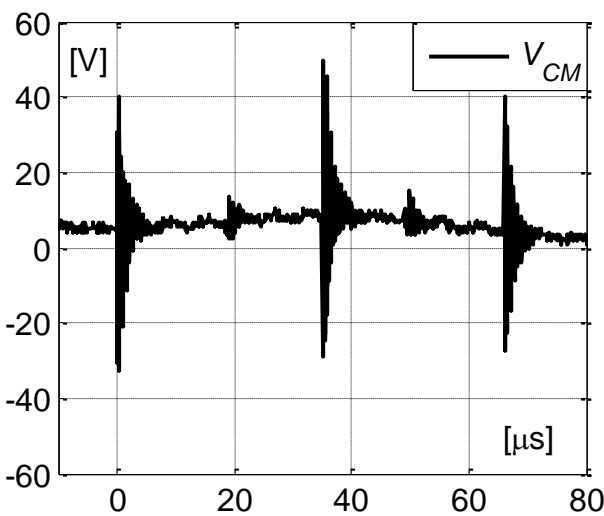
(a) Line to line voltage



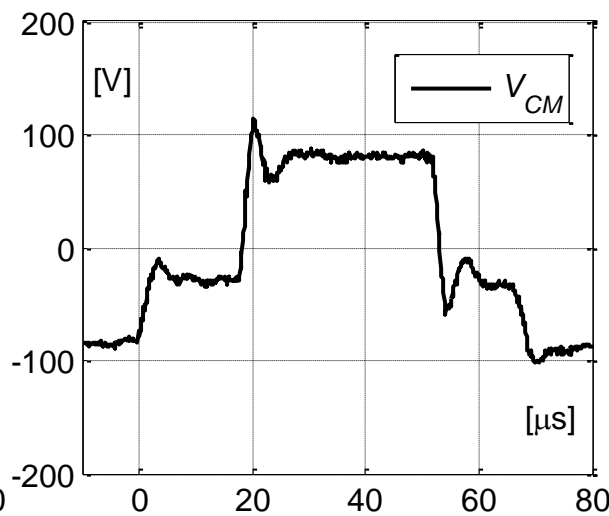
(b) Line to earth voltage



(b) Line to earth voltage



(c) Common mode voltage



(c) Common mode voltage

Figure 21: HS inverter with a Sine-wave EMC filter

Figure 22: SS Inverter

- **Hard switching inverter + Long cable + dv/dt filter** (Figure 20): The dv/dt filter increases the rise time of the line to line voltage and thereby voltage peaks at the motor are reduced. The frequency of the ringing oscillations is reduced. This filter has nearly no effect on the peak of common mode voltage.
- **Hard switching inverter + Long cable + Sine-wave EMC filter** (Figure 21): A near sinusoidal line to line voltage waveform can be observed at the motor side. Thus no high dv/dt , and voltage stress on the motor have been eliminated. The line to earth voltage at motor terminals is free of high frequencies. The CM voltage has smaller oscillations only during the PWM commutation. The ringing oscillations are completely eliminated.
- **Soft switching inverter + Long cable + No filter** (Figure 22): The soft switching inverter is designed for maximum voltage gradient of 600 V/ μ s. So the reduced dv/dt almost eliminates the ringing effect in the long cable. The reduced voltage reflections at the motor terminal can be observed. Due to the zero vector implementation within the resonant cycle, levels of the common mode voltage are limited to within ± 100 V. The slope of the common voltage is also reduced causing very low leakage currents.

The performance of the SS inverter is comparable to the HS inverter with a sine-wave EMC filter. For the HS inverter, the use of a filter increases the cost and weight of the power converters. The motor-friendly soft switching inverter does not need an output filter. So it has good dynamics compare to the hard switching inverter with a sine-wave EMC output filter.

1.5.3. Efficiency measurements

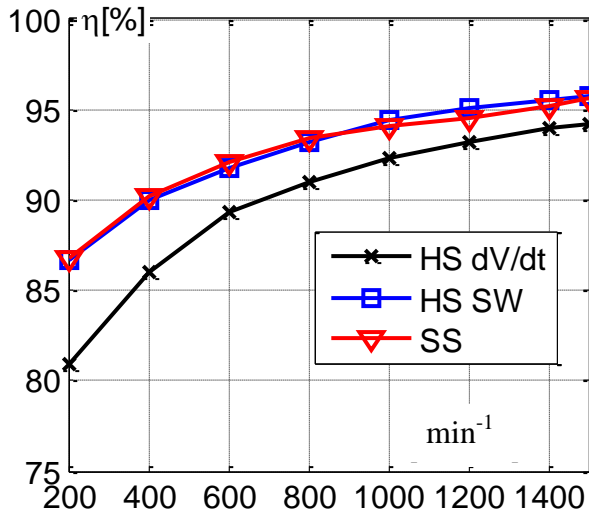
The efficiency measurements are taken for the hard switching inverter with filters and for the soft switching inverter without filters. The efficiency for a fixed speed and a fixed load torque is measured by a power meter NORMA 5000. The speed of the induction machine is kept constant by indirect field oriented control (IFOC) implemented in FPGA. Then the load torque is controlled by controlling the armature current of the DC generator. The efficiency measurements are presented for different speed and load torques. The following notations are used in Figure 23 and Figure 24:

- HS dv/dt : Hard switching inverter with a dv/dt filter and using a 34m long cable.
- HS SW: Hard switching inverter with a sine-wave EMC filter and using 34m long cable.
- SS: Soft switching inverter with no output filter and using a 34m long cable.

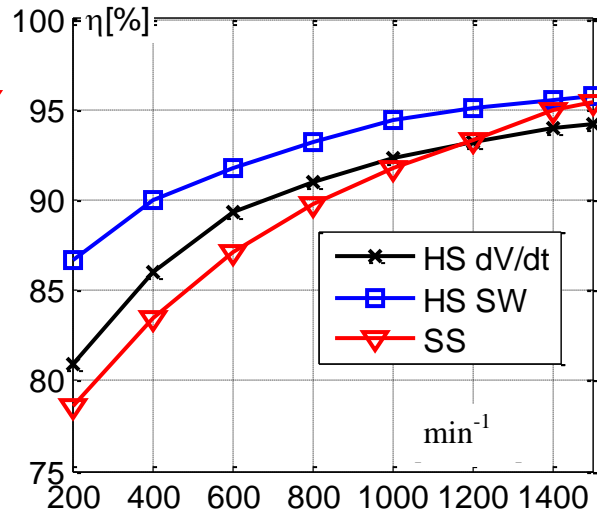
SS inverter for dv/dt reduction only: Here, the SS inverter operates only for the dv/dt reduction i.e. the zero vector is not implemented within a resonant cycle. Figure 23 shows the efficiency of a SS inverter, HS inverter with dv/dt filter and sine-wave EMC filter. The results indicate that SS inverter has higher efficiency when compare to HS inverter with a dv/dt filter.

SS inverter for dv/dt and CM voltage reduction: Here, the SS inverter reduces the dv/dt and also CM voltage level. So, the extended resonant cycle discussed in section 1.2.3 for the CM voltage reduction is used. From Figure 24, it can be concluded that HS inverter with a sine-wave EMC filter has higher efficiency compare to SS inverter. The difference in the efficiencies is very small at higher modulation indexes, i.e. at higher output power. With the decrease in the speed, the efficiency of SS inverter is decreasing rapidly.

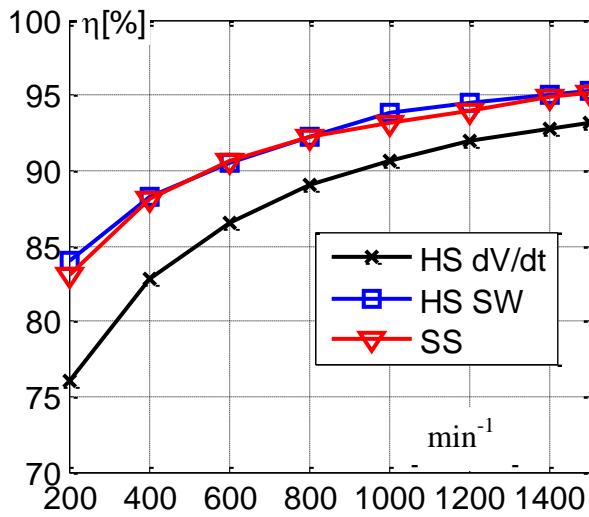
For a motor-friendly characteristic, the zero vector time is included in the resonant cycle. However, it is reducing the efficient characteristic of the SS inverter. In SS inverter, the zero voltage period of time is extended and the inductor current free wheels through a diode and inverter switches. The freewheeling inductor current is gradually reduced by the voltage drops of line resistance, diode and inverter switches. The considerable part of stored energy in the inductor is wasted as conduction losses. So the level of the trip current is increased otherwise the inverter input voltage will not reach the DC-link source voltage.



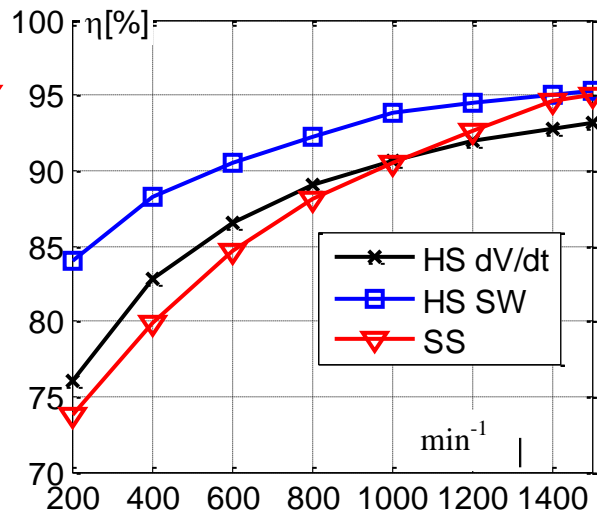
(a) Efficiency plot (T = 20 Nm)



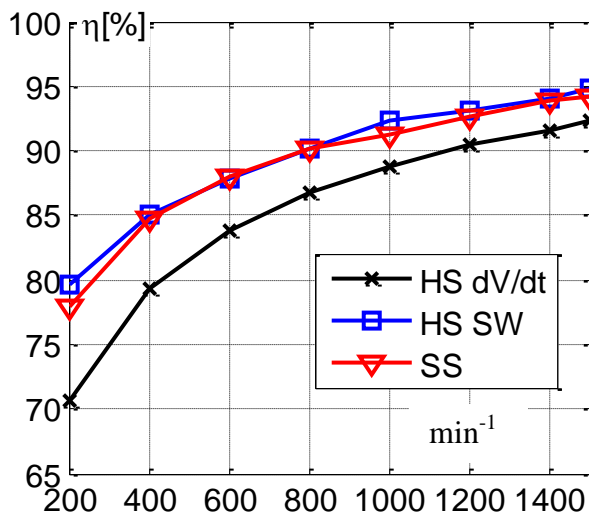
(a) Efficiency plot (T = 20 Nm)



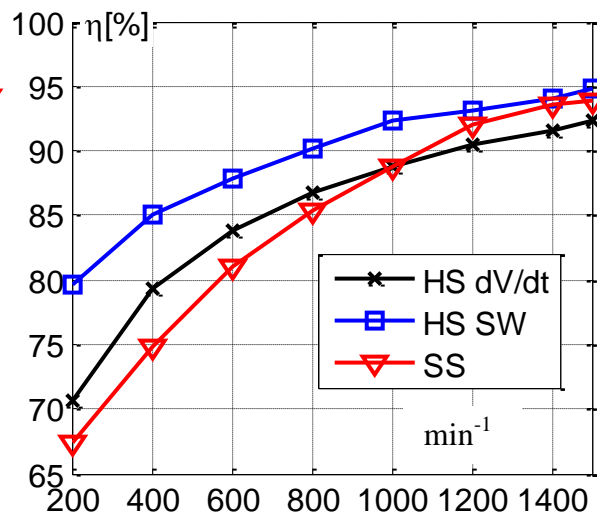
(b) Efficiency plot (T = 15 Nm)



(b) Efficiency plot (T = 15 Nm)



(c) Efficiency plot (T = 10 Nm)



(c) Efficiency plot (T = 10 Nm)

Figure 23 Efficiency comparison
(Soft switching inverter reducing only *dv/dt*)

Figure 24 Efficiency comparison
(Soft switching inverter reducing *dv/dt* and CMV)

The increase in a trip current and freewheeling inductor current produces substantial losses in the inverter. For low modulation index, a longer zero voltage period is needed. The losses during the freewheeling period are very high and the efficiency of the inverter is reduced to a low value. In Figure 23, the SS inverter efficiency is equal to of the HS inverter with a sine-wave EMC filter. In Figure 24, the SS inverter efficiency is less than that of the HS inverter with a sine-wave EMC filter. Here, the resonant cycles with longer zero voltage duration are producing high losses in the SS inverter. In order to improve the efficiency of the inverter, a SS inverter with a loss less variable zero voltage duration is required. Then the SS inverter will have same efficiency as the HS inverter with a sine-wave EMC filter.

1.5.4. A Novel Quasi-resonant DC-Link Inverter with Lossless Variable Zero Voltage Duration

A novel quasi-resonant DC-link inverter with lossless variable zero voltage duration (T3) is introduced in this subsection and is shown in Figure 25. If the switch S_{r2} is closed forever, then the topology T3 works in a similar way of topology T2. So for the given resonant circuit elements and inverter input currents, the required trip currents are equal in both the topologies T2 and T3. The converter is designed to achieve the voltage gradient of $600\text{V}/\mu\text{s}$ intended for low over voltage at the end of a 34m motor cable. For the given specifications, the selected parameters are same as topology T2 and are as follows: Resonant Inductor $L_r = 30\mu\text{H}$, resonant capacitor $C_r = 0.47\ \mu\text{F}$ and capacitor $C = 0.141\ \mu\text{F}$.

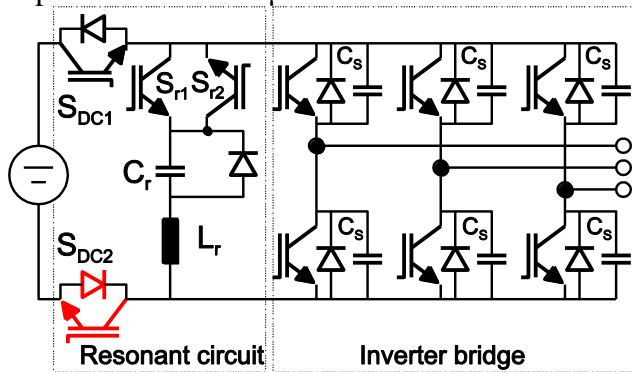


Figure 25 A novel QRDCL inverter

In Figure 26, simulated waveforms for resonant circuit are shown. In this case, the switch S_{r2} is closed with no delay. Then the resonant circuit works in similar fashion as of topology T2 and the waveforms are akin to the presented in Figure 18a. The resonant waveforms for extended resonant cycle are shown in Figure 27. During zero voltage period, the resonant capacitor voltage charged to its peak value and remained at this charge until the switch S_{r2} is turned on.

At the same time, the inductor current i_L is zero. This zero voltage period is controllable and continues until the switch S_{r2} is turned on. Because the current i_L is zero, no current is freewheeling through the inverter devices. So a lossless variable zero voltage duration can be achieved by the proposed resonant converter. For given operating conditions, average value of the inductor current is less in topology T3 compared to topology T2.

Figure 28 shows the waveforms of a line to line voltage at the inverter and motor terminals for maximum load current. The overvoltage at motor terminals remains under 17% when using a 34m long cable. The common mode voltage waveform is given in Figure 29. The slope and level of the common mode voltage is reduced. The efficiency is estimated for both the topologies and the efficiency plots are shown in Figure 30 and Figure 31. At low speeds, the efficiency of topology T3 is higher compare to topology T2. This can be attributed to the reduction of conduction losses during a resonant cycle's long zero voltage period. At higher speeds, the efficiency of topology T3 is same as topology T2. Here, a resonant cycle's zero voltage period is small and topology T3 works in a similar way of topology T2. So it can be concluded that the proposed QRDCL inverter helps in reducing the losses under low modulation index.

1.6. Conclusions

The soft switching inverter is designed to be a motor friendly. In this project, the reduction of high frequency parasitic effects is tested. For the same application, the hard switching inverter together with the filter can be opted. But it increases the size, weight and cost of the inverter. The efficiency of the QRDCL inverter is measured. The efficiency of a hard switching inverter with filters is also measured for comparison.

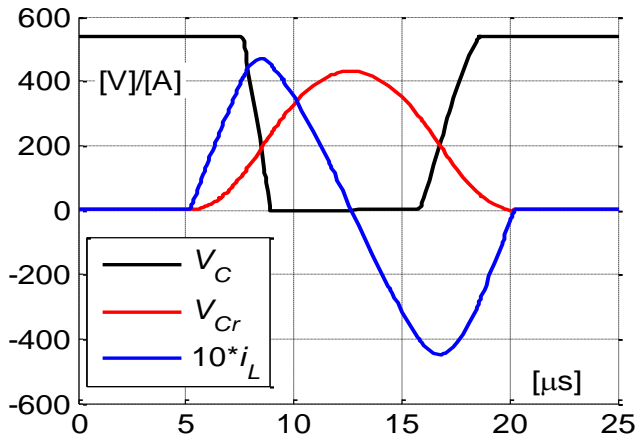


Figure 26: Simulated resonant circuit waveforms

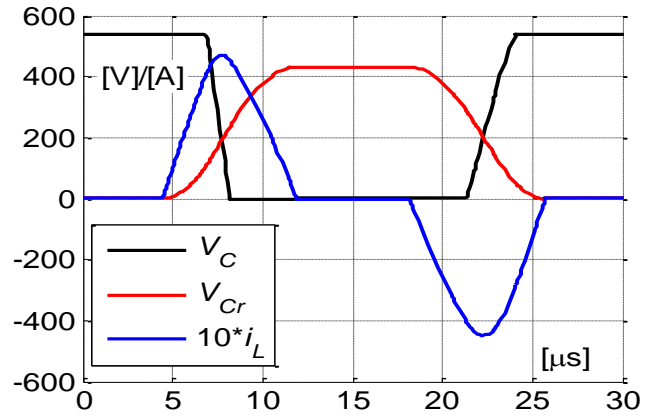


Figure 27: Simulated waveforms for extended zero voltage period

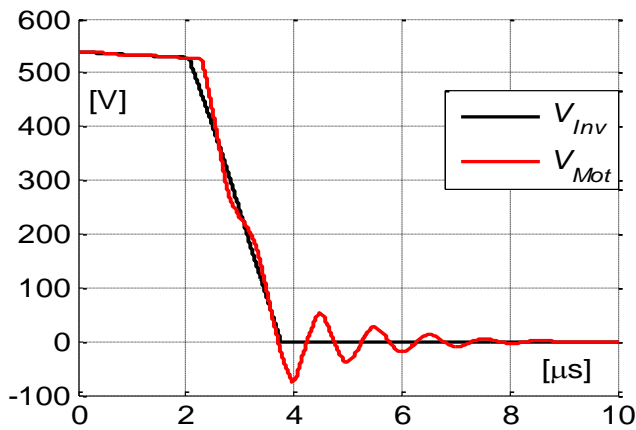


Figure 28: Simulated over voltage reflections

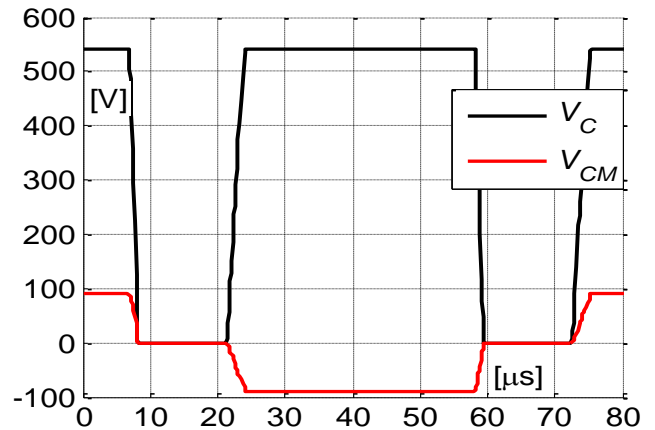


Figure 29: Simulated common mode voltage

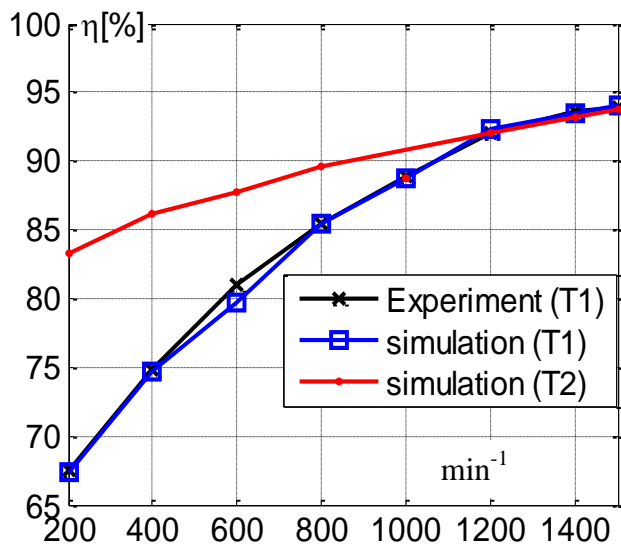


Figure 30: Efficiency plot (Torque = 10 Nm)

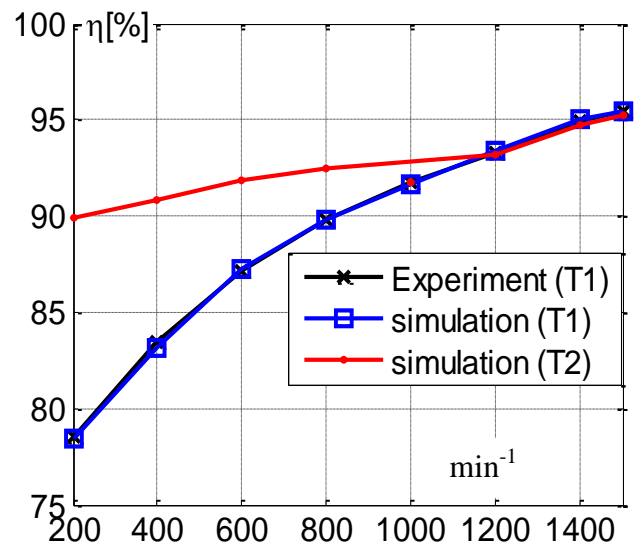


Figure 31: Efficiency plot (Torque = 20 Nm)

Table I gives a comparative overview of the evaluated motor-friendly hard and soft switching inverters. The efficiency of a QRDCL converter can be improved further by use of new semiconductor technology optimised for low switching and conduction losses. In summary, the comparative study based on experimental results suggests that motor-friendly SS inverter is an alternative to HS inverter with a sine-wave EMC output filter.

Table I: Motor-friendly hard and soft switching inverters

Hard switching inverter with dv/dt output filter	Soft switching inverter for dv/dt reduction	Hard switching inverter with sine - wave EMC output filter	Soft switching inverter for dv/dt and CM voltage reduction
Advantages (+) / Disadvantages (–)			
+ No modification in the HS inverter control – increase in cost, size and weight – Lower efficiency	+ Small size and cost effective + Higher efficiency – Addition of the resonant circuit control	+ Sinusoidal output voltage and line to earth voltage + Higher efficiency – Expensive, heavy and bulky – Additional sensors for a short circuit detection – Filter time constant to be taken in the HS inverter control. Reduction in the control dynamic.	+ No output filters are required. Good dynamic characteristic. + Small size and cost effective + High efficiency is possible with loss less variable zero voltage period – Addition of the resonant circuit control and modified modulation – Low efficiency due to losses in the extended zero voltage period
Application			
Over voltage reduction	Over voltage reduction	Over voltage, CM voltage reduction	Over voltage and CM voltage level reduction

1.7. References

- [1] E. Persson, “Transient effects in application of PWM inverters to induction motors,” *IEEE Transactions on Industry Applications*, vol. 28, pp. 1095-1101, 1992.
- [2] A. Von Jouanne, P. Enjeti and W. Gray, “Application issues for PWM adjustable speed AC motor drives,” *IEEE Industrial Applications Magazine*, vol. 2, Issue 5, pp. 10-18, Sep/Oct 1996.
- [3] N. Hanigovszki, J. Landkildehus and F. Blaabjerg, “Output filters for AC adjustable speed drives,” in *Proc. Applied Power Electronics Conference*, 2007, pp. 236-242.
- [4] S. Melly, “New output filter concept for power drive systems,” *Application notes*, Schaffner EMC Inc., Internet: <http://www.schaffner.com/mediapool/files/mediaPool49.pdf>, Aug. 2002.
- [5] “Output filters design guide,” *Application notes*, Danfoss, 2010.
- [6] A. Muetze and A. Binder, “Don’t lose your bearings—Mitigation techniques for bearing currents in inverter-supplied drive systems,” *IEEE Ind. Appl. Mag.*, vol. 12, no. 4, pp. 22–31, Jul./Aug. 2006.
- [7] C. Choochuan, “A survey of output filter topologies to minimize the impact of PWM inverter waveforms on three-phase AC induction motors,” in *Proc. 7th IPEC*, Nov. 29–Dec. 2, 2005, pp. 1–6.
- [8] A. F. Moreira, T. A. Lipo, G. Venkataramanan, and S. Bernet, “High-frequency modeling for cable and induction motor overvoltage studies in long cable drives,” *IEEE Transactions on Industry Applications*, vol. 38, pp. 1297-1306, 2002.
- [9] A. M. Hava and E. Un, “Performance analysis of reduced common-mode voltage PWM methods and comparison with standard PWM methods for three-phase voltage-source inverters,” *IEEE Trans. Power Electron.*, vol. 24, no. 1, pp. 241–252, Jan. 2009.
- [10] G. Bachmann and P. Mutschler, “Comparison of soft switched IGBT converters,” in *Proc. Power conversion and intelligent motion conference (PCIM)*, 1999, pp. 469-474.
- [11] D.M. Divan, “The Resonant DC Link Converter - A New Concept in Static Power Conversion,” in *Proc. IEEE-IAS Conf. Rec.*, 1986, pp. 648-656.
- [12] D.M. Divan and G. Skibinski, “Zero Switching Loss Inverters for High Power Applications,” in *Proc. IEEE-IAS Conf. Rec.*, 1987, pp. 627-634.

- [13] J. He, N. Mohan and B. Wold, “Zero voltage switching PWM inverter for high frequency DC-AC power conversion,” *IEEE Transactions on Industrial Applications*, vol. 29, pp. 959-968, Sep/Oct. 1993.
- [14] J.G. Cho, H.S. Kim, and G.H. Cho, “Novel soft switching PWM converter using a new parallel resonant dc-link,” in *Proc. IEEE PESC*, 1991, pp. 241-247.
- [15] Q. Li, J. Wu, and H. Jiang, “Design of parallel resonant dc-link soft switching inverter based on DSP,” in *proc. World Congress on Intelligent Control and Automation*, 2004, pp. 5595-5599.
- [16] Z. Y. Pan, and F. L. Luo, “Transformer based resonant dc-link inverter for brushless DC motor drive system,” *IEEE Trans. on Power Electron.*, vol. 20, No. 4, pp. 939-947, Jul. 2005.
- [17] H. Hucheng, D. Jingyi, C. Xiaosheng, and L. Weiguo, “Three-phase soft-switching PWM inverter for brushless DC motor,” in *proc. IEEE Industrial Electronics and Applications*, pp. 3362-3365, May 2009.
- [18] A. Sikorski and T. Citko, “Quasi-Resonant Parallel DC Link Circuit for High-Frequency DC-AC Inverters,” in *Proc. EPE*, 1993, pp. 174-177.
- [19] L. Malesani, P. Tenti, P. Tomasin and V. Toigo, “High efficiency quasi-resonant DC link three-phase power inverter for full-range PWM,” *IEEE Transactions on Industry Applications*, vol. 31, pp. 141-148, Jan/Feb 1995.
- [20] J.W. Choi and S.K. Sul, “Resonant link bidirectional power converter: Part I-Resonant circuit,” *IEEE Transactions on Power Electronics*, vol. 10, pp. 479-484, Jul 1995.
- [21] J. He and N. Mohan, “Parallel Resonant DC Link Circuit – A Novel Zero Switching Loss Topology with Minimum Voltage Stresses,” *IEEE Trans. Power Electron.*, vol. 6, no. 4, pp. 687- 694, Oct. 1991.
- [22] S. Munk-Nielsen, L.N. Tutelea and U. Jaeger, “Simulation with ideal switch models combined with measured loss data provides a good estimate of power loss,” in *Proc. IEEE Industry Applications Conference*, 2000, pp. 2915-2922.
- [23] C. Purcarea, J. Kedariseti and P. Mutschler, “A Motor Friendly and Efficient Resonant DC-link Converter,” in *Proc. 13th European Conference on Power Electronics and Applications (EPE)*, 2009, pp. 1-10.

6.5. Subproject 5: Multi-scale modelling and extraction of parameters in the simulation of inverter-fed drives

M.Sc. Zarife Cay

Dipl.-Wirtsch.-Ing. Frank Denz

Prof. Dr. –Ing. Thomas Weiland

Institut für Theorie Elektromagnetischer Felder, TU Darmstadt

E-Mail: denz@temf.tu-darmstadt.de

1. Work schedule and methods

Length (months)	Contents	Status
4	<ul style="list-style-type: none"> • Numerical model of a stator slot • Calculation of the capacitance matrix in the linear case • Variation of the electrical properties of the insulation material • Comparison with experimental data (with <i>TP3-Hinrichsen</i>) 	<input checked="" type="checkbox"/> <input checked="" type="checkbox"/> <input checked="" type="checkbox"/> <input checked="" type="checkbox"/>
4	<ul style="list-style-type: none"> • Extension of the calculation method to the non-linear case • Non-linear electro-quasistatics model for thin insulation layers • Investigation of the influence of non-linear material coatings on the capacitive coupling of motor windings • Comparison with experimental data (with <i>TP3-Hinrichsen</i>) 	<input checked="" type="checkbox"/> <input checked="" type="checkbox"/> <input checked="" type="checkbox"/> <input checked="" type="checkbox"/>
8	<ul style="list-style-type: none"> • Compilation of a capacitance database for a set of reference windings • Calculation of non-linear capacitance matrices for windings and/or stator slots with microvaristor material coatings • Magneto-quasistatics calculations and extraction of admittance and impedance matrices • Investigation of wave propagation effects using a multiconductor transmission line model (in collaboration with <i>TP2-Gjonaj</i>) 	<input checked="" type="checkbox"/> <input checked="" type="checkbox"/> <input checked="" type="checkbox"/> <input checked="" type="checkbox"/>

6	<ul style="list-style-type: none"> Development of a detailed winding model to be embedded into a reduced order transmission line model (in collaboration with <i>TP2-Gjonaj</i>) or into a Finite-Element model of a motor (in collaboration with <i>de Gersem</i> and <i>TP1-Binder</i>) 	☒
4	<ul style="list-style-type: none"> Implementation of the winding model into a multi-scale time domain simulation Comparison with experimental data for an open-ended conductor winding (in collaboration with <i>TP3-Hinrichsen</i>). 	☒ ☒ .
6	<ul style="list-style-type: none"> Application of multi-scale windings simulations for <ul style="list-style-type: none"> Transmission line models (with <i>TP2-Gjonaj</i>) Finite-Element model of an induction motor (with <i>de Gersem</i>), Comparison with experimental data for realistic motor windings (with <i>TP3-Hinrichsen</i> and <i>TP1-Binder</i>) 	☒ ☒
4	<ul style="list-style-type: none"> Comparison of the new approach with conventional simulation methods Preparation of the final report Preparation of the PhD thesis (ongoing) 	☑ ☑ ☑

2. Summary

The subproject deals with the characterization of the nonlinear machine components as well as with the transition from field simulations to equivalent network models. The nonlinearity of microvaristor filled insulator shieldings is analyzed in terms of their field depended permittivity and electrical conductivity. Emphasis is given to the development of an appropriate model for the non-linear hysteresis-like behavior of these materials. Another goal of the project which was pursued in the project is the derivation of nonlinear capacitances and conductances from numerical field simulations. The widely used approach used for this purpose is based on the linear superposition principle. This, however, does not apply in the highly nonlinear case of microvaristor insulation. We develop a method for extracting nonlinear equivalent network models from transient electro-quasistatics simulations. These models are, then, integrated in the full transient simulation of electric drives in order to quantify the propagation of higher frequency parasitic currents in inverter-fed induction machines.

3. Calculation of the capacitance matrix of a stator slot

The entries of the capacitance matrix corresponding to a simplified stator slot (see Fig. 1 (left)) were computed using several numerical programs for solving electrostatic problems. In addition, these results were compared with analytical estimates. The used programs were CST EM Studio, Olympos and Symplegades (see Fig. 2). The meshes used by Symplegades were generated either by CST EM Studio or Olympos. First, each of the turns is individually set to a potential of one Volt (i.e., $U_m = 1 \text{ V}$ for turn m), while the others are kept at 0 V. The energy W_{mm} stored inside the resulting field distribution was calculated. Due to

$$W_{mm} = \frac{1}{2} C_{mm} U_m^2, \quad (1)$$

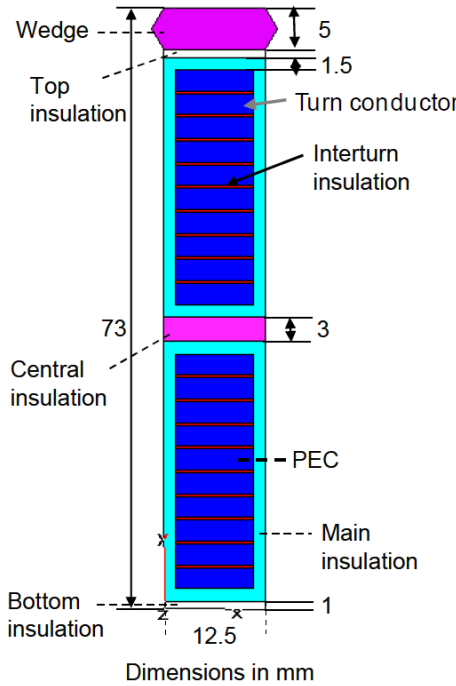
the entrance of the capacitance matrix C_{mm} is simply $C_{mm} = 2 W_{elec}$. Then, the off-diagonal entries C_{mn} are obtained when the potential of stator turns m and n is set to 1 V and all to zero Volt:

$$C_{mn} = \frac{1}{2} C_{mm} + \frac{1}{2} C_{nn} - \frac{W_{mn}}{U_m^2}, \quad (2)$$

Finally, different parameters related to the geometry were deduced from the obtained capacitance matrix. Fig. 3 (right) shows the obtained values. All the used programs provide results which agree relatively well. Rough analytical estimates of parameters a, b and c deliver values of 107 pF/m, 841 pF/m and 107 pF/m, respectively.

Table 1 Specifications of used electromagnetic simulation software.

	CST EM Studio	Symplegades	Olympos
Numerical method	3D FIT	2D FEM	2D FEM
Solver equation	Electrostatic	Electrostatic	Electrostatic
Mesh type	Hexahedral	Tetrahedral	Tetrahedral
Adaptive mesh refinement	Yes	–	Yes
Number of mesh cells	≈ 265.000	≈ 72.000 (CST projected) ≈ 75.000 (Olympos)	≈ 200.000



	CST EM Studio	Symplegades		Olympos	
		CST mesh	Olympos mesh		
a	211	213	212	211	capacitance between the conductor of the first turn and ground
b	879	885	881	880	capacitance between the two adjacent turns
c	119	117	119	118	capacitance between the intermediate-turn conductor and ground
d	194	190	194	194	capacitance between the conductor of the 10th or 11th turn and ground
e	261	257	262	261	capacitance between the conductor of the last turn and ground
f	40.7	40.8	40.8	40.8	capacitance between the conductor of the 10th and the 11th turn conductor

Figure 1 CST EM Studio model of a stator slot (left) and some capacitances per unit length (in pF/m) of the stator slot computed with different electrostatic solvers (right).

4. Verification of nonlinear electroquasistatics in symplegades

Symplegades is a 2D finite element program capable of solving electroquasistatics problems in time domain with nonlinear electric conductivity σ . The electroquasistatics equation can be written:

$$\nabla \cdot (\sigma(|\vec{E}|) \nabla \Phi) + \nabla \cdot \left(\frac{d}{dt} (\epsilon \nabla \Phi) \right) = 0 \tag{3}$$

with nonlinear, field-strength dependent electric conductivity $\sigma(|\vec{E}|)$, permittivity ϵ and scalar electric potential Φ . The correctness of the software with respect to the nonlinear conductivity was verified for a simple geometry with known analytical solution. The geometry is simply a plate capacitor, but conductivity depended on potential/field strength. In Fig. 2 the analytical results can be compared with the results from Symplegades and a simple MatLab™ code.

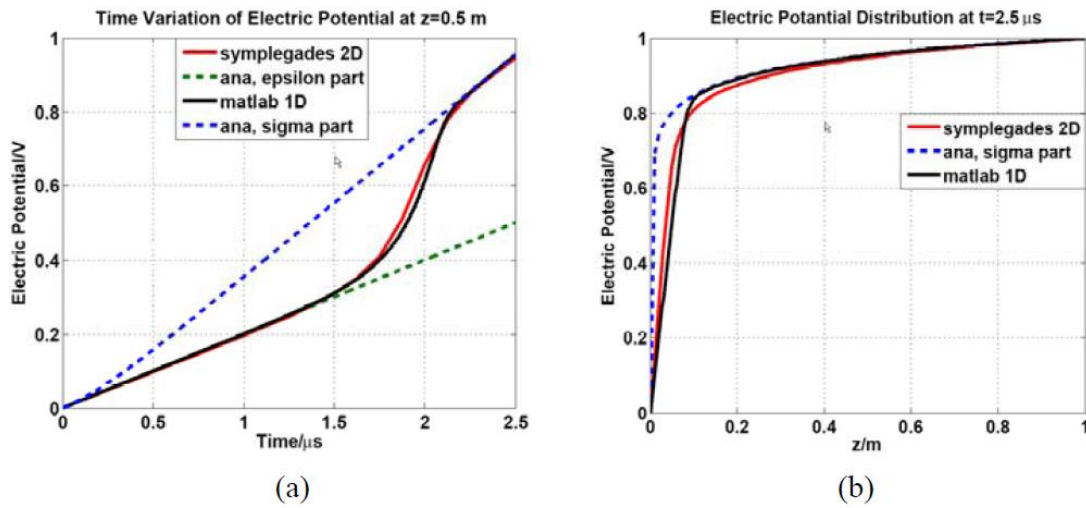


Figure 2 (a) Evolution in time of the electric potential between electrodes; (b) Electric potential on line connecting the two electrodes at $t=2.5 \mu s$.

5. Numerical simulation of a stator slot with field grading

The stator slot from above was simulated numerically with different insulation materials for the interturn insulation:

- an ordinary insulation material with relative permittivity $\epsilon_r = 3$,
- an insulation material with high relative permittivity $\epsilon_r = 18$,
- a microvaristor material.

The first turn of the stator slot is excited by a transient voltage, while all other turns are set to zero Volt. The effects of choosing a material with higher permittivity or with nonlinear conductivity can be seen in Fig. 3. In the case of the microvaristor material the maximum voltage stress is reduced by about 20 % with respect to the ordinary, low-permittivity material.

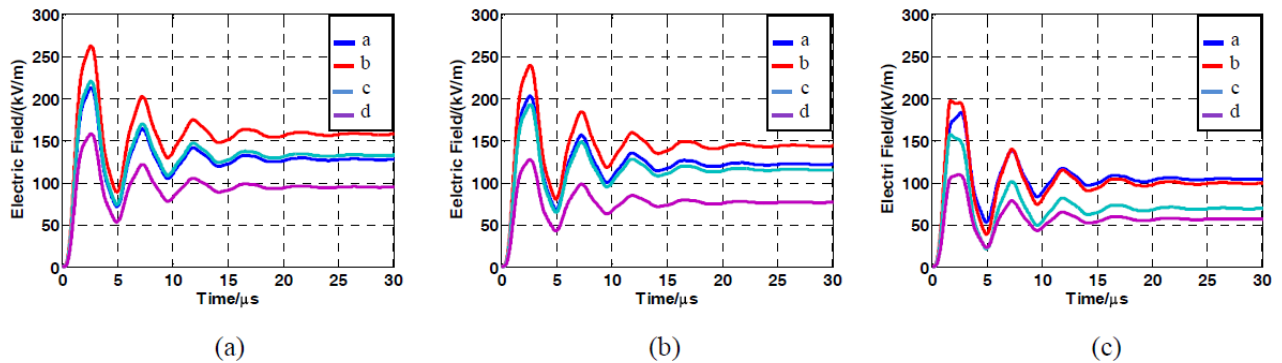


Figure 3 Magnitude of the electric field at the space monitors for the slot with (a) ordinary insulation material, (b) high-permittivity insulation material, and (c) microvaristor-filled interturn insulation.

6. Extraction of the material parameters of microvaristor-filled insulations

In the course of Subproject 3 measurements with microvaristor-filled silicone rubber had been realized. The measurement data should provide the material characteristics required for subsequent field simulations. However, the observed voltage and current signals indicated that it was impossible to explain the behavior of the material by a nonlinear, field-strength dependent electric conductivity $\sigma(|\vec{E}|)$ and constant relative permittivity ϵ_r . Dipl.-Ing. Sébastien Blatt suggested that relative permittivity might also depend on relative permittivity and offered his measurement data.

To obtain the material characteristics $\sigma(|\vec{E}|)$ and $\varepsilon_r(|\vec{E}|)$, a parameter extraction method was devised, which, to our knowledge, had not been used before. The approach presented at [1] or [2] is comparable to an approach that was applied by *Bitterlich* and others in the area of hydrodynamics ([3], [4],[5], [6]). The method is based on a least-square estimate and inspired by the finite element method. The estimation process consists of the following steps:

- Obtain current densities $J(t_i)$ and field strengths $E(t_i)$ from geometry, measured currents $I(t_i)$ and voltages $U(t_i)$ at discrete moments t_i .
- Calculation of a smooth $\dot{E}(t_i)$ and possibly reduction of the quantity of data.
- Assembly and solution of an over-determined linear system $\mathbf{A} x = b$ using chosen basis functions.
- Translation of vector x to material characteristics $\sigma(|\vec{E}|)$ and $\varepsilon_r(|\vec{E}|)$.

The first two steps need no further explanation. In the third step, it is assumed that the conductivity can be described in the following form:

$$\sigma(|E|) = \sum_i \tilde{\sigma}_i \varphi_i(|E|). \quad (4)$$

In this equation, the $\varphi_i(|E|)$ are bases functions, e.g., B-splines, and the $\tilde{\sigma}_i$ are yet unknown scalar values which characterize the conductivity. The same approach is used for $\varepsilon_r(|E|)$ with unknowns $\tilde{\varepsilon}_i$.

According to the continuity equation, the measured current density $J(t_i)$, has to be equal to the sum of resistive and displacement current density inside the material for the corresponding field strength values. Thus:

$$J(t_i) \cong \nabla \cdot (\sigma(|E(t_i)|) E(t_i)) + \nabla \cdot \left(\frac{d}{dt} (\varepsilon_r(|E(t_i)|) \varepsilon_0 E(t_i)) \right) \quad (5)$$

Inserting the expressions for conductivity and permittivity, one obtains a linear system of equation. Its number of rows corresponds with the number of time points t_i . The number of columns equals the user-defined number of unknowns $\tilde{\sigma}_i$ and $\tilde{\varepsilon}_i$. The vector on the right-hand side contains the currents $J(t_i)$. A resulting estimation of material characteristics is shown in Fig. 4.

This obtained material characteristic was used to calculate the currents, which should be observable for the measurement setup and the respective voltage signal, if these parameters were true. The estimated material characteristics were inserted in a MatLabTM code calculating the current given dimensions of the guard ring setup, material characteristics and voltage excitation signal. The measurement data consisted of 35 data sets with peak voltages ranging from 500 V to 9.000 V at 50 Hz. In Fig. 5 measured and simulated currents are for nine different peak voltages. One can see that measurement and simulation results agree quite well. Thus, the assumption of nonlinear conductivity $\sigma(|E(t_i)|)$ as well as permittivity $\varepsilon_r(|E(t_i)|)$ appears to be confirmed.

³ Measurements were done with a guard ring configuration to minimize the influence of stray field and obtain an almost homogeneous electric field.

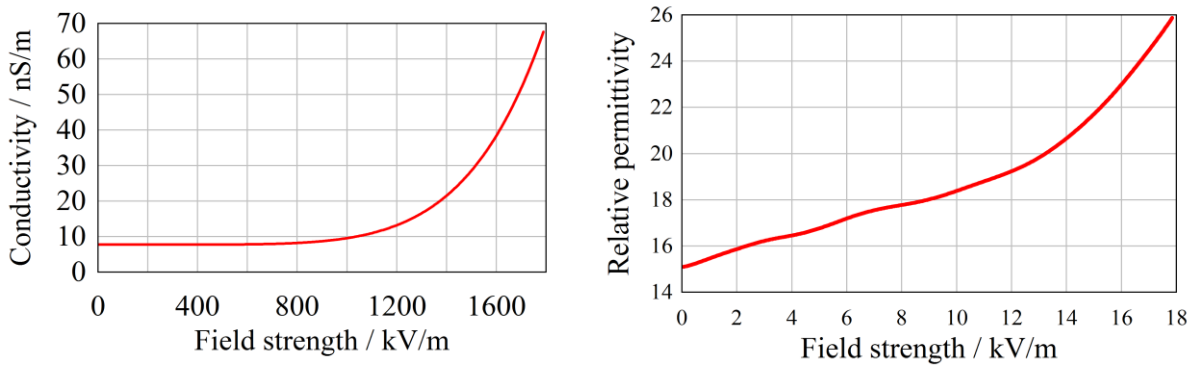


Figure 4 Electric conductivity (left) and relative permittivity (right) of microvaristor-filled silicone rubber estimated by procedure described above.

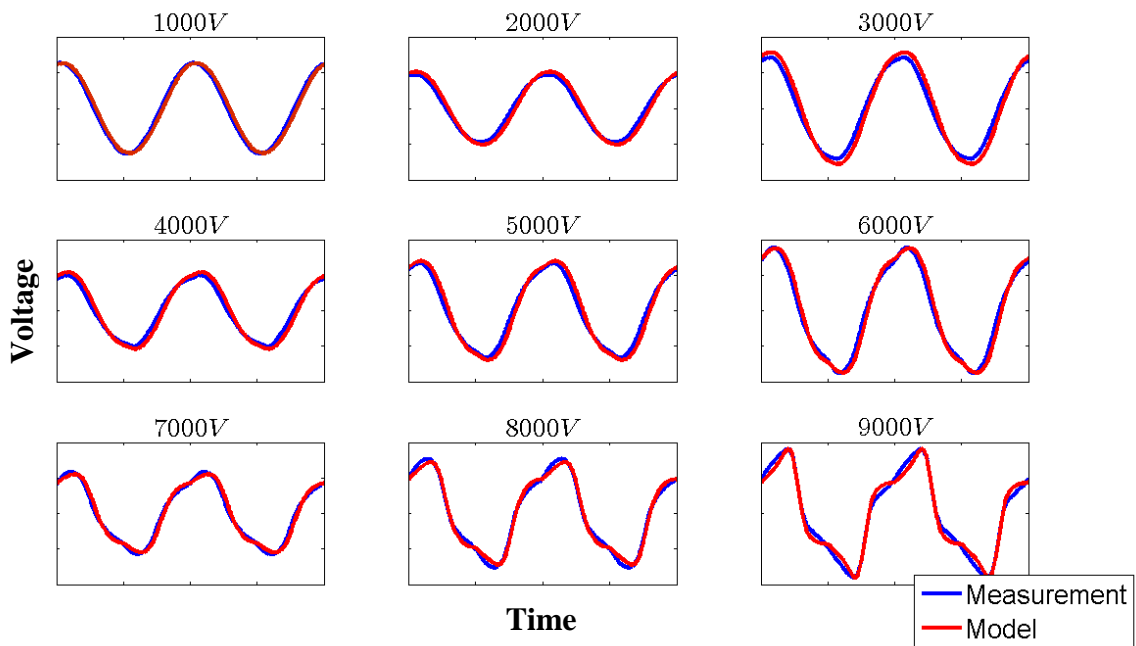


Figure 5 Comparison between two measured current and the current modeled with estimated material characteristics of Figure 4 for nine measurements with different peak voltage. Note that the vertical axis is scaled differently in each of the subplots.

Realizing that the residual error was not independent from peak voltage, the material characteristics were estimated for each of the 35 measurement data sets individually. This resulted in the characteristics of Fig. 6. One can see that the estimated conductivity at lower voltages increases continuously by up to a factor of four. The same tendency can be observed with respect to relative permittivity, although its increase is not much higher than 10%.

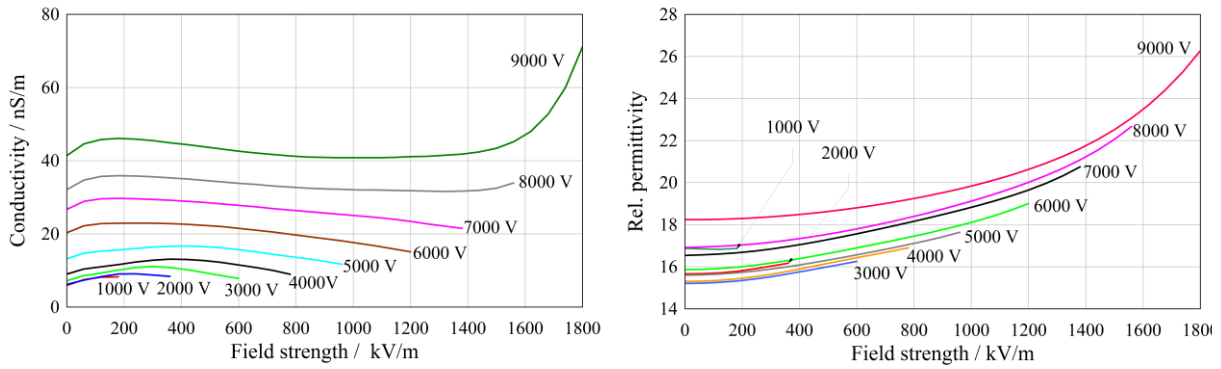


Figure 6 Polynomial estimates of conductivity (left) and relative permittivity (right) as functions of field strength derived from measurements with different peak voltages.

Fig. 7 shows the better agreement between measured and simulated currents, which cannot be discerned by looking at the plots. Conductivity and permittivity increase (almost) continuously for higher peak voltages. Therefore, the material properties do not only depend on momentary field strength, but also somehow on the peak voltage of the excitation signal. Thus, a hysteresis-like behavior is observed which needs to be addressed by a more detailed material model.

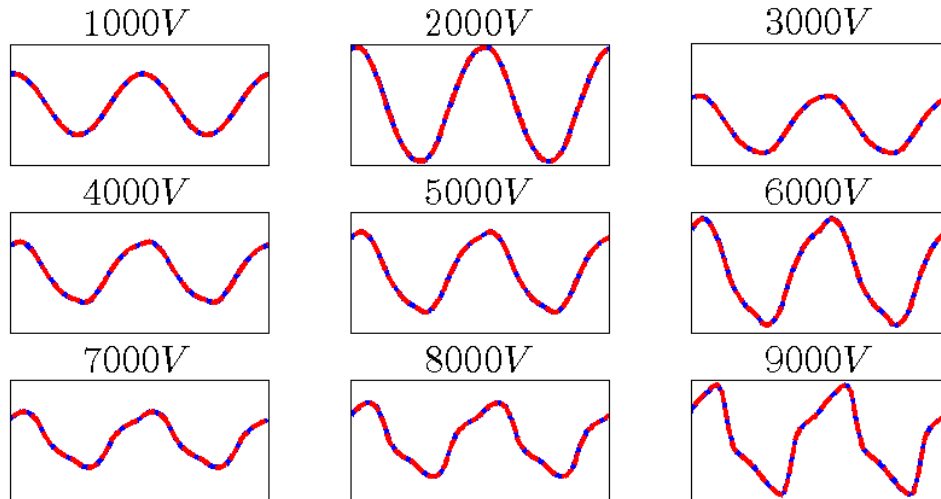


Figure 7 Comparison of transient measured (blue) and simulated (red) current for a 50 Hz signal with different peak voltages. The materials characteristics are piecewise-linear functions of field strength and differently chosen for each simulation of an equivalent network of parallel resistor and capacitance.

7. Relaxation models for the microvaristor material

In order to model the hysteresis effect in microvaristors, the relationship between fields and currents was extended to

$$J(t) \cong J_r(E(t)) + \frac{d}{dt}D(E(t)) + \underbrace{J_r^{rel}(E(0, \dots, t)) + J_d^{rel}(E(0, \dots, t))}_{\text{relaxation terms}} \tag{5}$$

Another question was, whether the material parameters change with some delay, e.g.:

$$\epsilon_r^{rel}(t) = \int_0^\infty \tilde{\epsilon}_r^{rel}(|E(t - \tau)|) \cdot e^{-\frac{\tau}{\tau_\epsilon}} d\tau, \tag{6}$$

with unknown field-strength dependent function $\tilde{\epsilon}_r^{rel}$ and relaxation time constant τ_ϵ , or if the current itself obeys a relaxation law:

$$J_d^{rel}(t) = \int_0^\infty \tilde{J}_d^{rel}(|E(t-\tau)|) \cdot e^{-\frac{\tau}{\tau_\epsilon}} d\tau. \quad (7)$$

For each of these approaches the minimum difference between measured and calculated currents was sought by a nonlinear minimization procedure. In Figure the results for some of the approaches are shown. Although the error between measured and calculated currents decreased in all those approaches – c), d) e) and f) – with respect to case b), which assumes a single nonlinear material characteristic without relaxation, the error remains significantly larger than in case a), characterized by different characteristics for different peak voltages. The confidence in the validity of a specific model and of the estimated parameters remains very limited. The question about the relaxation mechanism remains yet to be answered.

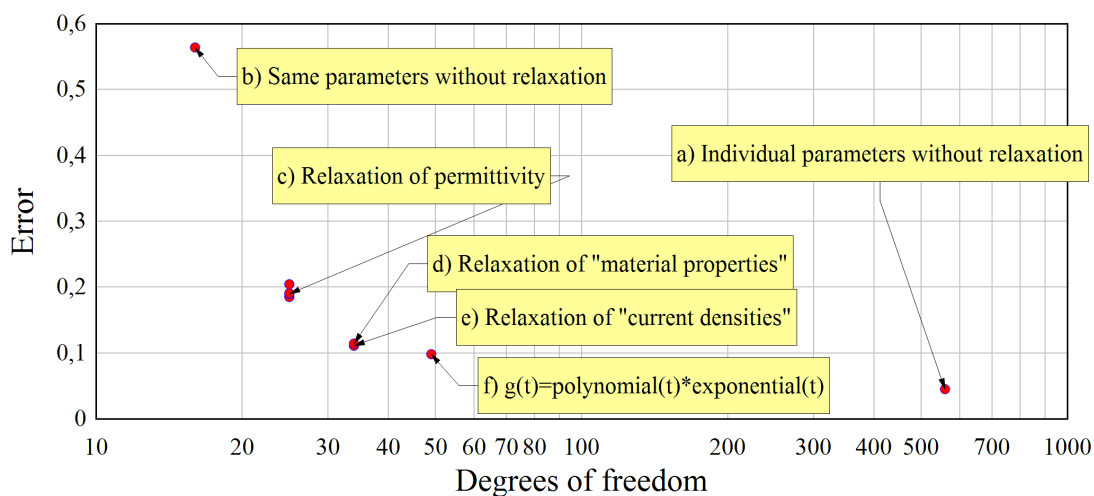


Figure 8 Quality of the estimate for different approaches. The difference between measured and observed current is much smaller for case a) when the parameters are chosen differently for each measurement than in case b) with the same material characteristic for all measurements. A large part of the difference may be attributed to relaxation. Several relaxation models show a much smaller error relative to case b), though not attaining the level of case b).

8. Nonlinear capacitance models

The capacitance extraction approach becomes problematic when permittivity is nonlinear, as shown for the microvaristor-filled silicone rubber, which might be used for nonlinear field control [8]. In that case, the capacitance between two conductors (e.g., turns of a stator) becomes a function of the voltage difference between them – and possibly of the potentials of neighboring conductors, too. For a stator slot model the value of one entry of the capacitance matrix was calculated based on the above-mentioned method and the energy of the electric field. The results are listed in Table 2. There is no single capacitance value, but the capacitance depends on voltage. Furthermore, one has to distinguish between “average” (i.e., Q/U) and “differential” capacitance (dQ/dU).

If this energy based method is to be used, one also has to define an appropriate working point, which is probably different from setting the potential of all other conductors to zero. Unless one operates closely to this working point, i.e. signal variations are small, errors may be important.

Table 2 Average and differential coupling capacitance between two conductors with nonlinear insulation.

U / V	$C_{6,5}^{\text{mean}}$	$C_{6,5}^{\text{diff}}$
0,1	5,54E-09	5,57E-09
30	5,57E-09	5,66E-09
60	5,66E-09	5,90E-09
90	5,79E-09	6,24E-09
120	5,95E-09	6,65E-09
150	6,13E-09	7,16E-09
180	6,35E-09	7,89E-09
210	6,63E-09	9,05E-09
240	7,02E-09	1,08E-08
270	7,56E-09	1,36E-08
300	8,34E-09	1,53E-08

In the following a different approach is used [9]. In this approach one does not require a multitude of electrostatic results, but a single electroquasistatic time-domain simulation. In many ways, it is similar to the procedure for the extraction of the material characteristics. In particular, where one was previously interested in the coefficients of $J(t) \cong \sigma(|E(t)|) E(t) + \frac{d}{dt} (\epsilon_r(|E(t)|) \epsilon_r U(t))$, one is now interested in:

$$I(t) \cong G(|U(t)|) U(t) + \frac{d}{dt} (C(|U(t)|) U(t)). \quad (8)$$

However, $U(t)$ and $I(t)$ are vectors, and G and C are conductance and capacitance matrices at each time t . The procedure can be described as follows:

- Electroquasistatic time-domain simulation with realistic and linearly independent excitation of the conductors. During the simulation the current entering/leaving a conductor, the electric potential and its time derivative are saved for a sufficient number of time steps.
- Choice of some parameters.
- Assembly and solution of an over-determined linear system $A x = b$.
- Translation of vector x to material characteristics partial capacitances $c_{ij}(|U_i - U_j|)$ and conductances $g_{ij}(|U_i - U_j|)$.
- Composition of the capacitance and conductance matrices from the partial capacitances and conductances. (if required; for a set of potentials)

The program FEMK, which is developed at our institute, was expanded to be able to calculate electroquasistatics problems with nonlinear permittivity as well as to accept different excitation signals (phase, frequency) for each conductor and write the data needed for post-processing. Then, the potential and current data are used in a MatLab™ code to estimate the nonlinear partial capacitances and conductances. The user may choose the polynomial degree of the capacitances or the (non-) symmetry of the matrices. Before application to objects with a plentitude of conductors (e.g., a stator slot), negligible coupling capacitances should be eliminated from consideration. Based on the following relation for the resistive current I_i^r for a particular conductor i

:

$$I_i^r \cong \sum_k g_{ii}^{(k)} (|\Phi_i|) \Phi_i^{k+1} + \sum_k \sum_{j \substack{ \\ (i \neq j)}} g_{ij}^{(k)} (|\Phi_i - \Phi_j|) \cdot (\Phi_i - \Phi_j)^{k+1} \quad (9)$$

and a similar expression for the displacement current, a linear system is built. Its solution provides the partial conductance and capacitance coefficients $g_{ij}^{(k)}$ and $c_{ij}^{(k)}$, where the indices i and j indicate conductors and k the polynomial degree.

9. Wave Propagation

The potentials in the different conductors of a cable (or stator slot) should be simulated by a multiconductor transmission line model as shown in Fig. 9. A way to obtain the coupling conductances G_{ij} and C_{ij} was described above, but R_i and L_i have to be obtained elsewhere, yet. An experimental MatLabTM code was written to simulate the wave propagation along a (fictitious) 2-line conductor including nonlinear and relaxation effects ([10],[11]). The underlying algorithm is symplectic (i.e., energy-conserving), if the conductor is composed exclusively of linear elements. But symplecticity is not necessarily conserved, when the elements are nonlinear or include relaxation processes.

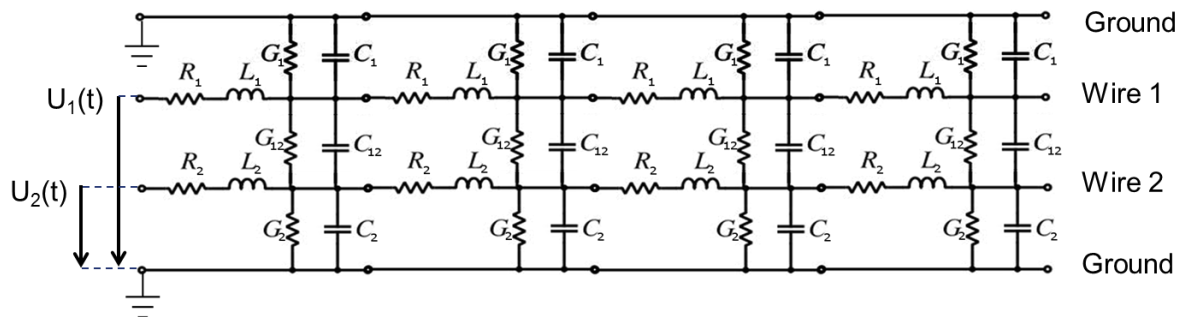


Figure 9 Section of a multiconductor transmission line with three wires (Wire 1, Wire 2 & Ground) excited by input voltages U_1 and U_2 . The conductances G and capacitances C may depend nonlinearly on the voltage difference between the nodes (nonlinearity) and on past voltage differences (relaxation).

Simulations with arbitrary parameters, nonlinear capacitance and excitation by a Gauss signal showed that the signal becomes increasingly steep during its propagation. Finally, the CFL criterion is violated and the results become erroneous. In the presence of (Debye) relaxation the appearance of this problem is delayed or eliminated. Thus, in this context, relaxation is less an additional problem than a remedy. Possibly, the conservation of energy could have been disregarded for the study of parasitics and nonlinear field control materials. Instead, if one added the influence of the iron sheet due to the induced currents using an analogous approach for magneto-quasistatics, one could obtain a good transmission line model for windings. In any case, the work on the propagation of signals along a multi-conductor transmission line had to remain uncompleted, when the project ended.

10. Conclusion

The main result of the work in this subproject is the development of methods and software which provide a continuous work-flow, which begins with the characterization of the relevant materials and ends with the simulation of transient signals, like parasitic effects in drives. The individual steps are the characterization of microvaristor materials/coatings, the simulation of geometries (e.g., windings) with nonlinear materials, the extraction of nonlinear conductances and capacitances and their insertion into a transmission line model to calculate the propagation of impulses along parallel conductors.

The investigations performed in this work on the properties of microvaristor materials confirmed that these do not only possess a nonlinear conductivity, but that their permittivity is, at least macroscopically, also nonlinear. Furthermore, it was shown that in order to properly characterize these materials relaxation effects need to be taken into account. The non-linear material characteristic obtained by our microvaristor models was inserted into a 2D planar/axisymmetric finite element program, which was developed in the course of this project. From the simulations, conductance and capacitance matrices were extracted. As the common approach is only valid for linear models, a new approach for the non-linear case was developed.

Comparing the realized work with the original schedule, one observes a number of differences. The characterization of microvaristor materials was not part of the original schedule, although it absorbed most of the time. At the time microvaristor insulation shieldings were to be simulated, a satisfactory characterization of the material was not available. Thus, a better description of the material properties was absolutely necessary. It was, furthermore, in many cases not possible to compare and/or validate simulations with experimental data. This was the case, e.g., for the microvaristor-filled cables which are neither commercially available, nor could they be manufactured at the TU Darmstadt. Finally, the construction of a detailed transmission-line model for the motor windings as well as the application of multi-scale time domain simulations including microvaristor shielding components could not be completed as scheduled. The main reason for this is that the electrical behavior and thus the characterization of microvaristor materials turned out to be much more complicated than originally planned. The better understanding of these materials remains an open issue which is difficult to be properly tackled without the assistance of material scientists. For this reason, DFG decided earlier this year to support the multidisciplinary project at the TU Darmstadt "Impuls-Energieaufnahmevermögen von MO-Varistoren für Überspannungsableiter in Hochspannungsnetzen" by J. Rödel, V. Hinrichsen and T. Weiland.

References

- [1] F. Denz, E. Gjonaj, and T. Weiland, „Simultaneous Determination of Nonlinear Material Properties“, KWT 2010 – Workshop on Advances in Electromagnetic Research, Waren a.d. Müritz, August 4th, 2010.
- [2] F. Denz, E. Gjonaj, and T. Weiland, „Nonlinear Characterization and Simulation of Zinc-Oxide Surge Arresters“, in: Scientific Computing in Electrical Engineering SCEE 2010, pp. 213-222, ISBN 978-3-642-22452, 2012.
- [3] S. Bitterlich, W. Durner, S. C. Iden, and P. Knabner, „Inverse Estimation of the Unsaturated Soil Hydraulic Properties from Column Outflow Experiments Using Free-Form Parameterizations“, *Vadose Zone J.*, Bd. 3, Nr. 3, S. 971-981, 2004.
- [4] S. Bitterlich und P. Knabner, „Formfree and cascadic identification of material laws in (un) saturated fluid flow from column experiments“, *Zeitschrift für Angewandte Mathematik und Mechanik*, Bd. 81, S. 13-16, 2001.
- [5] S. Bitterlich und P. Knabner, „Adaptive and Formfree Identification of Nonlinearities in Fluid Flow from Column Experiments“.
- [6] W. Durner, S. Bitterlich, und P. Knabner, „Bestimmung parameterfreier bodenhydrologischer Eigenschaften aus instationären Fließexperimenten durch inverse Simulation“, *Mitteilungen der Deutschen Bodenkundlichen Gesellschaft*, Bd. 96, Nr. 1, S. 65-66, 2001.
- [7] D. Meeker, “FEMM Reference Manual” [Online]. Available on 28.06.2012 at <http://www.femm.info/Archives/doc/manual42.pdf>.
- [8] F. Denz, E. Gjonaj, and T. Weiland, “Determination of Nonlinear Conductance and Capacitance Matrices”, KWT 2011 – Workshop on Advances in Electromagnetic Research, Riezlern, August 20th – 26th, 2011.
- [9] D. Weida, S. Böhmelt, und M. Clemens, „Design of ZnO microvaristor end corona protection for electrical machines“, in: *Electrical Insulation (ISEI)*, 2010, pp. 1–4.
- [10] A. Taflove, *Computational electrodynamics the finite-difference time-domain method*, 3rd ed.; Boston, London: Artech House, 2005.
- [11] K. Afrooz und A. Abdipour, „Efficient Method for Time-Domain Analysis of Lossy Nonuniform Multiconductor Transmission Line Driven by a Modulated Signal Using FDTD Technique“, *Electromagnetic Compatibility, IEEE Transactions on*, Bd. PP, Nr. 99, S. 1-13, 2011.